The Computational Modelling of Electromagnetic Acoustic Imaging

Ning Zhang

Wadham College

Department of Engineering Science

University of Oxford

A thesis submitted for the degree of Doctor of Philosophy

Trinity term 2015

Abstract

Computational Modelling of Electromagnetic Acoustic Imaging

Ning Zhang

Wadham College

Department of Engineering Science

University of Oxford

A thesis submitted for the degree of Doctor of Philosophy

Trinity Term 2016

The Electromagnetic Acoustic (EMA) technique is a novel multi-modal technique for medical imaging. It is sensitive, in principle, to contrast in mechanical properties and electrical properties and has potential in a number of applications such as breast tumour detection where there will be contrast between diseased and healthy tissue and high intensity focused ultrasound monitoring, where there will be contrast when tissue is ablated.

A complete computational model for the EMA imaging is developed. The model considers the linear or nonlinear propagation of ultrasound in soft tissue, the dynamic response of the viscoelastic soft tissue to acoustic radiation force (ARF) stimulation and scattering of electromagnetic waves with and without the Doppler effect.

The suitability of the EMA imaging for breast tumour detection is evaluated, modelling a tumour as a spherical inclusion in an infinite homogeneous background tissue with clinically relevant material properties. The results show that variations of the mechanical properties of underlying healthy breast tissue and tumour tissue in clinically feasible range should result in a change in the amplitude of the first Doppler component (FDC) of up to 50%, and varying the electrical contrast leads to a change in the ratio of the FDC and unshifted component (UC) of less than 1 dB. The relative difference between the first Doppler component and the unshifted component is greater than 68 dB and therefore the frequency demodulation may pose a significant challenge if EMA imaging is used for breast tumour detection.

The feasibility of using the EMA imaging for real-time monitoring of High Intensity Focused Ultrasound (HIFU) therapy is also investigated. Simulations conducted with realistic liver tissue properties show that the induced Doppler effect in the scattered EM wave is not well correlated with the growth of thermal lesion, therefore it is unlikely to be a good indicator of the lesion size. EMA imaging may not be appropriate for monitoring HIFU therapy.

Table of Contents

List of Figures I

List of Tables VIII

List of Symbols IX

List of Abbreviations XIV

Acknowledgement XV

Chapter 1 Literature review 1

1.1 Introduction 1

1.2 Overview of medical imaging technologies 4

1.2.1 X-ray Based Imaging 4

1.2.2 Magnetic resonance imaging 5

1.2.3 Ultrasound imaging 7

1.2.4 Microwave imaging 9

1.2.5 Acoustic radiation force based imaging 12

1.3 Electromagnetic acoustic (EMA) technique 14

1.3.1 Physics basis of EMA 14

1.3.2 Examples of interactions between EM and acoustic waves 15

1.3.3 Medical application of EMA imaging 16

1.4 Breast tumour screening 21

1.5 HIFU monitoring 23

1.6 Thesis organisation 25

Chapter 2 EM Scattering from oscillating spheres and vibrating cylinders 27

2.1 Introduction 27

2.2 EM Scattering from an electrically small dielectric sphere in harmonic oscillation 29

2.3 Sheet boundary condition 36

2.4 A FEM-SBC model in 2D 41

2.4.1 Introduction to the investigated problem 41

2.4.2 Method: TM case 43

2.4.3 Method: TE case: 46

2.4.4 Results and Discussion: 48

2.5 Summary 53

Chapter 3 An EMA model for medical imaging in 3D 54

3.1 Introduction 54

3.2 The linear acoustic model 56

3.3 A linear viscoelastic model 65

3.4 EM scattering from a stationary object 74

3.5 A FEM-SBC model in 3D space 80

3.6 Summary 85

Chapter 4 EMA imaging of breast tumours 86

4.1 Introduction 86

4.2 Safety of EMA 87

4.3 Modelling a breast tumour as a spherical inclusion 91

4.4 Impact of mechanical properties 97

4.5 Impact of electrical properties 108

4.6 Impact of inclusion size 111

4.7 Summary 114

Chapter 5 EMA monitoring of HIFU therapy 116

5.1 Introduction 116

5.2 A HIFU-EMA model 117

5.3 Simulating EMA during HIFU exposure 120

5.4 Sensitivity to mechanical properties 128

5.5 Impact of varying ultrasound intensity 134

5.6 Summary 139

Chapter 6 Conclusions and Future Work 141

6.1 Conclusions 141

6.2 Future work 146

Bibliography 149

List of Figures

Figure 1.1 Schematic of the EMA imaging system developed at the University of Oxford. A focused ultrasound transducer was used to produce a time varying ARF. Horn antennas operating at 434 MHz were used to transmit EM signals into the tissue and receive scattered signal. The system employed a phased-locked-loop and locked in amplifier to demodulate the scattered EM signal [39].*The grey circular arc is the boundary of the soft tissue.* 18

Figure 2.1 An oscillating electrically small sphere is oscillating in a sinusoidal manner along the y axis about the origin as described by Equation 2.4. A monochromatic plane EM wave described by Equation 2.1 travels in the +y direction and is incident of the sphere. The scattered EM wave is observed at an arbitrary location described by the spherical coordinate (r, θ, φ). 31

Figure 2.2 The spectrum of an EM wave scattered by an oscillating dielectric sphere. The sidebands are a result of the Doppler effect. The two sidebands at $\omega em \pm \omega 0$ *are first Doppler components. Other sidebands are very small according to the small argument approximation and are omitted from the discussion.* 34

Figure 2.3 The directivity of the FDC in the scattered EM signal as functions of (a) φ *is the x-y plane and (b)*θ *is the y-z plane.* 35

Figure 2.4 Illustration of the sheet boundary condition: The vibrating object can be replaced by a stationary object and a stationary object with a time-varying SBC. The EM signal scattered by the former is equivalent to the UC and the latter equivalent to the FDC. 37

Figure 2.5 The object boundary is discretized into a collection of small elementary patches 40

Figure 2.6 The TM (TE) incidence of an EM wave on a circular dielectric cylinder of radius a. The EM wave travels in +y direction. The observer is located at a location (r, φ*) in polar coordinates.* 42

Figure 2.7 The FEM-SBC model of a dielectric cylinder built in the FEM package. The model is composed of a circular cylinder (pink), a circular background space (grey) and a perfectly matched layer (blue). 45

Figure 2.8 The comparison between the FEM-SBC simulations (red) to analytical solutions (blue) of the amplitude of the FDC as a function of the bi-static angle for a vibrating dielectric cylinder that is vibrating at mode 1(a), mode 2(b), and mode 3(c) in TM case. 49

Figure 2.9 The change in the FDC and UC as a function of $\varepsilon 2$ *for the case of TM incidence depends on the mode number N.*...50

Figure 2.10 The comparison between the simulations (red) to analytical solutions (blue) of the amplitude of the FDC as a function of the bi-static angle for a vibrating dielectric cylinder that is vibrating at mode 1(a), mode 2(b), and mode 3(c) in TE case....51

Figure 2.11 The change in the FDC and the UC as a function of $\varepsilon 2$ *for the case of TE incidence depends on vibration mode number N.* 51

Figure 3.1 The simulation process of the proposed EMA model for medical imaging. The linear acoustic model considers the ultrasound propagation in soft tissue. The linear viscoelastic model considers the tissue dynamics under the ARF stimulation. The EM scattering from static object model and Doppler scattering model consider the regular and Doppler scattering from an oscillating object.................................54

Figure 3.2 The geometry of a concave spherical ultrasound transducer 58

Figure 3.3 Schematic of the measurement system for the ultrasound pressure profile. The measurement was realised by a computer controlled acquisition system. The step size of the measurement was 1mm in the axial direction and 0.1 mm in the lateral direction. 58

Figure 3.4 The comparison of the linear acoustic model predicted and experimentally measured pressure field (a) in the lateral direction at the focal length and (b) in the axial direction f_{us} *= 5 MHz*...........................60

Figure 3.5 The simulated spatial distribution of the normalized acoustic radiation force produced by the 5 MHz ultrasound transducers with $r0 = 94\ mm$ *and a = 12.7 mm.*...63

Figure 3.6 The acoustic pressure produced by a 5MHz transducer (a) is amplitude–modulated by a sinusoidal signal at $\omega arf/2$ *(b), resulting modulated time varying pressure (c) and ultrasound intensity (d) at an angular frequency* ωarf*. The resultant ARF is related to I(t) by equation 3.2.*......64

Figure 3.7 Illustration of the geometry of the linear viscoelatic model based on FEM: the axial symmetrical tissue with scatterer omitted from the illustration (left) and the spatial distribution of ARF (right). The colour bar show the normalised amplitude of ARF. 69

Figure 3.8 The dynamic response of the soft tissue to an ARF pulse: FEM simulated solution at 1cm (P1) and 2 cm(P2) away from the point of stimulation compared to Green's function based solution: (a) $\eta s = 0$ $Pa \cdot s$ *and (b)* $\eta s = 0.2$ $Pa \cdot s$*.* 72

Figure 3.9 The geometry of the EM scattering model by stationary object implemented in Comsol Multiphysics 74

Figure 3.10 The geometry of surface equivalent model. An imaginary closed surface is created just outside the scatterer......75

Figure 3.11 Comparison of the EM scattering model and the surface equivalence model. (a) the scattered E field in y-x plane in the EM scattering model for a static object and (b) the radiated E field form equivalent current in the surface equivalence model. The virtual surface is marked out by the red circle and the boundary of the scatterer is marked out by white circle. Colour bar unit V/m......77

Figure 3.12 The comparison of the directivity of the EM scattering model and surface equivalence model 89 mm away from the centre of the scatterer in the y-x plane.......79

Figure 3.13 Illustration of a 3D scatterer with vibrating boundary. An elementary area at location indicated by vector $\boldsymbol{r}$ *is highlighted with its associated normal oscillation (green arrow) and tangential E field (orange arrow)* 80

Figure 3.14 The FEM-SBC simulated FDC (red)received 150 mm away from the electrically small and oscillating sphere plotted as a function angle *compared to analytical solution (blue)in(a) y-x plane, (b) plane y-z plane.* 82

Figure 3.15 The FEM-SBC simulation compared (red) to analytical solution (blue) for oscillating sphere as a function of radius, for $\varepsilon_{ic} = 19$, $\sigma_{ic} = 0$ *S/m and* $\varepsilon_{bg} = 18$, $\sigma_{bg} = 0$ *S/m* 84

Figure 3.16 The FEM-SBC simulation (red) compared to analytical solution (blue) for oscillating sphere as a function of ε_{ic}, *for* $\varepsilon_{ic} = 18.5\text{-}20$, $\sigma_{ic} = 0$ *S/m and* $\varepsilon_{bg} = 18$, $\sigma_{bg} = 0$ *S/m* 84

Figure 4.1 (a) The dynamic response of homogeneous linear viscoelastic tissue (E = 3 kPa, $\eta s = 1.2\ Pa \cdot s$ *and* $\rho = 1000\ kg/m^3$*) to a step force (blue) and a harmonic force (black) and the sum (red) (b) The dynamic response of linear viscoelastic soft tissue to the sum of two forces is equivalent to the sum of the dynamic responses of the same tissue to each of the two forces as would be expected for linear simulation.* 93

Figure 4.2 The dynamic response of the spherical inclusion to amplitude modulated ARF. a: The snapshot of the spherical inclusion at t = 0 ms (A: before ARF was applied), t = 9.4ms (B: ARF is at local maximum), and t = 12.6 ms (C: ARF is at local minimum; b: the time-varying displacement at different locations at the spherical boundary shown in A (red spot: $\phi = -90°$, *blue spot:* $\phi = 0°$, *and black spot:* $\phi = 90°$*). Note that to illustrate the deformation of the spherical boundary, the actual displacement in (a) was magnified by 100 times* 95

Figure 4.3 The amplitude (a) and phase (b) of the oscillatory displacement of the spherical boundary of the inclusion under the excitation of ARF as a function of ϕ 96

Figure 4.4 The simulated FDC (a: in the y-x plane and b in the y-z plane) received a focal distance (89 mm) away from the centre of spherical inclusion and the simulated UC(c: in the y-x plane and d in the y-z plane) as functions of the bi-static angle φ *between the transmitter and receiver*..96

Figure 4.5 The amplitude (a,c) and phase (b,d) of the oscillation at the spherical boundary of inclusions with $r_{ic} = 0.5$ *mm (a,b), and 6 mm (c,d) as functions of* ϕ. E_{ic} *is 9 kPa (blue curve) 24 kPa(green curve) and 42 kPa* *(red curve). The background medium is $E_{bg} = 3$ kPa. Horizontal axis unit: degree* 100

Figure 4.6 The amplitude (a,c) and phase (e,h) of the oscillation at the spherical boundary of inclusions with $r_{ic} = 0.5$ mm (a,b), and 6 mm (c,d) as functions of ϕ. η_{s_ic} is 3.2 $Pa \cdot s$ (blue curve) 7.2 $Pa \cdot s$ (green curve) and 10.2 $Pa \cdot s$ (red curve). The background medium viscosity is 1.2 $Pa \cdot s$. Horizontal axis unit: degree 101

Figure 4.7 The amplitude (a,c) and phase (e,h) of the oscillation at the spherical boundary of inclusions with $r_{ic} = 0.5$ mm (a,b), and 6 mm (c,d) as functions of ϕ. ρ_{ic} is 800 kg/m^3(blue curve) 1000 kg/m^3 (green curve) and 1200 kg/m^3 (red curve). The background medium $\rho_{bg} = 1000$ kg/m^3. Horizontal axis unit: degree 102

Figure 4.8 The impact of Young's modulus: blue star (Blue star: $E_{bg} = 3$ kPa, Green triangle: $E_{bg} = 6$ kPa and red circle: $E_{bg} = 9$ kPa) on the FDC for spherical inclusions with (a) r_{ic}= 0.5 mm, (b) r_{ic}= 1.5 mm,(c) r_{ic}= 4.5 mm and (d) r_{ic}= 6 mm 104

Figure 4.9 The impact of shear viscosity: (Blue star: $\eta_{s\_bg} = 1.2$ $Pa \cdot s$, Green triangle: $\eta_{s\_bg} = 2.2$ $Pa \cdot s$ and red circle: $\eta_{s\_bg} = 3.2$ $Pa \cdot s$) on the FDC for spherical inclusions with (a) r_{ic}= 0.5 mm, (b) r_{ic}= 1.5 mm,(c) r_{ic}= 4.5 mm and (d) r_{ic}= 6 mm. 105

Figure 4.10 the impact of density: (Blue star: ρ_{bg} =800 kg/m^3, green triangle: ρ_{bg} =1000 kg/m^{3}and red circle: ρ_{bg} =1200 kg/m^3) on the FDC for spherical inclusions with (a) r_{ic}= 0.5 mm, (b) r_{ic}= 1.5 mm,(c) r_{ic}= 4.5 mm and (d) r_{ic}= 6 mm 107

Figure 4.11 The impact of the relative permittivity of the inclusion material on the FDC (Blue triangle) and the UC (red circle) and FDC/UC in dB (green diamond). The arrows indicate the appropriate vertical axes. 110

Figure 4.12 The impact of the electrical conductivity of the inclusion material on the FDC (blue triangle) and UC (red circle) and FDC / UC in dB (green diamond). The arrows indicate the appropriate vertical axes. 110

Figure 4.13 The FEM-SBC simulated impact on the FDC of the varying r_{ic} from 1 mm to 10 mm when the spherical inclusion oscillates uniformly and harmonically (blue triangle) or oscillates under ARF excitation (red *circle) together with the analytical solution given in Chapter 2 (green dot).* 113

Figure 4.14 FEM-SBC simulated ratio of the FDC and UC in dB for uniformly and harmonically oscillating sphere (blue triangle) and ARF excited spherical inclusion (red circle) 113

Figure 5.1 Block diagram of the HIFU-EMA model to illustrate the simulation process: inside the red dash line box is the HIFU model consisting of a non-linear acoustic model, a thermal model and a thermal dose model. Outside the red box is the EMA model as introduced in Chapter 3 with an additional surface equivalence model. 117

Figure 5.2 Schematic of the employed HIFU transducer. The transducer has a radius of aperture radius a = 3.2 cm, a radius of curvature d = 6.26 cm and a centre frequency of 1.1 MHz. 121

Figure 5.3 (a) The normalized spatial distribution of the ARF (the same as the normalized heating rate map) and (b) the resultant temperature elevation at the ultrasound focal point with I_{spta} *= 750 W/cm*^{2}........ 125

Figure 5.4 The growth of the thermal lesion as a function of HIFU exposure time shown as three snapshots at t = 1.87 s, 2.50 s and 3.12 s. The boundary of the lesion is determined using the thermal dose model 125

Figure 5.5 (a) The displacement of tissue at the ultrasound focal point before the lesion is formed (blue curve) and at the end of the thermal ablation (red curve); (b) the displacement field at the end of the ablation plotted as vector field along the lesion boundary 126

Figure 5.6 (a) The normalized backscattered FDC and UC received at the face of the ultrasound source as a function of HIFU exposure time and (b) FDC/UC as a function of HIFU exposure time 127

Figure 5.7 The sensitivity of the FDC to the attenuation coefficient (α_{le}*) of thermal lesion tissue. (a) shows the oscillatory displacement at the ultrasound focal point before the lesion is formed (b) compares the displacement at the ultrasound focal point towards the end of the thermal therapy; (c) compares the resultant FDC with different attenuation coefficient assigned to the lesion tissue in the linear-viscoelastic model ;(d) shows* *the resultant change in the FDC/UC; the subscript le denotes the property for the lesion tissue.* 131

Figure 5.8 The changes in the FDC when the stiffness ratio between the lesion tissue and untreated tissue is varied from 4 to 12. 132

Figure 5.9 The changes in the FDC when the shear viscosity ratio between the lesion tissue and untreated tissue is varied from 1 to 30 133

Figure 5.10 The impact of increasing ultrasound intensities on the FDC and simulated lesion volume by the HIFU model. The scattered EM signal is recorded 6.26 cm away from the ultrasound focal point at the backward scattering position 136

Figure 5.11 Simulated volume of thermal lesions formed at different ultrasound intensities (I_{spta}= 1445 W/cm^2 and 1135 W/cm) compared to experimental measurements described in [127]. 138

List of Tables

Table 2.1 Summary of parameters employed in the FEM-SBC simulations for EN scattering by dielectric cylinders. f_{em} is the EM wave frequency, f_0 the ARF modulation frequency, N the resonance mode, a the cylinder radius, ε the relative permittivity and μ the relative permeability. 48

Table 3.1 Summary of the electrical properties of the scatterer and background medium at 434 MHz 77

Table 3.2 Summary of the electrical properties of the scatterer and background material at 434 MHz. ε is the relative permittivity, μ the relative permeability and σ the electrical conductivity. 81

Table 4.1 The material properties assigned to the linear-viscoelastic model (E is the Young's modulus, η_s the shear viscosity, ρ the material density, α the ultrasound attenuation coefficient, ε the relative electrical permittivity, σ the electrical conductivity, and μ the relative magnetic permeability [26] [102] [103] [104] [105] [106]. 92

Table 5.1 The non-linear acoustic parameters of bovine liver tissue used in the non-linear acoustic simulation, data summarized from [113] at $37°C$..121

Table 5.2 The thermal parameters of bovine liver tissue used in the thermal map model, data summarized from [52]. As the perfusion rate w_b was taken to be 0 kg/m^3/s (no heat loss due to blood flow), C_b and T_a are not required. 122

Table 5.3 The mechanical parameters [117] and electrical properties [60] of untreated and coagulated bovine liver tissue used in the linear viscoelastic model. For material densities of both tissues, refer to Table 5.1. E is the Young's modulus, η_s the shear viscosity, ρ_0 the material density, ν the Poisson's ratio, ε the relative electrical permittivity, σ the electrical conductivity, and μ the relative magnetic permeability..122

List of Symbols

f_{em}, ω_{em}	The frequency and angular frequency of electromagnetic wave
f_{us}, ω_{us}	The frequency and angular frequency of ultrasound
f_{arf}, ω_{arf}	The frequency and angular frequency of the acoustic radiation force
E_i	*Incident electric field*
E_s	*Scattered electric field*
k_{em}	*The wavenumber of electromagnetic wave*
ε_0	*The electric permittivity of free space*
μ_0	*The magnetic permeability of free space*
ε_1 ,ε_2	*The relative permittivity of the material outside (subscript 1) and inside (subscript 2) the scattering object*
μ_1, μ_2	*The relative permeability of the material outside (subscript 1) and inside (subscript 2) the scattering object*
Z_1,Z_2	*The intrinsic impedance of the material outside (subscript 1) and inside (subscript 2) the scattering object*
E_1,E_2	*The electric field eternal (subscript 1) and internal (subscript 2) to the object boundary*
H_1,H_2	*The magnetic field eternal (subscript 1) and internal (subscript 2) to the object boundary*
k_{em1},k_{em1}	*The wavenumber of the electromagnetic wave propagating outside (subscript 1) and inside (subscript 2) the scattering object*
Z_1^s,Z_2^s	*The sheet impedance related to the sheet boundary condition outside (subscript 1) and inside (subscript 2) the scattering object*
Y_1^s,Y_2^s	*The sheet admittance related to the sheet boundary condition outside (subscript 1) and inside (subscript 2) the scattering object*

Ξ	Local displacement normal to the boundary of the scattering object
Γ_{mn}, θ_{mn}	The amplitude and phase of the nth normal Fourier modes of the oscillatory displacement of the mth elementary patch
$\xi(\varphi', t)$	The time varying oscillatory displacement of boundary of a circular cylinder in polar coordinates
$\Xi(\varphi', \omega)$	*The Fourier transform of* $\xi(\varphi', t)$
E_z^i,E_z^s	*The incident (superscript i) and scattered (superscript s) electric field polarized in z direction in transverse magnetic mode*
J_n	*Bessel function of the first kind*
$H_n^{(2)}$	*Hankel function of the second kind*
J_z	*The density of the equivalent sheet current in transverse magnetic mode*
H_z^i	*The incident magnetic field polarized in z direction in transverse electric mode*
E_{tan}^2	*The scattered electric field in transverse electric mode*
J_s	*The density of the equivalent sheet current in transverse electric mode*
p	*The radiated ultrasound pressure field by a ultrasound transducer*
p_0	*The effective source pressure on the transducer surface*
ρ_0	*The material mass density*
u_0	*The surface velocity on the transducer surface*
c_0	*The speed of sound*
k_{us}	*The wavenumber of ultrasound wave*
r_0	*The radius of curvature of an focused ultrasound transducer*
a	*The radius of aperture of an ultrasound transducer*

I_{sppa}	*The spatial peak pulse averaged intensity*
I_{spta}	*The spatial peak time averaged intensity*
I_{sptp}	*The spatial peak temporal peak intensity*
$\sigma_{ij,j}$	The directional derivative of the stress tensor
b_i	The externally applied steady state acceleration
f_i	The externally applied radiation force
δ_{ij}	*Kronecker delta*
σ_{ij}	*Stress tensor*
$u_{i,j}$	*The displacement field*
$\bar{\lambda}, \bar{\mu}$	*The complex first and second* Lamé *constants*
ψ	*Longitudinal wave*
$\vec{W}$	*Shear wave*
c_l	*The longitudinal wave speed*
α_l	*The attenuation coefficient of longitudinal wave*
k_l	*The wavenumber of the longitudinal wave*
α_s	*The attenuation coefficient of shear wave*
c_s	*The shear wave speed*
k_s	*The wavenumber of the shear wave*
g_{ij}	*The transient response of soft tissue to spatial and temporal impulse excitation*
$v_l, v_s,$	*The kinematic bulk (subscript l) and shear (subscript s) viscosity*
η_l, η_s	*The bulk (subscript l) and shear (subscript s) viscosity*

γ_i	*The directional cosine*
J_s^{se}	*The surface equivalence current*
$\xi_{\vec{r}}(t)$	*The local displacement normal to the boundary of a 3D object*
$\Gamma_{\vec{r}}$	*The amplitude of the displacement normal to the boundary of a 3D object*
$\Xi(\omega)$	*The Fourier transform of* $\xi_{\vec{r}}(t)$
$J_{\vec{r}}$	*The equivalent current of sheet boundary condition in 3D*
Σ	*Electrical conductivity*
r_{ic}	*The radius of the spherical inclusion*
$\varepsilon_{\mathrm{ic}},\varepsilon_{bg}$	*The relative permittivity of the inclusion (subscript ic) and background (subscript bg)*
$\mu_{\mathrm{ic}},\mu_{\mathrm{bg}}$	*The relative permeability of the inclusion (subscript ic) and background (subscript bg)*
$\sigma_{\mathrm{ic}},\sigma_{\mathrm{bg}}$	*The electrical conductivity of the inclusion (subscript ic) and background (subscript bg)*
p_r	*The peak rarefaction pressure*
W_p	*The derated acoustic power*
W_{deg}	*The energy required to raise the tissue equilibrium temperature by 1degree*
γ_{v}	*The specific heat at constant volume*
E	*The Young's modulus*
E_{ic},E_{bg}	*The Young's modulus of the inclusion (subscript ic) and the background (subscript bg)*
$\eta_{\mathrm{s\_ic}},\eta_{\mathrm{s\_bg}}$	*The shear viscosity of the inclusion (subscript ic) and the background (subscript bg)*
ρ_{ic},ρ_{bg}	*The material density of the inclusion (subscript ic) and the background (subscript bg)*

β	*The non-linear coefficient in non-linear acoustics*
α_0	*The attenuation coefficient at 1 MHz*
C_t	*Heat capacity*
T	*Temperature*
w_b	*The blood perfusion rate*
C_b	*The heat capacity of blood*
T_a	*The arterial blood temperature*
ς	*The power law exponent of frequency dependent ultrasound attenuation*
Q	*Heating rate*
ν	*Poisson's ratio*
α_{le}	*The ultrasound attenuation of lesion tissue*
E_{lesion}	*The Young's modulus of lesion tissue*

List of Abbreviations

EM	Electromagnetic
EMA	Electromagnetic acoustic
ARF	Acoustic radiation force
HIFU	High intensity focused ultrasound
SBC	Sheet boundary condition
MRI	Magnetic resonance imaging
CT	Computed tomography
FEM	Finite element method
FDC	First Doppler component
UC	Unshifted component
PML	Perfectly matched layer
SAR	Specific absorption ratio

Acknowledgement

This thesis would not have been possible without the help of many intelligent and supportive people I met in Oxford and in my life.

Firstly, I would like to express my greatest gratitude to Professor Robin Cleveland and Professor David Edwards, who have provided invaluable advice and guidance throughout my doctoral research. It has been a very pleasant and rewarding experience working with them.

I would like to thank Dr Eleanor Edwards for the valuable discussion of the EMA imaging and EM coil design, Dr Edward Jackson, Dr Jamie Collins, Dr Sunali Bhatnagar and other colleagues in the BUBBL group for their help in characterising the acoustic transducers.

I would also like to thank Mr Graham Faulkner for his extensive technical support during my study, and my other colleagues in the communications group for providing their academic insights into electromagnetics.

Lastly, I would like to express my love and gratitude to my wife Siting, my brother Shuo and my parents to whom I am forever indebted to. Their constant moral support and love throughout my DPhil study has helped me through all the difficult times.

Chapter 1 Literature review

1.1 Introduction

Cancer is the name given to a group of over 100 diseases that are related to the changes or mutations in genes. Normal cells usually have a well-defined proliferation-differentiation-death lifecycle whilst abnormal cells, with altered DNA (deoxyribonucleic acid), may grow and divide at an unregulated and quickened pace without stopping [1] and may form cancer. In some case the cancer cells may form solid tumours (e.g. liver cancer) whilst other cancers, for example cancer in blood, usually do not form solid tumours [2]. Cancer is a leading cause of disease and death across the globe [3]. It was estimated that about 12.1 million cancer cases and 8.2 million deaths due to cancer occurred in 2012 worldwide with a projection of 23.6 million cancer cases annually by 2030 [3]. Detecting cancer at its earliest stages significantly improves prognosis [4] as does being able to effectively monitor cancer therapy [5].

Modern medical imaging techniques exploit the changes in tissue properties associated with tumours (Table 4.1) to gather information for cancer diagnosis or to detect tissue denaturation (Table 5.1 and Table 5.3) during cancer therapy (e.g., a thermal ablation) for treatment monitoring. The imaging technique investigated in this thesis is referred to as electromagnetic acoustic (EMA) imaging. It is a novel multi-modal imaging technique that exploits the contrast in electrical and mechanical properties simultaneously via the interaction between acoustic waves and electromagnetic waves in soft tissue.

The remainder of this chapter is organised as follows:

Section 1.2 briefly reviews a number of clinically well-established medical imaging modalities including X-ray imaging, magnetic resonance imaging and ultrasound imaging, as well as several emerging imaging modalities including microwave imaging and acoustic radiation force based imaging. The underlying physics, advantages and limitations of the imaging modalities are discussed.

Section 1.3 presents a historical account of the interaction between electromagnetic waves and acoustic waves, and an introduction of its applications in atmospheric temperature profiling, hydrophone calibration, landmine detection and medical imaging. For its application in medical imaging, prior theoretical and experimental investigation are introduced and discussed. This motivates the need to develop a complete theoretical framework for the EMA imaging.

Section 1.4 discusses the advantages and limitations of current methods for breast cancer screening, and provides motivation for the EMA imaging to be developed as a breast cancer diagnosing method.

Section 1.5 briefly introduces the physics basis of an emerging therapeutic method high intensity focused ultrasound (HIFU) for treating solid tumours. The real-time monitoring of HIFU is one of the major barriers for the wide clinical application of HIFU. Several techniques of the real time monitoring HIFU are introduced and discussed, followed by the motivation for the EMA as a viable HIFU monitoring technique.

1.2 Overview of medical imaging technologies

1.2.1 X-ray Based Imaging

X-rays undergo different degrees of attenuation when passing through tissues of different types. For example, bone, absorbs X-rays more strongly than soft tissue (tissues that connect, support, or surround other structures of the body, not being bone). Based on this phenomenon, X-ray based medical imaging techniques have been developed and are widely used in analysing acute injuries as well as diagnosing suspected chronic diseases. Commonly used imaging modalities based on X-ray include planar radiography and computed tomography (CT) [6].

In planar radiography, a collimated beam of X-rays is transmitted through the object to be imaged. A portion of the X-rays is attenuated by the object depending on the local attenuation which in turn is related to the material density. The remaining X-rays passing through the object are detected by an array of X-ray detectors. The recovered 2D image from the detected X-rays is a projection of X-ray absorption of all structures along the path of the transmitted X-ray beam – in effect a shadow.

In X-ray CT, the X-ray source and a bank of detectors are rotated around the patient in synchrony. The 1D projection of the X-ray beam through the cross section of the patient creates a shadow image [6]. Shadow images are captured at different angles which allow the cross section of the patient to be reconstructed via tomographic reconstruction algorithms.

There are certain drawbacks associated with the use of X-ray imaging. Exposure to ionizing radiation can potentially cause damage to DNA, which increases the life-time risk of cancer. The risk of developing cancer depends on the radiation dose, patient’s age and gender, and the exposed body region. In addition, increasingly the number of situations of anatomical and physiological imaging using X-ray CT require contrast enhancement by intravenously injecting contrast agents into the region of interest (effectively substances which increase the absorption of X-rays) and improving the visibility of features. Moreover, the contrast in the photoelectric absorption characteristic between different soft tissues types other than bone and lung tissue is often not significant. As a result X-ray imaging does not perform well in differentiating between soft tissues types.

1.2.2 Magnetic resonance imaging

Magnetic Resonance Imaging (MRI) originated from the discovery of nuclear magnetic resonance (NMR) in 1946 [7] [8]. At the atomic level, a hydrogen nucleus or a proton is a charged particle that spins around an internal axis of rotation with a given value of angular momentum and magnetic moment. Without an external magnetic field, the direction of the spinning axis is randomly distributed and the net magnetisation is zero. When a strong external static magnetic field is applied, the direction of the magnetic moment tends to preferentially align in parallel with the applied magnetic field, leading to a small but detectable magnetisation. The protons whose magnetic moments are parallel with the external field are of lower energy states compared to those that are not. Resonance is induced by applying energy packets in the form of radio frequency (RF) pulses, the energy of which match the energy gaps between different energy states of the spinning protons. This will cause the transition of the spinning protons at a lower energy state to a higher energy state, i.e., the axis of the spin is tilted out of alignment with the magnetic field, by absorbing the energy packets. The energised spinning protons return to the lower equilibrium energy state, and give up the energy absorbed during the resonance process in the form of RF emission, a process referred to as relaxation. The time constants that govern the relaxation process in the direction (T1) and transverse to the direction (T2) of the external magnetic field form the basis of MRI.

Compared to X-ray based imaging, MRI does not require ionizing radiation and is excellent in differentiating soft tissues. However, MRI also has drawbacks. First, the acquisition time of an MRI image is long compared to other major imaging techniques. Patients are often required to lie still for 30-40 minutes in a typical MRI scan due to the need to sample the MRI signal repeatedly to acquire sufficient data to build a complete image [9]. Second, the strong magnetic field involved in MRI precludes patients with metallic implants from previous orthopedic surgeries. Lastly, MRI systems are very expensive to install and maintain [6].

1.2.3 Ultrasound imaging

In ultrasound imaging, acoustic waves with frequencies typically between 1 and 15 MHz, are used to image soft tissue structures. Acoustic impedance is the ratio of the acoustic pressure and the volume flow. It is the product of the sound speed the mass density of the medium it propagates in and allows the calculation of the transmission and reflection of sound waves at boundaries of different medium [10]. Conventional ultrasound imaging is based on a pulse-echo approach, where a short (a few cycles) ultrasound pulse is produced by an ultrasound transducer and propagates through tissue. When the pulse encounters boundaries or small structures with different acoustic impedance, a fraction of the acoustic energy (an echo) is reflected or scattered whilst the remaining ultrasound is transmitted through the object. The echo propagates backwards and is detected by the ultrasound transducer. The distance from the ultrasound transducer to the reflecting tissue boundary is calculated from the arrival time of the echo and by assuming a known sound speed for soft tissue, typically 1540 *m/s*.

In A-mode scanning the amplitude of the backscattered ultrasound versus time along a single line of sight is generated and the major application of this technique is ophthalmic corneal pachymetry to measure the corneal thickness. The most commonly used imaging mode is brightness-mode (B-mode) scanning. In this mode, the acoustic beam is steered in a lateral direction and multiple A-lines (typically 100-200) are acquired to create a 2D image of a cross-section of the anatomical structure.

Ultrasound can also measure blood flow by exploiting the Doppler effect. The ultrasound signals are scattered by red blood cells and blood flow towards/away from the ultrasound transducer with a phase shift from which the Doppler frequency is obtained. The region of vessels can be identified from B-mode images. The calculated blood velocity in the region of interest may be coded in colour (red/yellow represents blood flow towards the probe whilst green/blue away from the probe) and overlaid on top of a B-mode image. Colour Doppler ultrasound is very useful in detecting unusual blood flow patterns and providing diagnosis reference for a number of pathological conditions.

The advantage of ultrasound imaging is that it doesn’t involve ionizing radiation and therefore the safety concerns are minimal. The equipment is portable, is relatively low-cost and is capable of producing images in real-time. Disadvantages of ultrasound imaging include its inability to image regions behind bones and air. It is also operator dependent and requires the sonographer to be highly skilled in order to acquire good quality images and make an accurate diagnosis.

1.2.4 Microwave imaging

Microwave imaging interrogates an object by examining the transmission and scatterering of electromagnetic pulses in the microwave regime (300 *MHz*~300 *GHz*) [11]. The potential clinical applications of microwave imaging includes: lung cancer detection, brain imaging, cardiac imaging and breast cancer detection [12]. Microwave imaging for breast tumour detection has attracted growing attention in the past few decades because breast tissue is easy to access and is largely composed of fatty tissue which is translucent to microwave signals. Microwave techniques can be classified as passive methods, hybrid methods and active methods. In the following paragraphs, a brief introduction to each of the three classes is provided [11].

Passive methods: Some pathological conditions are accompanied with disease related temperature abnormalities. For example, tumour tissue is of an increased temperature compared to surrounding healthy breast tissue due to increased vascularization. Passive methods, e.g., microwave radiometry, refer to techniques that measures the naturally emitted electromagnetic radiation from underlying object at microwave frequencies to detect such temperature abnormalities [13]. One key challenge in radiometry is the linking of temperature measured at the surface of the tissue to changes in the physical temperature due to the presence of a tumour. Numerical models have been developed to determine a weighting function that maps changes in physical temperature to surface temperatures measured by radiometry. With the weighting function, the physical temperature can be solved from the radiometry measurement using an inverse approach [11].

Hybrid microwave-acoustic method: Microwave induced thermal acoustic tomography is an innovative technique being developed for breast tumour detection [11]. When irradiated with microwave pulses, tumour tissue and healthy breast tissue absorb microwave energy differently due to the contrast in the absorption coefficient. The absorbed microwave energy heats up tissue and induces thermal expansion, which in turn creates an acoustic wave at the position of the tumour. The resulting acoustic wave is detected by an ultrasound transducer or array of ultrasound transducers. A map of absorption can be recovered from the detected acoustic signal by taking the advantage of advanced image reconstruction algorithms [11].

Active microwave methods: Active microwave imaging falls into two categories: a radar based approach and microwave tomography.

Radar based approaches aim to directly locate tumours by detecting the strong EM scatterers in the breast environment. An ultra-wide band microwave signal is employed to illuminate the tissue to improve the resolution. The backscattered signal is received by an antenna array whose focal point can be electronically steered. An image is obtained by scanning the focal point of the antenna array through a preselected volume. When the focal point coincides with the strongly scattering object (e.g., tumour), signals received by elements in the antenna array add constructively, which yields a significant response in the image [11] [14]. However, a problem associated with this approach is that it is very difficult to achieve accurate focusing in inhomogeneous medium of uncertain properties.

Tomographic approaches aim to create maps of electrical property distributions in the imaged object. Following a similar strategy as in X-ray CT, it involves illuminating the object with microwave and the scattered or transmitted microwave signals are collected by an array of antennas around the object. Reconstruction algorithms are employed to recover the microwave image by matching the measured microwave scattered by the object to the simulated results computed with a numerical model [15]. Such algorithms are under active research [16] [17].

Previous theoretical and experimental investigations have suggested that microwave imaging has the advantages of being low-cost compared to MRI imaging, non-ionizing compared to X-ray imaging and being able to differentiate soft tissues more effectively compared to ultrasound imaging. Therefore it is recognised as promising complementary technology to clinically established imaging modalities [18]. However, despite the positive results reported by various research groups, microwave imaging has not seen widespread use in clinics outside research labs, with only a few systems reached the stage of clinical test (the ONCOSCAN system [19] and the Dartmouth system [20]). Challenges in designing microwave antennas and developing efficient image reconstruction algorithms need to be overcome before the wide clinical application of microwave imaging.

1.2.5 Acoustic radiation force based imaging

Elastography is classification of elasticity measurement that involves generating a stress in the tissue and measuring the tissue response [21]. Acoustic radiation force (ARF) (see Section 3.2 for details) can be used to create the stress in tissue. Compared to static elastography, where the tissue compression is done by the sonographer manually compressing the transducer onto the skin of the patient, this method is expected to be less operator-dependent. A number of ARF based imaging modalities are under investigation: acoustic radiation force impulse (ARFI) imaging [22], harmonic motion imaging (HMI) [23] and shear wave elasticity imaging (SWEI) [24].

ARFI uses the diagnostic ultrasound scanner to create localized impulsive ARF within the soft tissue, which causes μm scale tissue displacements. A Correlation-based ultrasonic tracking algorithm is used to monitor the dynamic response of the tissue within the region of excitation (ROE). Parameters such as time to peak (TTP) displacements, time to recover (RT) from the peak displacements are used to characterize the dynamic response of the soft tissue. Stiffer tissues, e.g., thermal lesions and tumours tend to exhibit a distinctive characteristic response to impulse ARF compared to surrounding healthy soft tissues, and therefore can be differentiated. HMI is similar except that it applies a harmonic ARF to the tissue which causes the tissue within the ROE to oscillate at a specific frequency. With a separate ultrasound transducer, the harmonic signals are detected and the oscillatory motion is estimated at different snapshots of the motion using cross-correlation of RF signals, which reflects the viscoelasticity of the local tissue [23]. In SWEI and supersonic imaging (SSI) a short-duration ARF is used to generate a shear wave. As the shear wave passes through the tissue of interest, its propagation speed and attenuation can be measured using an ultrafast (~1*kHz*) ultrasound imaging sequence [24] [25] [26]. From measurements of the shear wave (see Section 3.3 for details of shear and longitudinal wave) speed and attenuation the viscoelastic properties of the tissue can be mapped with resolution of a few millimetres.

1.3 Electromagnetic acoustic (EMA) technique

1.3.1 Physics basis of EMA

There are a number of mechanisms by which acoustic and electromagnetic waves can interact.

In 1921 L. Brillouin was the first to predict the diffraction of light by ultrasonic waves of short wavelength travelling in a liquid medium. As the ultrasound wave propagates through a medium it compresses and rarefies the medium, which causes fluctuations in its dielectric constant, which in turn will affect the propagation of electromagnetic wave in the medium. The diffraction of light by ultrasound wave was observed approximately 10 years later by many researchers [27] [28]. Brillouin's theory was extended using the classical theory of scattering by G. Benedek and T. Greytak [28]. They derived an expression for the spectrum intensity of the light scattered by an ultrasonic wave propagating in a liquid medium which was then experimentally verified in the same work.

In situations where the medium is electrically inhomogeneous and ultrasound is applied to stimulate the medium to cause vibration, for example in the case of detecting buried electrical objects in a surrounding medium, the Doppler effect may be induced in the scattered EM signal by two mechanisms: 1) the vibration of the electrical boundary of the objects and 2) the fluctuation of the dielectric constant caused by the compression and dilation of the object material. This phenomenon is referred to as electromagnetic acoustic (EMA) interaction in this work. The first mechanism has much greater effect (>40 dB) than the second [29] and therefore the following investigation considers the first mechanism only.

1.3.2 Examples of interactions between EM and acoustic waves

The Radio Acoustic Sounding System (RASS) was developed for remotely measuring the temperature profile, wind profile, air quality as well as other atmospheric parameters using the direct interaction between sound waves and EM waves. The basic principle of RASS is the tracking of sound waves by EM radar. A sound pulse sent by the RASS compresses and rarefies air and alters the local dielectric constant. The disturbance in dielectric constant causes partial reflections of the EM energy, and therefore allows the travelling sound pulse to be tracked by a Doppler EM radar system. With the aid of more advanced techniques, such as the use of multiple beam directions, the reflected EM signal allows a series of atmospheric parameters to be determined [30] [31] [32].

The calibration of hydrophones is another application of the interaction of sound and light. It involves suspending an acoustically transparent but optically reflective pellicle (a thin plastic layer) in liquid media. A laser beam is transmitted towards the pellicle and gets reflected. As the motion of the thin pellicle follows the motion of the water particles, which modulates the reflected laser light, the velocity of the acoustic particles and the acoustical pressure can be estimated from the Doppler shift of the laser light [33] [34].

Detecting buried objects, especially non-metallic landmines buried in soil using the EMA imaging is under active research. It has been proposed that if one stimulates soil surface under which there is a buried landmine acoustically with unfocused acoustic source there will be a differential displacement. The Doppler shift of the scattered EM wave, and hence the presence of land mine, can be detected by ground-penetrating radar (GPR). Experiments based on this approach for buried landmine detection has been described [35] [36]. Experiments were carried out with simulated landmines of various models buried in damp sand and the capability of distinguishing several types of landmine from some naturally occurring clutter was demonstrated [37].

1.3.3 Medical application of EMA imaging

The feasibility of applying the EMA imaging in medical imaging was first investigated experimentally at the University of Oxford [38] [39]. The initial experimental system, shown in Figure 1.1, employed a focused megahertz ultrasound source, amplitude modulated, to create an oscillating radiation force for tissue excitation. The oscillatory motion of the tissue induced a shear wave that propagated laterally out of the region of excitation. Simultaneously the soft tissue was illuminated with an EM signal (434 *MHz*) from a horn antenna. The contrast in electrical permittivity and conductivity between the excited tissue and background tissue caused the EM signal to be scattered and undergo a Doppler shift due to the oscillatory motion experienced by the tissue boundary. The scattered EM signal was detected by a receiving horn antenna, demodulated with a phase-lock-loop circuit and then processed with a lock-in amplifier to extract the induced frequency shift. The acquired data was then interpreted to acquire information about the mechanical and electrical properties of the medium. It was demonstrated experimentally that the frequency shift detected in the scattered EM signal was correlated with changes in stiffness of an agar gel and changes in conductivity in a sheep kidney [38].

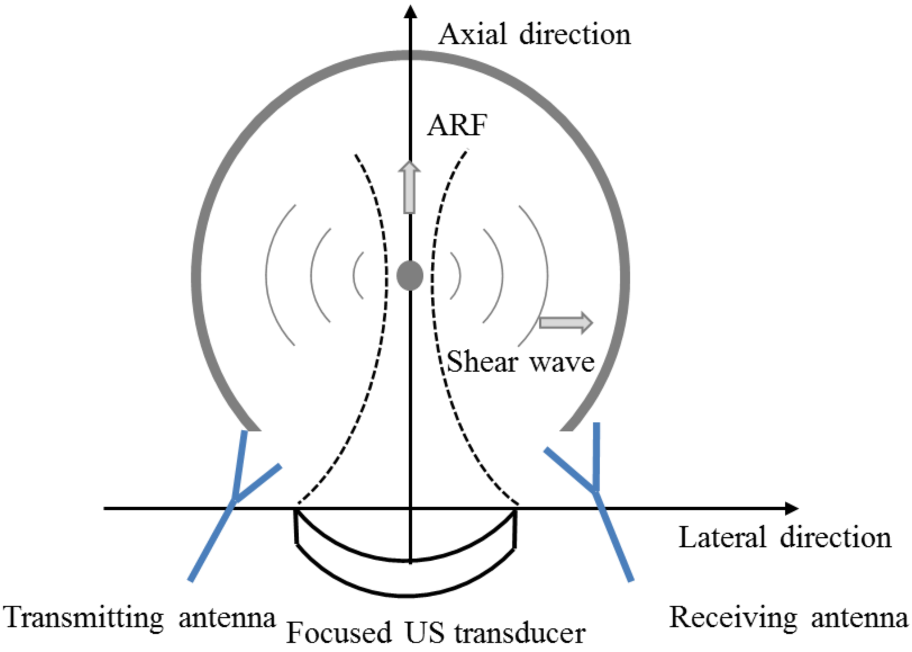

Figure 1.1 Schematic of the EMA imaging system developed at the University of Oxford. A focused ultrasound transducer was used to produce a time varying ARF. Horn antennas operating at 434 MHz were used to transmit EM signals into the tissue and receive scattered signal. The system employed a phased-locked-loop and locked in amplifier to demodulate the scattered EM signal [39].*The grey circular arc is the boundary of the soft tissue.*

However several issues were identified with the experimental approach in these studies. First, the acoustic intensities in the above studies were not well characterised. The clinical deployment of the proposed system for medical diagnostic applications requires the acoustic power to be within the prescribed safety limits. Second, it was not recognised at the time that the EM reflections from the phantom outside the region of excitation, e.g., the water-air interface and the surrounding experimental apparatus, would be likely to degrade signal quality by contributing to the energy at the carrier frequency (434 *MHz*)

This thesis focuses on developing a complete and computational model for the EMA imaging. The EMA model will help associate the characteristics of the scattered EM signals to the variations in mechanical and electrical properties of the underlying tissue. It can also guide the development of new experimental configurations which should result in better performance.

One solution for modelling the EMA imaging would be a "brute force" computational analysis that uses a multi-physics solver to account for the ultrasound propagation, tissue deformation and EM scattering processes simultaneously. Two particular problems arise from this approach [40]. The first problem is that very fine spatial discretization is required to resolve the μm scale vibration from the cm scale wavelength of the EM waves. This leads to unaffordable computational time and memory requirements. The second problem is that the induced frequency shift is very small. In the frequency spectrum, the sidelobes corresponding to the Doppler effect are many orders smaller (-40~-70 dB) compared to that of the carrier signal, which makes them very difficult to calculate accurately.

One approach that has been employed to address the issue of calculating the EM scattering is the sheet boundary condition (SBC). The SBC was developed by the University of Michigan Radiation Laboratory [41] [42] [43] [29]. This class of time varying boundary condition can be applied to the boundaries of a stationary object to account for the motion of the object. A detailed discussion of SBC is found in Section 3.3. Simulations that combine SBC with the Finite Difference Time Domain (FDTD) method have been successfully applied to solve for the EM wave scattering by vibrating cylinders of infinite length in 2D space in both Transverse Electric (TE) and Transverse Magnetic (TM) cases [40]. The SBC technique was firstly applied in medical scenario by Zhao and Varghese [44]. A region of diseased tissue was modelled as infinite cylinder and clinically relevant material parameters were assigned to diseased and healthy tissue respectively. The simulation results confirmed the potential of the EMA imaging in the medical field. It is noted that these prior investigations employed an unfocused acoustic source or external compression to cause deformation of the underlying structure instead of using focused acoustic excitation [38] [39]. In addition the diseased tissue and healthy tissue were modelled as cylinders in 2D space, which is not adequate to account for the complex geometry of imaged targets in clinical applications such as tumours and thermal lesions.

1.4 Breast tumour screening

Breast cancer is one of the most common causes of death from cancer in females in economically developed countries. In addition, epidemiological data suggest that the incidence rate of female breast cancer will increase in less developed countries as these countries becomes more developed through social and economic change [3]. Early detection of breast cancer opens up the possibility of wider range of treatment options, allows less aggressive surgery being performed and leads to a reduced risk of mortality from breast cancer [45]. The guidelines by American Cancer Society for breast cancer screening recommend mammography (X-ray based imaging) be used for annual screening and MRI for screening women of high lifetime risk patients (~20%-25% or greater). Sometimes breast ultrasound is also used to examine abnormalities found from a mammogram screening, particularly in cases where breast tissue appears denser on a mammogram. Both MRI and ultrasound imaging are used as complementary tools to mammography rather than as replacement [46].

Despite mammography being the single most effective method for early breast cancer detection, there are certain problems associated with it. It is not 100% effective and does not perform well in detecting breast cancer in radiographically dense breast [47]. The sensitivity and specificity reported in a clinical trial of film and digital mammography is 65.8% - 89.9% and 88% - 93.1% respectively, depending on the age group of the scanned patient, the type and status of the cancer [48]. False-positive results in a large number of unneeded biopsies which results in risks and stress for patients. Mammography is also a relatively high-cost screening approach which can restrict its use in countries with limited healthcare infrastructure.

The problems with mammography provide an opportunity for other imaging techniques, based on alternative contrast, to be developed as complementary methods. For example, microwave breast imaging is motivated by the relatively high contrast in electrical properties between the malignant breast tissue and the healthy breast tissue. Several other imaging techniques aim to diagnose cancer by exploiting the contrast in elasticity [49] between cancerous tissue and healthy breast tissue. In this thesis, the EMA imaging is evaluated as a complementary technique to be used with existing methods to enhance the breast tumour detection methods.

1.5 HIFU monitoring

High intensity focused ultrasound (HIFU) is an emerging therapeutic method for the treatment of solid tumours. The deposition of high level energy via a focused ultrasound beam causes rapid temperature elevation at the focus of the ultrasound transducer and induces localized and irreversible denaturation of the targeted tumour tissue [50] [51] [52] [53]. The benefits are that it is non-invasive, has few side effects and is relatively cheap.

One of the main barriers to widespread use of HIFU is the inability to reliably form lesions. This means robust imaging methods are required to monitor tissue ablation in real time during HIFU. Substantial progress has been made by various groups and a number of monitoring approaches have been developed or under continuous development. MRI-based temperature imaging (thermometry) is the standard non-invasive method for monitoring HIFU treatment. A number of MR parameters such as T_1, T_2 relaxation, proton resonance frequency and magnetization transfer coefficient are temperature dependent. Using a temperature sensitive sequence, MRI-based thermometry can provide quantitative spatial maps of temperature rise induced during thermal therapies [54] [55]. However several drawbacks such as low frame rate (long image acquisition time), high cost and the need for magnetic compatible HIFU apparatus are limiting the wider clinical usage of MRI-based approaches. Other methods being developed include ultrasound thermometry to monitor temperature elevation [56], B-mode ultrasound image that detects the hyper-echogenic change caused by cavitation [57], ARF-based elasticity imaging technique that detects the stiffness change in tissue associated with the coagulation process [52] [23], passive acoustic technique that monitors the acoustic emission from the ultrasound focus during HIFU exposure [58], and photoacoustic technique that exploits the optical absorption contrast [59].

Our motivation for using EMA imaging for HIFU monitoring is that the electrical relative permittivity and conductivity of soft tissue are reported to be temperature dependent [60]. Therefore the EMA imaging has the potential to detect the changes in the electrical contrast between coagulated tissue and untreated tissue which can in turn be used to indicate the formation of thermal lesion. Compared to MRI based monitoring method, the author expects the EMA imaging to be of lower cost and more convenient to use.

1.6 Thesis organisation

In this chapter, motivation and appropriate background are provided for EMA imaging in diagnosis and therapy. The rest of the thesis proceeds as follows:

Chapter 2 derives an approximate analytical solution for the EM scattering from an oscillating electrically small dielectric sphere using a quasi-stationary approach. The analytical solution reveals the spectral and spatial characteristic of the scattered EM signal which provides a benchmark solution for numerical simulations conducted in subsequent chapters. The Sheet Boundary Condition (SBC) is combined with a Finite Element Method (FEM) simulation to improve the efficiency of the scattered EM field simulation. The simulation results for EM scattering from dielectric cylinders in different modes of vibration are compared to corresponding analytical solutions for validation.

A complete model for the EMA imaging in 3D space is developed in Chapter 3. The developed simulation framework, which is the major contribution of the thesis, includes an acoustic model to model the propagation of ultrasound wave through tissue, a linear-viscoelastic model to estimate the dynamic response of soft tissue to acoustic excitation, and electromagnetic (EM) models to evaluate both the regular EM scattering as well as the Doppler Effect in the scattered EM signal.

The application of the EMA imaging to breast tumour detection is investigated in Chapter 4. Using the simulation framework developed in Chapter 3, breast tumours are modelled as spherical inclusions buried in homogeneous background tissue assigned with clinically realistic material properties. The suitability of the EMA imaging as a breast tumour detection method is discussed.

Chapter 5 evaluates the feasibility of using the EMA imaging to monitor thermal lesion formation during HIFU therapy. A HIFU simulator is incorporated into the developed simulation framework in Chapter 4. The signal of the EMA imaging during a thermal exposure is simulated with acoustic and material parameters varied in clinically feasible range.

In Chapter 6, conclusions are drawn and topics of future research are discussed.

Chapter 2 EM Scattering from oscillating spheres and vibrating cylinders

2.1 Introduction

In EMA imaging (see Section 1.3.3 for more details), the localized oscillation of the soft tissue induced by an ARF is monitored by means of electromagnetic (EM) waves which illuminates the target and which are then scattered by contrast in the tissue. Understanding the spatial and spectral characteristics of the scattered EM waves is important to order to develop a theoretical framework for the EMA imaging. In medical applications of the EMA imaging, the geometry of the underlying tissue, e.g., a breast tumour is often of irregular shape and does not always oscillate as a rigid body under acoustic excitation because of its finite stiffness. This problem is not tractable analytically and in this chapter a numerical method is developed to model the Doppler spectrum of the EM wave scattered by arbitrarily vibrating objects of irregular geometries.

The chapter is organised as follows: in Section 2.2 an analytical investigation is performed for a plane EM wave incident on an electrically small dielectric sphere in harmonic oscillation. An approximate solution of the scattered EM wave is developed using a quasi-stationary approach. It is noteworthy that the sole purpose of this section is to derive a benchmark solution for the Doppler EM scattering (by an oscillating object) model in the 3D EMA model (see Section 3.5). Therefore the acoustic stimulation and linear-viscoelastic deformation are not considered here. A rigid sphere is assumed to oscillate harmonically without specifying the cause of such a motion. In Section 2.3 the principle of sheet boundary condition (SBC) is introduced in order to improve the efficiency of the numerical simulation of the EM scattering. The expression of the SBC that is compatible with a frequency domain simulation is developed. In Section 2.4 a model for simulating the bi-static scattering of a plane EM wave by dielectric cylinders in different vibration modes based on the SBC and Finite Element Method (FEM) is developed and validated using known analytical solutions.

2.2 EM Scattering from an electrically small dielectric sphere in harmonic oscillation

The theory of EM scattering by a finite-sized, stationary sphere has been well established. The solution for the EM scattering problem by a moving sphere has been derived using the Lorentz transformation, which is only valid for a sphere moving at a constant velocity [61] [62]. In this section, an approximate solution for the scattered EM wave by an oscillating electrically small dielectric sphere is developed using a quasi-stationary approach.

A quasi-stationary approach evaluates the scattered EM wave at the observer's position at a time instant by assuming the scatterer is stationary at the position it occupies (i.e. it neglects the motion of the scatterer during the travel time of the EM wave from the source to the scatterer, and from the scatterer to the observer). The conditions which need to be satisfied when applying a quasi-stationary approach are 1) a small maximum velocity v of the scatterer relative to the EM propagation speed and 2) maximum acceleration of the scatterer much smaller than vf_{em}, where f_{em} (434 MHz for EMA imaging) is the frequency of EM wave [63] [64] [65] [66] [67]. The harmonic motion of the tissue involved in the EMA imaging does not exceed amplitude of 100s μm and is of a frequency of 100s Hz. The velocity and the acceleration of the scatterer are estimated to be no greater than 0.02 m/s and 3 m/s^2 respectively, and therefore the two conditions are satisfied.

Derivation:

An electrically small (the size of the scatterer much smaller than a wavelength of the EM wave) sphere P of radius a is placed at the origin of the Spherical coordinates as shown in Figure 2.1. A monochromatic plane EM wave polarized in the z direction and travelling in the +y direction is incident on the sphere at the origin. The plane EM wave can be described by

$$E_i = E_0 e^{j\omega_{em}t} e^{-jk_{em}y} \tag{2.1}$$

For the case where P is stationary, the scattered EM wave in the far field is equivalent to the radiated field of a Hertzian dipole for $k_{em}a \ll 1$ [68], where k_{em} is the wavenumber of the EM wave. Assuming an observer is located at an arbitrary location $\vec{\boldsymbol{r}} = (r, \theta, \varphi)$ in the spherical coordinates, the scattered EM wave is [68],

$$\begin{aligned} E_s &= -\hat{\boldsymbol{\theta}} \frac{jk_{em}(j\omega_{em}p)}{4\pi r \varepsilon_0 c_0} \cos(\theta)\, e^{-jk_{em}r} e^{j\omega_{em}t} \\ &= \hat{\boldsymbol{\theta}} E_{amp} \cos(\theta)\, e^{-jk_{em}r} e^{j\omega_{em}t} \end{aligned} \tag{2.2}$$

where $\hat{\boldsymbol{\theta}}$ is the unit vector in θ direction and r is the distance from the observer to P. The momentum p of the induced Hertzian dipole is given by,

$$p = 4\pi\varepsilon_0 a^3 \left(\frac{\varepsilon_1 - \varepsilon_0}{\varepsilon_1 + 2\varepsilon_0}\right) E_0 \tag{2.3}$$

Here ε_0 and ε_1 are the permittivity of the background medium and the material of P respectively.

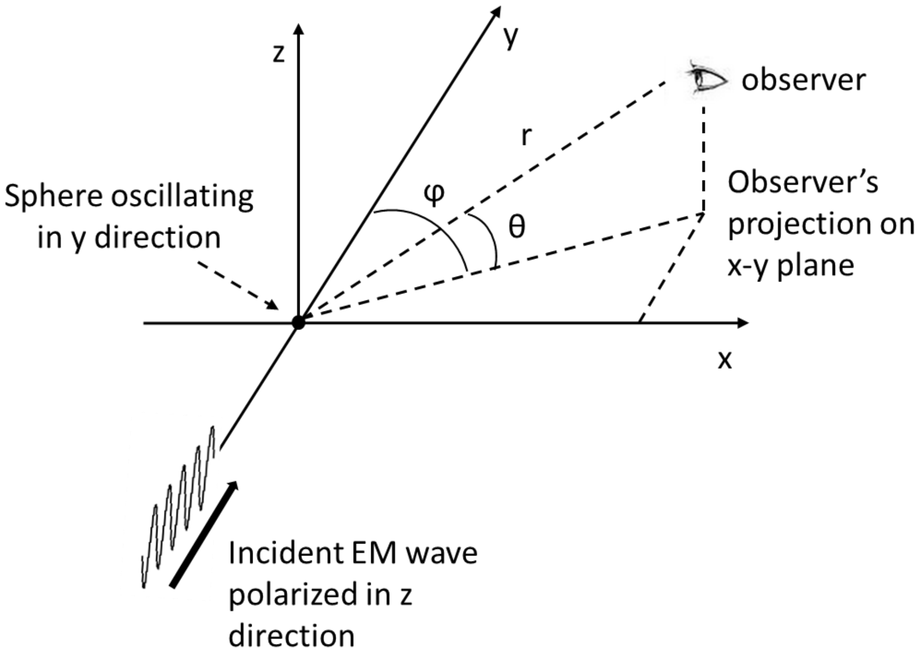

Figure 2.1 An oscillating electrically small sphere is oscillating in a sinusoidal manner along the y axis about the origin as described by Equation 2.4. A monochromatic plane EM wave described by Equation 2.1 travels in the +y direction and is incident of the sphere. The scattered EM wave is observed at an arbitrary location described by the spherical coordinate (r, θ, φ).

Now the sphere is assumed to oscillate in y direction about of the origin, which is described by,

$$y(t) = Asin(\omega_o t)\hat{\boldsymbol{y}} \tag{2.4}$$

where $\hat{\boldsymbol{y}}$ is the unit vector in y direction. Assuming P is stationary, the transmitter and observer are oscillating relative to P. In the first step, ignoring the relative motion between the observer and the scatterer, the scattered EM wave propagates an extra distance due to the oscillation of the transmitter, has an additional phase shift, and is described by

$$E'_s = \hat{\boldsymbol{\theta}} E_{amp} \cos\theta e^{j\omega_{em}t} e^{-jk_{em}r} e^{-jk_{em}Asin(\omega_o t)} \tag{2.5}$$

Here $e^{-jk_{em}Asin(\omega_o t)}$ is introduced to account for the phase change due to the extra EM propagation. As the velocity of the oscillation of the sphere is much smaller than the speed of the EM wave, the amplitude modulation in the scattered EM wave due to the relativistic effect is neglected and therefore the term E_{amp} in Equation 2.2 is not altered. In the second step, when the relative motion between the observer and the scatterer is considered, the observer sees only the Doppler effect induced by the motion in the direction of the observer. The displacement of P relative to the origin in the direction of observer can be described by

$$Y(t) = -Asin(\omega_o t)\cos\theta\cos\varphi\hat{\boldsymbol{r}} \tag{2.6}$$

where $\hat{\boldsymbol{r}}$ is the unit vector in the direction of observer. The displacement of the observer relative to P is described by

$$Y(t) = r\hat{\boldsymbol{r}} + Asin(\omega_o t)\cos\theta\cos\varphi\hat{\boldsymbol{r}} \tag{2.7}$$

and the scattered E field seen by the observer is given by

$$E_s(\vec{\boldsymbol{r}}) = \hat{\boldsymbol{\theta}} E_{amp} \cos\theta e^{j\omega_{em}t} e^{-jk_{em}r} e^{-jk_{em}A(1+\cos\theta\cos\varphi)\sin(\omega_o t)} \tag{2.8}$$

$E_s(\vec{\boldsymbol{r}})$ can be written in terms of Bessel functions with the term $e^{-jk_{em}r}$ supressed,

$$E_s(\vec{\boldsymbol{r}}) = \hat{\boldsymbol{\theta}} E_{amp} \cos\theta \cdot \sum_{n=-\infty}^{\infty} (-j)^n J_n((1+\cos\theta\cos\varphi)k_{em}A) e^{j(\omega_{em}-n\omega_o)t} \tag{2.9}$$

The Fourier transform of Equation 2.9 is then given by

$$\mathcal{F}\ (E_s(\vec{\boldsymbol{r}})) = \widehat{\boldsymbol{\theta}} E_{amp} \cos\theta \cdot \sum_{n=-\infty}^{\infty} (-j)^n J_n((1+\cos\theta\cos\varphi)k_{em}A)\delta(\omega - \omega_{em} + n\omega_o) \tag{2.10}$$

Discussion:

Equation 2.10 describes a Doppler spectrum of discrete sidebands at intervals of ω_o as shown in Figure 2.2. In the EMA imaging, the magnitude of the displacement of the target is much smaller than a wavelength of the EM wave (i.e. $k_{em}A \ll 1$). Therefore the small argument approximation [69] is applicable

$$J_n((1+\cos\theta\cos\varphi)k_{em}A) = (-1)^n J_{-n}((1+\cos\theta\cos\varphi)k_{em}A) \approx \frac{1}{(n)!}\left(\frac{(1+\cos\theta\cos\varphi)k_{em}A}{2}\right)^n \tag{2.11}$$

For n = 0, the frequency of the scattered EM wave is the same as the incident EM wave, therefore it is referred to as the unshifted component (UC). For n = 1 and $k_{em}A \ll 1$, the corresponding sideband is referred to as the first Doppler component (FDC) and it is proportional to the amplitude of the oscillation of the sphere A. Furthermore, Equation 2.11 suggests that the amplitude of the higher order Doppler components (n>=2) are much smaller than the FDC. Therefore in the rest of the study, the FDC is evaluated to quantify the tissue response in the EMA imaging.

The directivity of the FDC of the EMA signal is $\cos\theta(1+\cos\theta\cos\varphi)$ and is shown as functions of φ and θ in the y-x plane and the y-z plane respectively in Figure 2.3a and b. The observed pattern corresponds to the Doppler effect observed at different angle modulated by the scattering pattern of a stationary sphere. The strongest Doppler component is observed at the backward scattering position and a null is observed at the forward scattering position.

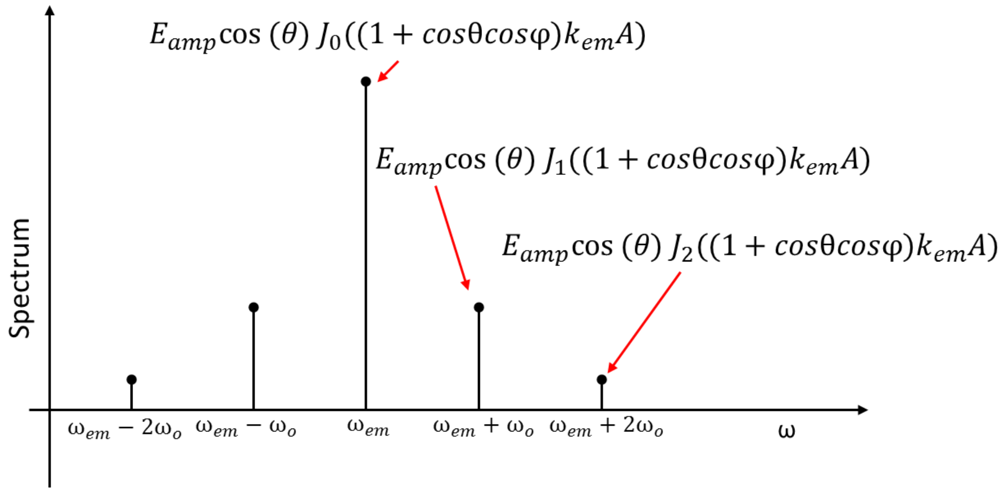

Figure 2.2 The spectrum of an EM wave scattered by an oscillating dielectric sphere. The sidebands are a result of the Doppler effect. The two sidebands at $\omega_{em}\pm\omega_0$ *are first Doppler components. Other sidebands are very small according to the small argument approximation and are omitted from the discussion.*

The solution presented here determines the Doppler effect by considering the extra phase change due to the motion of sphere using the solution. It neglects the phase modulation while the signal is propagating inside the dielectric sphere. Without considering the phase modulation internal to the spherical boundary, the derived solution is only approximately valid when the difference in electrical properties between the sphere and background medium is small.

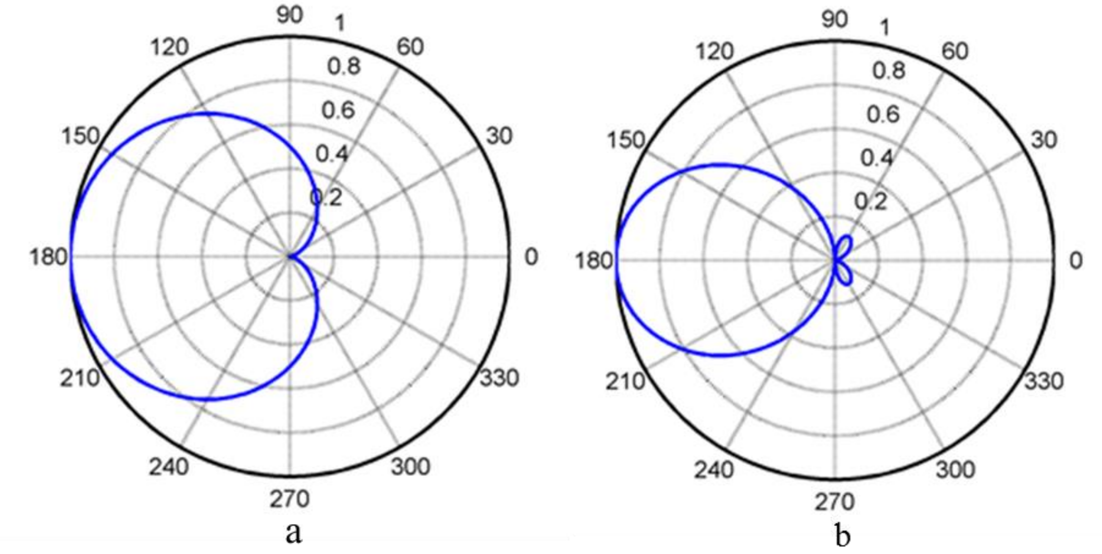

Figure 2.3 The directivity of the FDC in the scattered EM signal as functions of (a) φ is the x-y plane and (b)θ is the y-z plane.

2.3 Sheet boundary condition

The sheet boundary condition (SBC) is introduced to solve the two problems associated with a “brute force” model of EMA imaging in Section 1.3.3. Figure 2.4 depicts the principle of the SBC. A vibrating object of electrical properties (ε_2, μ_2) placed in a background medium (ε_1, μ_1) is modelled by two stationary bodies, one with constant (ε_2, μ_2) and the second with a sheet of impedance and admittance$(Z_i^s(t),\ Y_i^s(t))$ that is a function of time. The scattered EM signal by the vibrating object is equivalent to the sum of the scattered EM signals by the first stationary object which is equivalent to the UC and the second stationary object with a time varying SBC which is equivalent to the FDC. The SBC approach is applicable to scatterers of any geometries and arbitrary vibration as along as amplitude of vibration is small compared to a wavelength of the EM wave [42]. It is also applicable to electrically small scatterers although higher order boundary condition may be required.

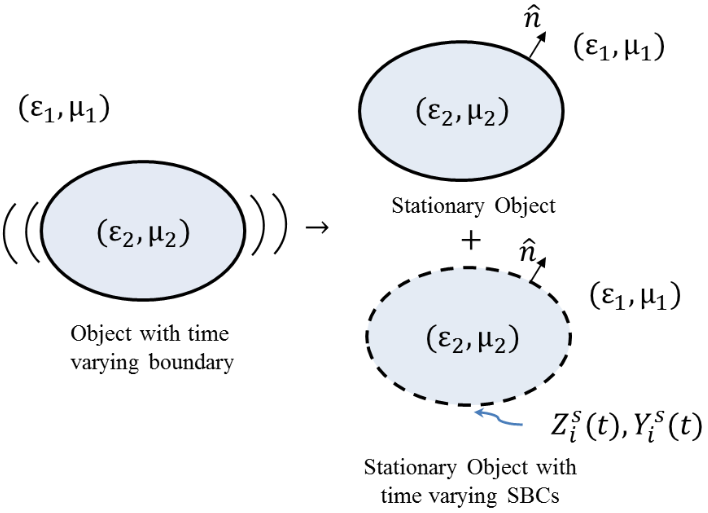

Figure 2.4 Illustration of the sheet boundary condition: The vibrating object can be replaced by a stationary object and a stationary object with a time-varying SBC. The EM signal scattered by the former is equivalent to the UC and the latter equivalent to the FDC.

Across the surface of the object, to the first order, the expression of the general SBC is given by [40],

$$\begin{aligned} \hat{n} \times (\boldsymbol{E_1} - \boldsymbol{E_2}) &= \hat{n} \times \hat{n} \times (Z_1^s \boldsymbol{H_1} + Z_2^s \boldsymbol{H_2}) \\ -\hat{n} \times (\boldsymbol{H_1} - \boldsymbol{H_2}) &= \hat{n} \times \hat{n} \times (Y_1^s \boldsymbol{E_1} + Y_2^s \boldsymbol{E_2}) \end{aligned} \tag{2.12}$$

with the sheet impedance Z_i^s and admittance Y_i^s given by

$$\begin{aligned} Z_1^s &= -jk_{em1}\xi Z_1 \qquad Z_2^s = +jk_{em2}\xi Z_2 \\ Y_1^s &= -jk_{em1}\xi / Z_1 \qquad Y_2^s = +jk_{em2}\xi / Z_2 \end{aligned} \tag{2.13}$$

where the subscript 1 and 2 denote the medium external and internal to the object boundary respectively, $\hat{n}$ is the outward unit vector normal to the boundary, Z_i and k_{emi} are the intrinsic impedance and the wavenumber, and ξ is the local displacement normal to the object boundary and is, therefore, time-varying for a vibrating object.

Second order boundary conditions for TM is

$$\hat{n} \times (\boldsymbol{E_1} - \boldsymbol{E_2}) = \hat{n} \times \hat{n} \times \left(\eta_1^s \boldsymbol{H_1} + \frac{\partial}{\partial s}\left(B_1 \frac{\partial}{\partial s} \boldsymbol{H_1}\right) + \eta_2^s \boldsymbol{H_2} + \frac{\partial}{\partial s}\left(B_2 \frac{\partial}{\partial s} \boldsymbol{H_2}\right)\right) \tag{2.14}$$

and for TE is

$$-\hat{n} \times (\boldsymbol{H_1} - \boldsymbol{H_2}) = \hat{n} \times \hat{n} \times \left(\gamma_1^s \boldsymbol{E_1} + \frac{\partial}{\partial s}\left(A_1 \frac{\partial}{\partial s} \boldsymbol{E_1}\right) + \gamma_2^s \boldsymbol{E_2} + \frac{\partial}{\partial s}(A_2 \frac{\partial}{\partial s} \boldsymbol{E_2})\right) \tag{2.15}$$

with

$$\begin{gathered}
\eta_1^s = -jk_{em1}\xi Z_1 \qquad \eta_2^s = +jk_{em2}\xi Z_2 \\
\gamma_1^s = -jk_{em1}\xi / Z_1 \qquad \gamma_2^s = +jk_{em2}\xi / Z_2 \\
A_1 = \frac{-j\xi}{k_{em1} Z_1} \qquad A_2 = \frac{-j\xi}{k_{em2} Z_2} \\
B_1 = \frac{+j\xi Z_1}{k_{em1}} \qquad A_2 = \frac{+j\xi Z_2}{k_{em2}}
\end{gathered} \tag{2.16}$$

By converting the boundary in motion to a time-varying SBC on a stationary body the spatial discretisation in the numerical simulations (e.g. FDTD) can be done with respect to the EM wave without considering the amplitude of vibration. Therefore, the first problem described in Section 1.3.3 is circumvented. It is emphasised that the

SBC separates the total scattered wave E_s from a vibrating object into two parts: the UC and the FDC, and allow them to be calculated separately, thereby the second problem described in Section 1.3.3 is avoided.

To find the appropriate expression of the SBC compatible with frequency domain EM simulation, the object boundary is discretized into a collection of small patches $P_1 \dots P_m$ as shown in Figure 2.5. For an object oscillating periodically at ω_o, the function of the transient displacement of an elementary patch normal to the boundary can be written in the form of a Fourier series,

$$\xi(m,t) = \sum_{n=0}^{\infty} \Gamma_{mn} \cos(n\omega_o t + \theta_{mn})\,\hat{n}_m \tag{2.17}$$

where ω_o is the principal angular frequency of the vibration. In EMA imaging ω_o is associated with the frequency of the ARF excitation. n is the index for the normal Fourier modes and m the index for the elementary patches, Γ_{mn} is the amplitude and θ_{nm} the phase of the oscillatory displacement. $\hat{n}_m$ is the unit vector normal to the m^{th} elementary patch and depends on instantaneous position of the element patch. Note the equivalent sheet impedance and admittance are linearly related to ξ, and therefore so is the FDC in the scattered EM wave as shown in Equation 2.12 to Equation 2.16. This is consistent with the analytical solution in Section 2.2. In the frequency domain, the vibration function for each normal Fourier mode is written in complex notation,

$$\Gamma_{mn}\cos(n\omega_o t+\theta_{mn})\hat{n}_m \xrightarrow{Fourier} \pi\,\Gamma_{mn}\cdot\exp(j\theta_{mn})(\delta(\omega-n\omega_o) + \delta(\omega+n\omega_o)) \tag{2.18}$$

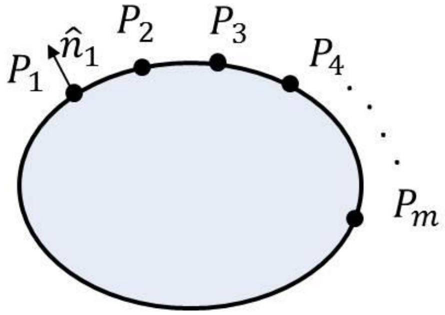

Figure 2.5 The object boundary is discretized into a collection of small elementary patches

The FDC induced by each normal Fourier mode n can be calculated by replacing the vibration function ξ in Equation 2.12 to Equation 2.16 by the complex notation in Equation 2.18. Summing up the Doppler components of different normal Fourier modes allows the Doppler effect induced by a periodic vibration to be evaluated.

2.4 A FEM-SBC model in 2D

2.4.1 Introduction to the investigated problem

As has been discussed in Section 2.2, only the amplitude of the FDC is evaluated. For vibration of a single normal Fourier mode, only two numerical simulations are needed [40] [44]: the first simulation is conducted to compute the UC by the stationary object and a second simulation is conducted to compute the FDC. Here a Finite Element Model (FEM) is used to solve the scattering of EM waves which is implemented as a module in 'Comsol Multiphysics^{TM}'. From here on the combinatorial use of the FEM and the SBC will be referred to as the FEM-SBC.

The purpose of the following investigation is to validate the proposed SBC-FEM. In the following section, SBC-FEM is applied to the problem of EM scattering from a vibrating cylinder for which the analytical solution is known. The FDC of the EM wave scattered by a vibrating dielectric circular cylinder is computed using SBC-FEM. The result is compared to known the analytical solution. The principles employed in the 2D analysis will be extended to modelling of the EMA in 3D in Chapter 3.

A circular dielectric cylinder in polar coordinates is shown in Figure 2.6. Considering the incidence of a time-harmonic plane acoustic wave travelling in +y direction on a dielectric cylinder of radius a, the analytical solutions of the vibration of the cylinder have been derived for a series of radial resonance mode N [70]. In the following investigation, the dielectric cylinder is assumed to vibrate such that the radial displacement of the cylindrical boundary is given by [40]

$$\xi(\varphi', t) = \sum_{N=0}^{\infty} \Gamma_N \cos(N\varphi') \cos(\omega_0 t + \theta_N) = \sum_{N=0}^{\infty} \xi_N(\varphi', t) \tag{2.19}$$

where ω_0 is the angular frequency of vibration. Note that Equation 2.19 corresponds to Equation 2.17 with m replaced by φ' in the polar coordinates and Γ_{mn} replaced by $\Gamma_N \cos(N\varphi')$. The Fourier transform of the radial displacement of resonance mode N is written as,

$$\xi_N(\varphi', t) \xrightarrow{Fourier} \Xi_N(\varphi', \omega) \tag{2.20}$$

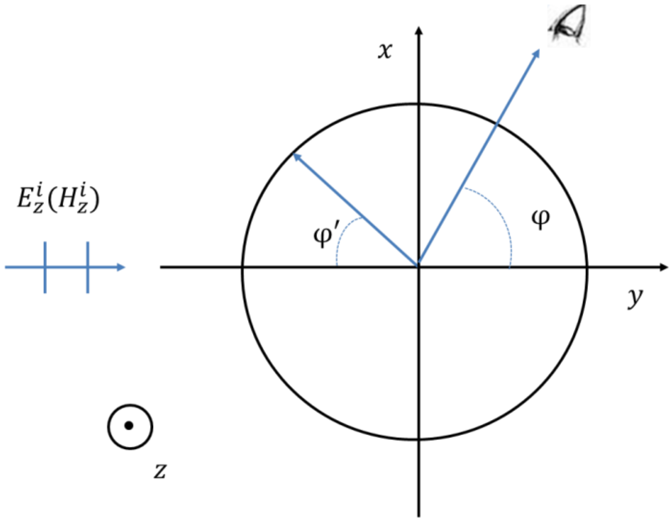

Figure 2.6 The TM (TE) incidence of an EM wave on a circular dielectric cylinder of radius a. The EM wave travels in +y direction. The observer is located at a location (r, φ) in polar coordinates.

2.4.2 Method: TM case

The incident plane EM wave, with electric field polarized in z direction (parallel to the axis of the cylinder), of frequency ω_{em} and propagating along y axis, can be expressed as,

$$E_z^i(r,\varphi) = E_0 e^{-jk_{em1}\, r\cos\varphi} \tag{2.21}$$

The analytical solution of the scattered electric field external to a vibrating dielectric cylinder is given by [29],

$$E_z^s(r,\varphi) = E_0 \sum_{n=-\infty}^{\infty} (-j)^n A_n^{TM}(1+C_n^{TM}k_{em1}b)H_n^{(2)}(k_{em1}r)e^{jn\varphi} \tag{2.22}$$

with

$$A_n^{TM} = \frac{\frac{\eta_1}{\eta_2}J_n(k_{em1}a)J_n'(k_{em2}a) - J_n'(k_{em1}a)J_n(k_{em2}a)}{J_n(k_{em2})H_n^{(2)}{}'(k_{em1}a) - \frac{\eta_1}{\eta_2}J_n'(k_{em2}a)H_n^{(2)}(k_{em1}a)} \tag{2.23}$$

$$B_n^{TM} = \frac{-2j/\pi k_{em1}a}{J_n(k_{em2})H_n^{(2)}{}'(k_{em1}a) - \frac{\eta_1}{\eta_2}J_n'(k_{em2}a)H_n^{(2)}(k_{em1}a)} \tag{2.24}$$

and

$$C_n^{TM} = \frac{j^n J_n(k_{em2}a)}{\frac{\eta_1}{\eta_2}J_n(k_{em1}a)J_n'(k_{em2}a) - J_n'(k_{em1}a)J_n(k_{em2})}\sum_{p=-\infty}^{\infty}\xi_{n-p}(t)V_p$$

$$V_p = j^{-p}\left[-J_p''(k_{em1}a) - A_p^{TM}H_p^{(2)}{}''(k_{em1}a) + \frac{k_{em2}^2}{k_{em1}^2}B_p^{TM}J_p''(k_{em2}a)\right] \tag{2.25}$$

where subscript 1 and 2 denote the regions external and internal to the cylindrical boundary respectively, η_i and k_{emi} are the impedance and wavenumber of the EM wave respectively. J_n and $H_n^{(2)}$ are Bessel function of the first kind and Hankel function of the second kind respectively, $'$ and $''$ denote the first and second derivative of the underlying functions. ξ_{n-p} is the $n-p$ normal Fourier mode of radial displacement (refer to Equation 2.19).

The implementation of the FEM-SBC was realized using a commercial FEM package (Radio Frequency Module of Comsol Multiphysics$^{\text{TM}}$, Comsol Inc, Burlington, MA, USA). As shown in Figure 2.7, in 2D space, a circular region of radius a was created to represent the dielectric cylinder. A larger circular region of radius = 15 *cm* was then created as the background space. The background space was further enclosed by a perfectly matched layer (PML) with a thickness of 12 cm, and a scattering boundary condition was assigned to the outmost boundary of the PML. The PML together with the scattering boundary condition ensured that the outgoing EM waves were sufficiently absorbed with a maximum reflection of -94 dB. Triangular meshes were generated using the mesh generator in Comsol. Adaptive meshing was employed resulting a finer meshing in regions closer to the boundaries of high curvature. In total, mesh consisted of 19972 elements.

In the first step, the electric field E_z^1 external to the boundary of the cylinder was recorded, which was later used for the simulation of the FDC. The scattered electrical field 15 *cm* away from the centre of the dielectric cylinder was also recorded as the

UC. In the second step, the FDC was solved as the radiation from an equivalent current distributed on the dielectric cylinder boundary. The current density was calculated using

$$
\begin{aligned}
J_z(\varphi') = \hat{n} \times \hat{n} \times \Big\{ & -j(\varepsilon_2 - \varepsilon_1)\omega_{em} \cdot \Xi(\varphi', \omega_0) E_z^1(a, \varphi') \\
& + \frac{\partial}{\partial s} \Xi(\varphi', \omega_0) \frac{1}{j\mu_1 \omega_{em}} \left(\frac{1}{\mu_1} - \frac{1}{\mu_2}\right) \frac{\partial E_z^1(a, \varphi')}{\partial s} \Big\}
\end{aligned}
\tag{2.26}
$$

where the direction tangential to the dielectric cylinder boundary, perpendicular to the 2D plane of simulation is denoted by the subscript z and lying in the 2D plane denoted by s. The equivalent version of Equation 2.26 in time domain analysis can be found in [40].

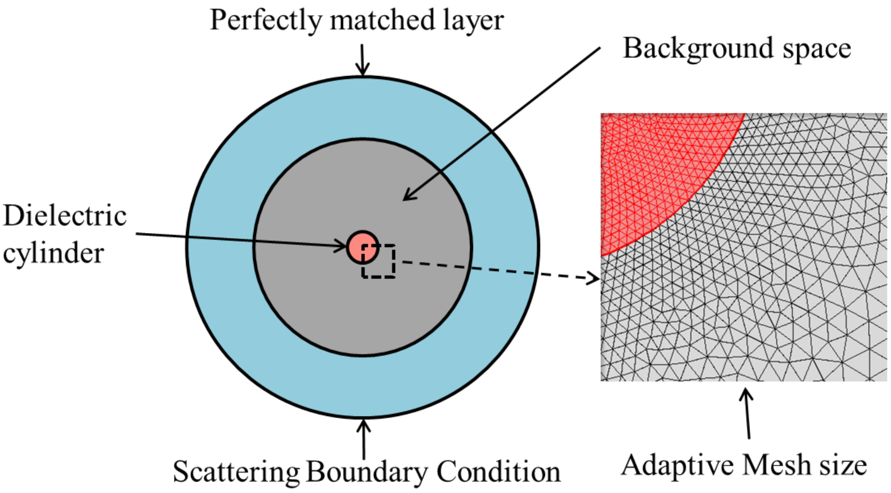

Figure 2.7 The FEM-SBC model of a dielectric cylinder built in the FEM package. The model is composed of a circular cylinder (pink), a circular background space (grey) and a perfectly matched layer (blue).

2.4.3 Method: TE case:

In the TE case, the incident magnetic field can be described as,

$$H_z^i(r,\varphi) = H_0 e^{-jk_{em1}\, r\cos\varphi} \tag{2.27}$$

The analytical solution of the scattered electric field with TE incidence is given by [71]

$$\begin{aligned} E_{tan}^s(r,\varphi) = \frac{j}{\eta_1} \sum_{n=-\infty}^{\infty} \chi \cdot j^{-n} A_n^{TE} (1 \\ + C_n^{TE} k_{em1} \Gamma) \left[\frac{\beta j n}{k_{em1} r} H_n^{(2)}(k_{em1} r) \right. \\ \left. - H_n^{(2)\prime}(k_{em1} r) \right] e^{jn\varphi} \end{aligned} \tag{2.28}$$

with

$$\begin{gathered} C_n^{TE} = \frac{j^n}{J_n(k_{em1}a) J_n'(k_{em2}a) - \frac{\eta_1}{\eta_2} J_n'(k_{em1}a) J_n(k_{em2}a)} \\ \sum_{p=-\infty}^{\infty} A_{n-p}(t) \left[\frac{\eta_1}{\eta_2} J_n(k_{em2}a) V_{p,n-p} - J_n'(k_{em1}a) U_p \right] \end{gathered} \tag{2.29}$$

where

$$\begin{aligned} V_{p,n-p} = j^{-p} \left[\frac{-p(n-p)}{(k_{em1}a)^2} B_p^{TE} J_p(k_{em2}a) (1 - \frac{\varepsilon_1}{\varepsilon_2}) - J_p''(k_{em1}a) \right. \\ \left. - A_p^{TE} H_p^{(2)''}(k_{em1}a) + B_p^{TE} J_p''(k_{em2}a) \right] \end{aligned} \tag{2.30}$$

$$U_p = j^{-p} \left[\frac{k_{em2}}{k_{em1}} B_p^{TE} J_p'(k_{em2}a) - A_p^{TE} H_p^{(2)'}(k_{em1}a) + J_p'(k_{em1}a) \right]$$

and

$$A_n^{TE} = \frac{\frac{\eta_2}{\eta_1} J_n(k_{em1}a) J_n'(k_{em2}a) - J_n'(k_{em1}a) J_n(k_{em2}a)}{J_n(k_{em2}a) H_n^{(2)}{}'(k_{em1}a) - \frac{\eta_2}{\eta_1} J_n'(k_{em2}a) H_n^{(2)}(k_{em1}a)} \tag{2.31}$$

$$B_n^{TE} = \frac{-2j/\pi k_{em1}a}{J_n(k_{em2}) H_n^{(2)}{}'(k_{em1}a) - \frac{\eta_2}{\eta_1} J_n'(k_{em2}a) H_n^{(2)}(k_{em1}a)} \tag{2.32}$$

χ and β are associated with the perturbation to the dielectric cylinder boundary due to the vibration and are expressed as,

$$\chi = \left\{ \left[\frac{\xi'(\varphi',t)}{a + \xi(\varphi',t)} \right]^2 + 1 \right\}^{-1/2} \tag{2.33}$$

and

$$\beta = \frac{\xi'(\varphi',t)}{a + \xi(\varphi',t)} \tag{2.34}$$

The FEM-SBC simulation in TE case employed a FEM of the same geometry and setting as described in TM case. The incident field was specified according to Equation 2.27. The equivalent current density was calculated using,

$$\begin{aligned} J_s(\varphi') = \hat{n} \times \Bigg\{ & -j(\varepsilon_2 - \varepsilon_1)\omega_{em} \cdot \Xi(\varphi',\omega_0) E_s^1(a,\varphi') \\ & + \frac{\partial}{\partial s} \Xi(\varphi',\omega_0) \frac{1}{j\mu_1\omega_{em}} \left(\frac{1}{\mu_1} - \frac{1}{\mu_2}\right) \frac{\partial E_s^1(a,\varphi')}{\partial s} \Bigg\} \end{aligned} \tag{2.35}$$

2.4.4 Results and Discussion:

The parameters used in this investigation are summarized in Table 2.1. The bi-static scattering (as shown in Figure 2.6) with TM incidence by a dielectric cylinder resonating at N = 1,2,3 were simulated. The FDC was recorded by moving the receiver in a circular trajectory in the far field 15 *cm* away from the centre of the cylinder. The simulations of the FEM-SBC model were compared to the corresponding analytical solutions and are shown in Figure 2.8. The simulations were in excellent agreement with the analytical solutions. The directivity of the FDC depends heavily on N.

Table 2.1 Summary of parameters employed in the FEM-SBC simulations for EN scattering by dielectric cylinders. f_{em} *is the EM wave frequency,* f_0 *the ARF modulation frequency, N the resonance mode, a the cylinder radius,* ε *the relative permittivity and* μ *the relative permeability.*

Parameter	Background tissue	Tumour tissue
f_{em}	434 *MHz*	
f_o	160 *Hz*	
N	1,2,3	
a	3 *mm*	
$\Xi_{1,2,3}$	0.1 *mm*	
ε	18	100~300
μ	1	1

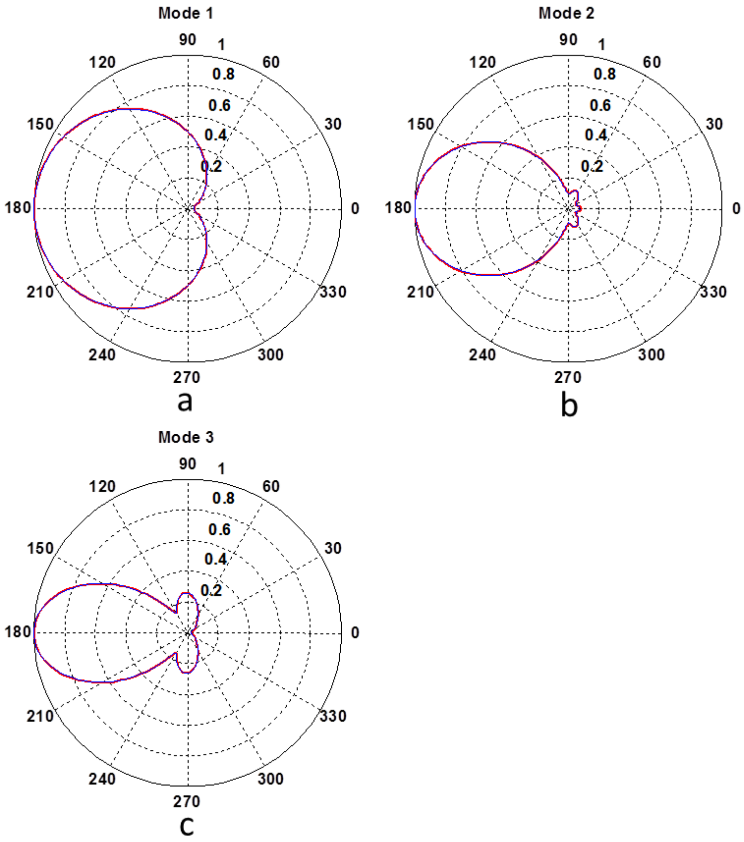

Figure 2.8 The comparison between the FEM-SBC simulations (red) to analytical solutions (blue) of the amplitude of the FDC as a function of the bi-static angle for a vibrating dielectric cylinder that is vibrating at mode 1(a), mode 2(b), and mode 3(c) in TM case.

For all the N investigated, the strongest FDC occurs at the backward scattering position, i.e.,$\varphi = 180°$. Fixing the EM receiver at the backscattering position (180°), the FDC and the UC were obtained as a function the permittivity of the dielectric cylinder ε_2. The FEM-SBC simulations are compared to analytical solutions in Figure 2.9. Excellent agreement was observed. The results show that the variation in the normalized FDC and UC as a function of ε_2 depends on the vibration mode of cylinder. It is also noted that when the scatterer and background are of the same magnetic permeability, the second order term in Equation 2.35 vanishes. The agreement between SBC-FEM solution and analytical solution suggests that the second order boundary condition is not required.

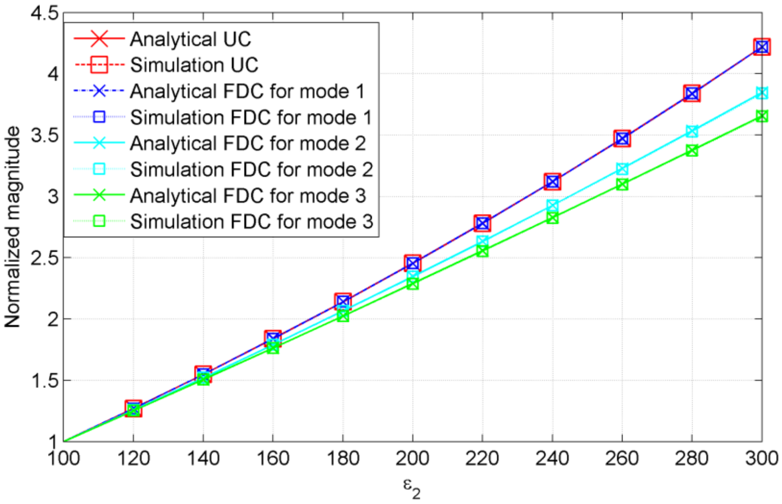

Figure 2.9 The change in the FDC and UC as a function of $\boldsymbol{\varepsilon_2}$ *for the case of TM incidence depends on the mode number N.*

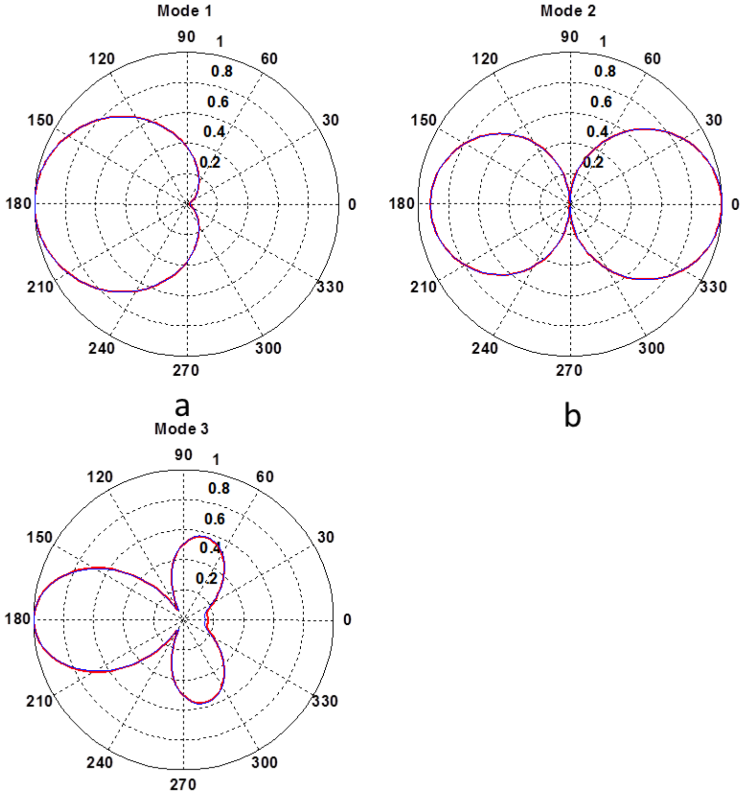

a

b

c

Figure 2.10 The comparison between the simulations (red) to analytical solutions (blue) of the amplitude of the FDC as a function of the bi-static angle for a vibrating dielectric cylinder that is vibrating at mode 1(a), mode 2(b), and mode 3(c) in TE case.

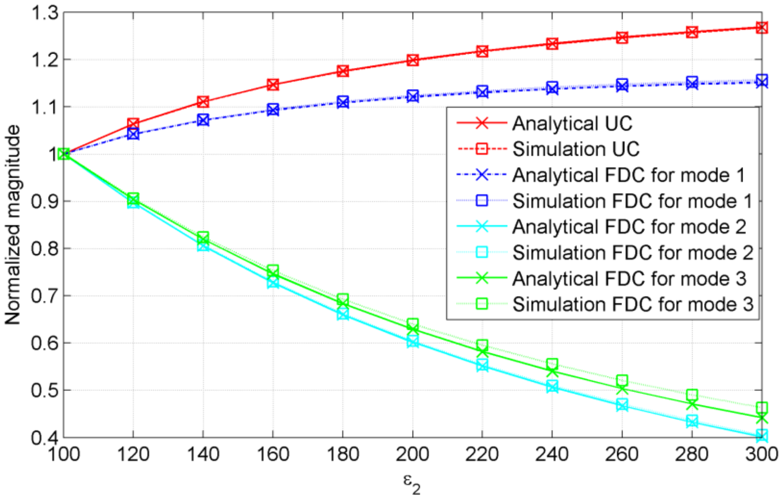

Figure 2.11 The change in the FDC and the UC as a function of $\boldsymbol{\varepsilon_2}$ *for the case of TE incidence depends on vibration mode number N.*

With TE incidence, the electrical field is polarized in the x-y plane. The same investigation in the TM case was repeated for the TE incidence. The FEM-SBC simulations are compared to analytical solutions in Figure 2.10 and Figure 2.11. Excellent agreement between FEM-SBC and analytical results was also observed with TE incidence. Note the scattering pattern of the FDC as functions of φ for different N were different from that in TM case. Especially for N = 2, the strongest FDC was observed at the forward scattering position ($\varphi = 0°$). Figure 2.11 shows that, similar to TM incidence, the variation of the FDC with ε_2 depends on N. The reason for the vibration mode dependence of the FDC is explained by Equation 2.26 and Equation 2.35. Equation 2.26 (Equation 2.35) essentially evaluates the equivalent current which is used as the source of radiation to yield the FDC in a FEM simulation. The current is associated with the cross product of the external electric field tangential to the cylindrical surface and the oscillatory displacement normal to the cylindrical surface. Therefore the resonance mode of the cylinder N, which determines the amplitude and phase distribution of the oscillatory displacement distribution on the cylinder surface, in turn has an impact on the FDC.

2.5 Summary

In this chapter, an approximate analytical solution for the EM scattering from by an oscillating electrically small sphere has been derived. The derived solution indicates that the scattered EM signal has a discrete spectrum. The sidebands i.e., the Doppler components in the spectrum, are separated by integer multiples of the oscillating frequency of the sphere. With a small argument approximation, it was recognised that all Doppler components but the FDC can be omitted from the analysis. The directivity of the FDC in the scattered EM signal indicates that the strongest Doppler effect will be observed at the backward scattering position.

The derived solution has a series of limitations. It is only applicable to an isolated dielectric sphere that is electrically small, of small dielectric contrast and oscillating as rigid body without boundary deformation.

A SBC-FEM model is used for the first time. In order to validate the proposed model, it is used to investigate the bi-static scattering by dielectric cylinders that were mechanically vibrating in different resonance modes and with varying electrical properties. The results were found to be in excellent agreement with corresponding analytical solutions. The FEM-SBC model will be employed for more complex 3D problems which are relevant to medical applications and for which no analytical models exist.

Chapter 3 An EMA model for medical imaging in 3D

3.1 Introduction

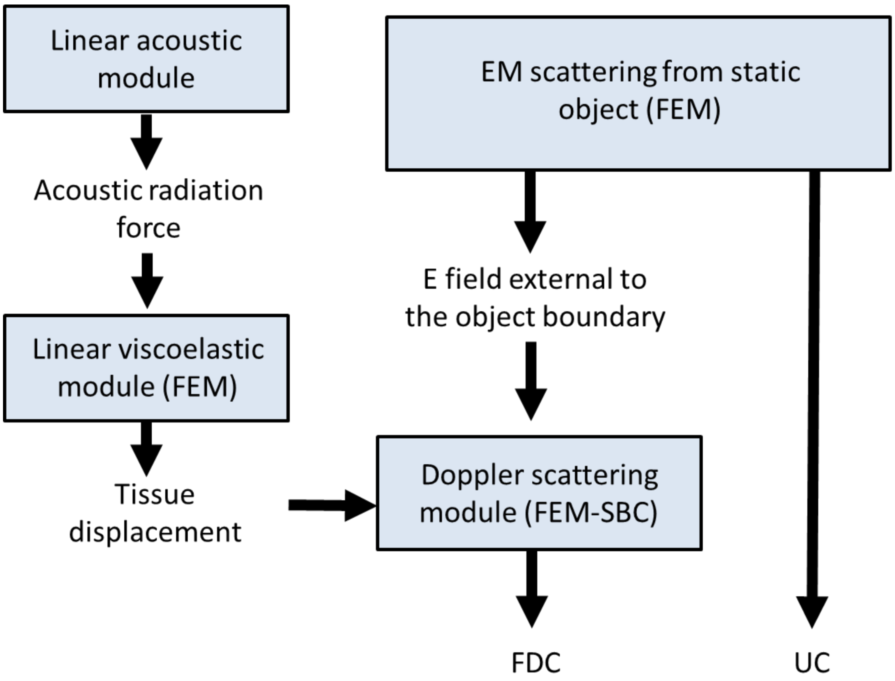

Figure 3.1 The simulation process of the proposed EMA model for medical imaging. The linear acoustic model considers the ultrasound propagation in soft tissue. The linear viscoelastic model considers the tissue dynamics under the ARF stimulation. The EM scattering from static object model and Doppler scattering model consider the regular and Doppler scattering from an oscillating object.

In this chapter, a complete EMA model for medical imaging is developed for simulations in 3D space. Figure 3.1 shows the schematic of the simulation process of the proposed EMA model. The process is as follows: 1) an analytical linear acoustic model (Section 3.2) is employed to calculate the acoustic pressure and acoustic radiation force (ARF); 2) The resultant ARF is input into a linear viscoelastic model (Section 3.3) based on a Finite Element Model (FEM). With this model, the response of the soft tissue is estimated numerically; 3) The scattering of the electromagnetic (EM) waves from a stationary scatterer (Section 3.3) is simulated and the UC in the spectrum of the scattered EM wave is determined; 4) The desired FDC is calculated using a Doppler scattering model (Section 3.4) based on the FEM-SBC.

3.2 The linear acoustic model

The EMA system employs a concave spherical ultrasound transducer operating in the MHz frequency range. The radius of the spherical transducer is usually large relative to the ultrasound wavelength and the depth of the concave surface. A numerical model based on the summation of Bessel function terms [72] is chosen to calculate the acoustic field excited by such a transducer as part of the EMA imaging model. For the purpose of validation, the pressure profiles along the axis of symmetry of the deployed transducer and in the lateral direction at the focal plane were measured and compared to the analytical linear acoustic model.

Figure 3.2 shows the coordinates and relevant parameters used for the analysis of the ultrasound transducer. Here r_0 is the radius of curvature, a is the radius of the active transducer element, B is the observation point, r is the distance from point source to the observation point, and θ is the polar angle of the observation point.

For a time harmonic excitation with angular frequency ω_{us}, the radiated pressure field of the above described ultrasound transducer is estimated analytically by [72],

$$
\begin{aligned}
p(r,\theta) &= \frac{jp_0 e^{-jk_{us}r}}{1 - r\cos\theta / r_0} I(Y,Z) \\
I(Y,Z) &= e^{-jY/2}\,\frac{Y}{Z}\left[u_1'(Y,Z) + ju_2'(Y,Z)\right] \\
u_1'(Y,Z) &= \sum_{n=0}^{\infty} (-1)^n \left(\frac{Y}{Z}\right)^{2n} J_{2n+1}(Z) \\
u_2'(Y,Z) &= \sum_{n=0}^{\infty} (-1)^n \left(\frac{Y}{Z}\right)^{2n+1} J_{2n+2}(Z) \\
Y &= \left(\frac{k_{us}\, a^2}{r}\right)\left[1 - \left(\frac{r}{r_0}\right)\cos\theta\right] \\
Z &= k_{us} a \sin\theta
\end{aligned}
\tag{3.1}
$$

where $p_0 = \rho_0 c_0 u_0$ is an effective source pressure on the transducer surface, u_0 is the surface velocity, ρ_0 is the material density, c_0 is the speed of sound, and k_{us} is the ultrasound wavenumber.

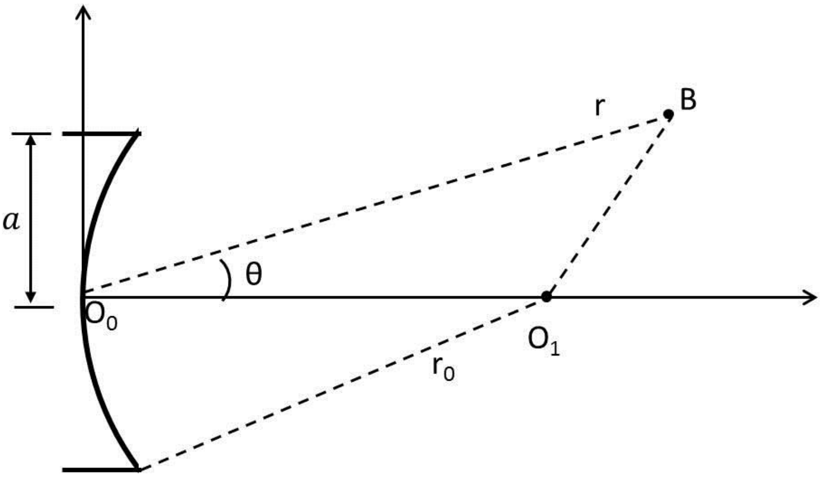

Figure 3.2 The geometry of a concave spherical ultrasound transducer

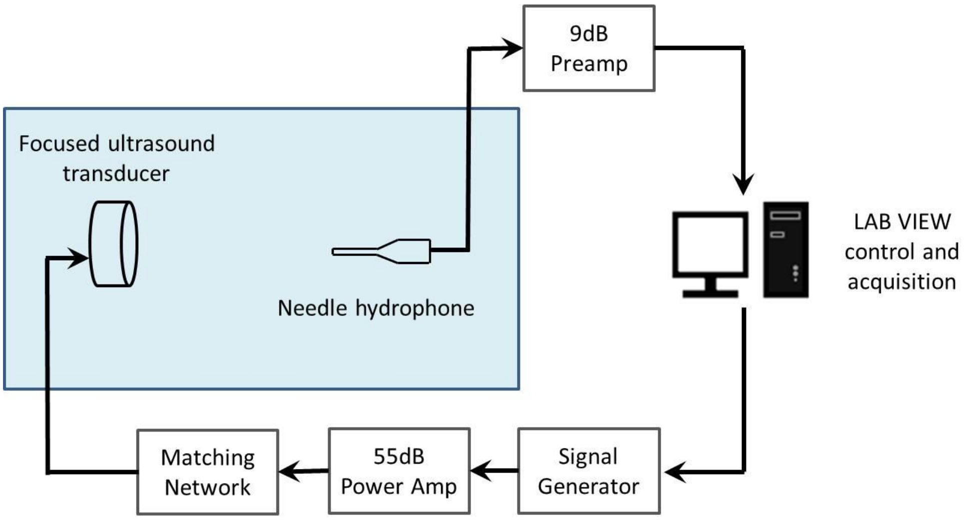

Figure 3.3 Schematic of the measurement system for the ultrasound pressure profile. The measurement was realised by a computer controlled acquisition system. The step size of the measurement was 1mm in the axial direction and 0.1 mm in the lateral direction.

Experimental measurements:

The measurement of the pressure profile radiated by the focused transducer (Harisonic I8-0516-P, f_{us} = 5 *MHz*, focal distance = 89 *mm*, a = 12.7 *mm*) was conducted with a hydrophone (HMP0075 1321, Precision Acoustics, diameter = 200 *μm*) inside a water tank. The measurement system is shown in Figure 3.3. The driving signal was 25 cycles of sinusoidal signal at 5 *MHz* of 10 *mV* peak-to-peak amplitude produced by a signal generator (33580 Agilent Technology) and amplified by a 55 dB radio frequency power amplifier (E&I A300).

Results and discussion:

The listed focal distance is the location of highest pressure and not the radius of curvature. The r_0 and a of the ultrasound transducer substituted into Equation 3.1 were varied to search for the best match between the linear acoustic model prediction and the experimental measurements. The best match was found when r_0 = 94 *mm* and a = 12.7 *mm*. The lateral and axial pressure profiles obtained by the two methods are compared in Figure 3.4. Excellent agreement between the linear acoustic model prediction and experimental measurements was observed in both directions especially within the main lobe. The standard deviation of the linear acoustic model prediction from the experimental measurement was 3.5% of its peak pressure. It is concluded that the linear acoustic model based on the method in [72] can provide adequate accuracy for the EMA modelling, and therefore will be used in the subsequent work.

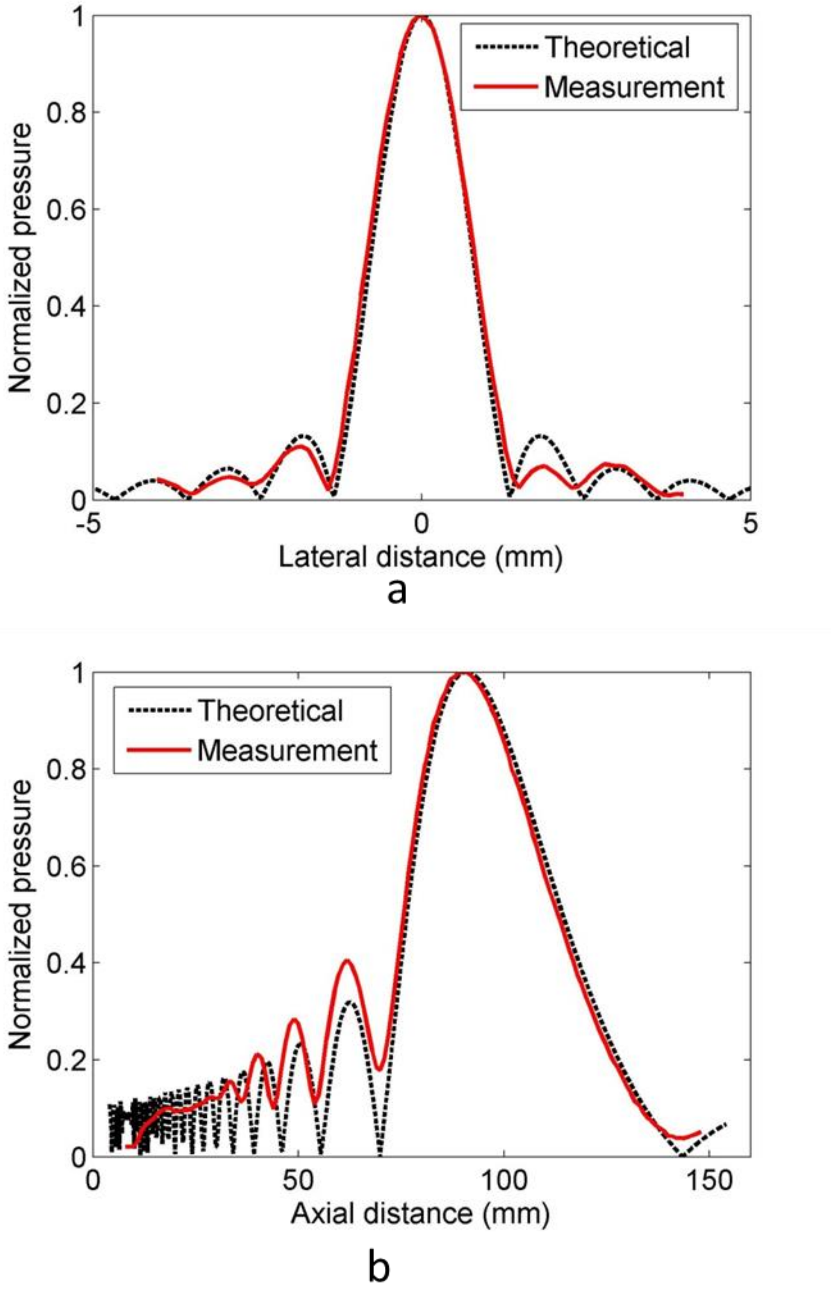

Figure 3.4 The comparison of the linear acoustic model predicted and experimentally measured pressure field (a) in the lateral direction at the focal length and (b) in the axial direction f_{us} *= 5 MHz.*

The ARF in the biomedical applications related to accessing viscoelastic properties of the biological tissue is generated by the change in the energy density of the propagating wave [73] due to 1) acoustic absorption by the medium and 2) the effects of scattering which alters the acoustic path. The same phenomenon is sometimes described as the transfer of momentum from the acoustic wave to the medium it propagates in by absorption and scattering [74] [22]. Assuming a plane acoustic wave, the ARF can be expressed as the following equation:

$$F = \frac{2\alpha I}{c_0} \tag{3.2}$$

where F [N/m^3] is the acoustic radiation force per unit volume, α [m^{-1}] the attenuation coefficient, and c_0 [ms^{-1}] the speed of sound. I[Wm^{-2}] is the average temporal ultrasound intensity for a locally progressive plane wave, and is calculated by [75] [76] [22]

$$I = \frac{1}{T}\int_0^T \frac{p^2(t)}{\rho_0 c_0}\,dt \tag{3.3}$$

where $p(t)$ is the pressure, and T is the ultrasound period. It is noted that for biomedical ultrasound the maximum allowable I is limited by certain safety limits [77]. EMA imaging has various potential applications, e.g. the imaging of breast tumours and the monitoring of High Intensity Focused Ultrasound (HIFU) surgery. The safety issues associated with the tumour detection is discussed in Section 4.2. For the real time monitoring of HIFU using EMA imaging, the intensity of the acoustic beam is determined by the therapeutic effect that one aims to achieve rather than the EMA imaging. Therefore it is not further discussed in this thesis.

The concave focused ultrasound transducers employed in the EMA produce a spatially localized ARF. The spatial distribution of the ARF generated by the transducer is illustrated in Figure 3.5. In order to induce an oscillatory motion of the target tissue, the acoustic radiation force is amplitude-modulated to create a harmonically oscillating force at ω_{arf} as shown in Figure 3.6. This can be done by multiplying $p(t) = p_0 \sin(\omega_{us})$ by a sinusoidal signal $\sin(\frac{\omega_{arf}t}{2})$ where ω_{arf} denotes the angular frequency of the resulting oscillating ARF. Substituting $p(t) = p_0 \sin(\omega_{us}t)\sin(\omega_{arf}t/2)$ into Equation 3.3 yields the pressure modulation is described by,

$$I(t) = \frac{1}{T}\int_0^T \frac{p_0^2}{\rho_0 c_0} \sin^2(\omega_{us}) \sin^2\left(\frac{\omega_{arf}}{2}\right) dt \tag{3.4}$$

For $\omega_{us} \gg \omega_{arf}$,$\sin^2(\omega_{us}t)$ is approximately constant for at the time scale of ω_{arf}, which leads to

$$I(t) = \frac{1}{2T}\int_0^T \frac{p_0^2}{\rho_0 c_0} \sin^2(\omega_{us})\, dt = I_0(1 - \cos(\omega_{arf}t))/2 \tag{3.5}$$

The spatial-peak, temporal peak intensity I_{sptp} is the highest spatial and instantaneous intensity as shown in Figure 3.6d. The spatial-peak, pulsed-average intensity I_{sppa} describes the intensity of the transmitted pulse waveform. It is the spatial peak intensity averaged over the duration of the pulse (Figure 3.6d). The spatial-peak, temporal average intensity I_{spta} evaluates the ability of the ultrasound waveform to heat tissue. Assuming a pulse of duration t is repeated at every T, $I_{spta} = I_{sppa} \times \frac{t}{T}$. Note that Figure 3.6d shows the case for $t = T$, therefore $I_{spta} = I_{sppa}$. The modulated ARF is input into the linear viscoelastic model based on FEM in Section 3.3 to simulate the oscillatory response of soft tissue.

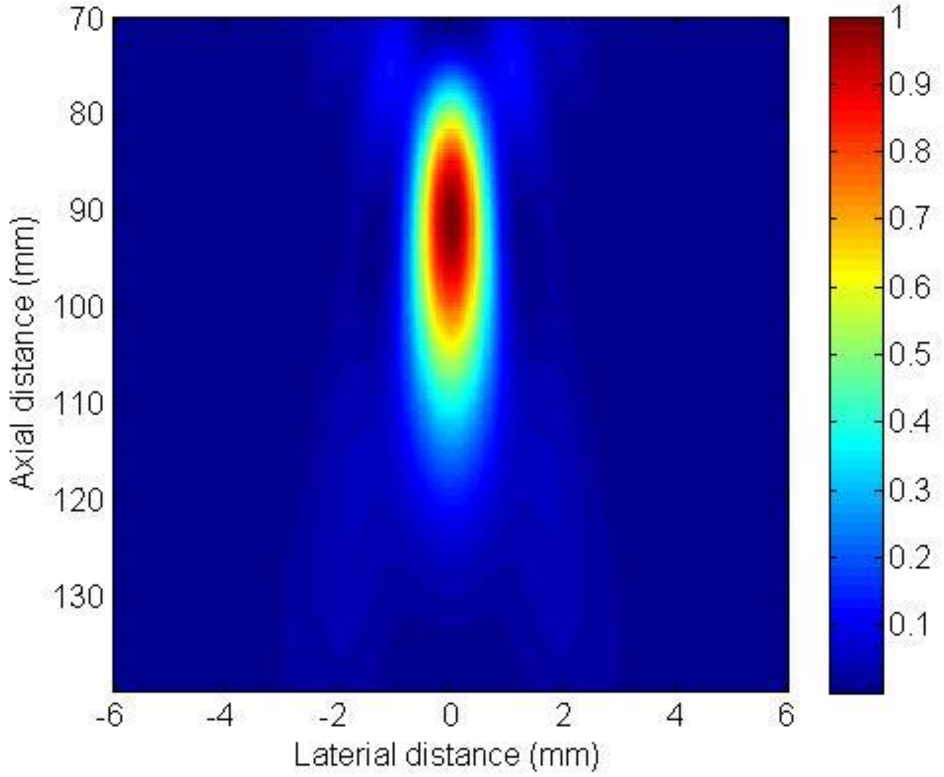

Figure 3.5 The simulated spatial distribution of the normalized acoustic radiation force produced by the 5 MHz ultrasound transducers with $r_0 = 94\ mm$ *and a = 12.7 mm.*

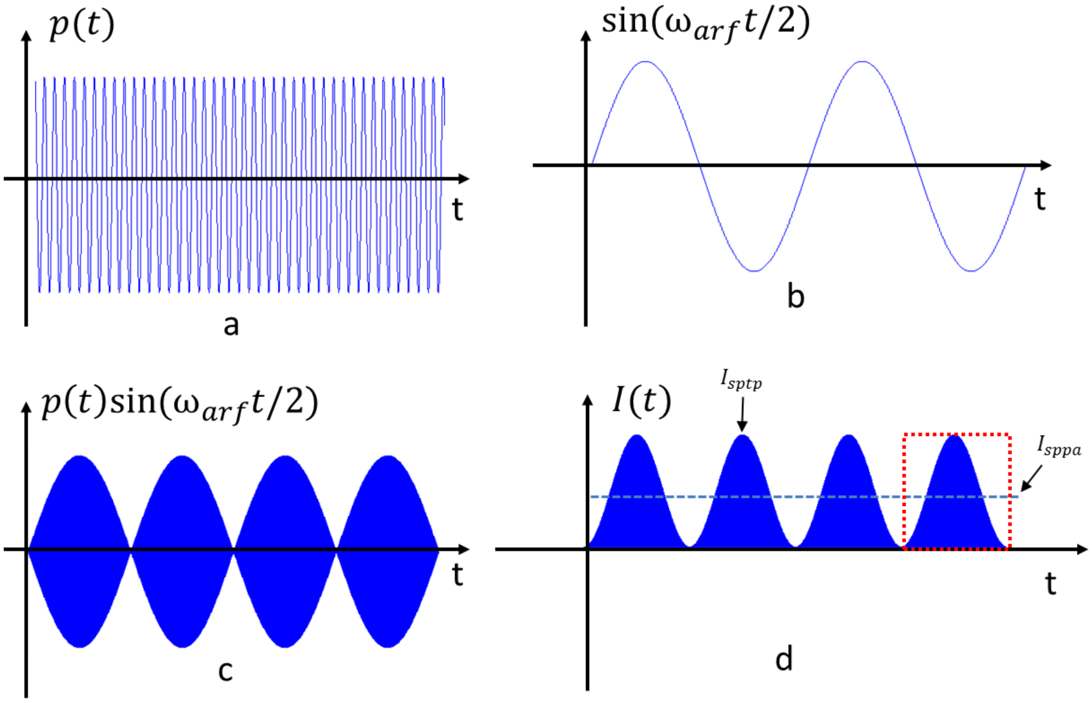

Figure 3.6 The acoustic pressure produced by a 5MHz transducer (a) is amplitude–modulated by a sinusoidal signal at $\omega_{arf}/2$ *(b), resulting modulated time varying pressure (c) and ultrasound intensity (d) at an angular frequency* ω_{arf}*. The resultant ARF is related to I(t) by equation 3.2.*

3.3 A linear viscoelastic model

Theoretical background:

Soft tissues can be treated as linear viscoelastic, isotropic solids to a first order approximation [74]. In Cartesian coordinates, the balance of linear momentum can be expressed as

$$\sigma_{ij,j} + \rho_0 b_i = \rho_0 f_i \qquad (3.6)$$

where $\sigma_{ij,j}$ is the directional derivative of the stress tensor, b_i is the external steady-state acceleration such as gravity and f_i is an externally applied radiation force. The following equation relates the stress tensor to the displacement

$$\sigma_{ij} = \bar{\lambda}\delta_{ii}u_{i,i} + \bar{\mu}(u_{i,j} + u_{j,i}) \qquad (3.7)$$

where $\bar{\lambda}$ and $\bar{\mu}$ are the complex first and second Lamé constants for the material which are usually empirically determined. The real parts of the Lamé constants correspond to the elastic or storage moduli and the imaginary part to the loss modulus. u_i is the particle displacement, and δ_{ij} equals 1 when i=j, otherwise equals 0. Equation 3.6 can be separated into elastostatic and elastodynamic components. The elastostatic component is neglected in the analysis of elastic waves hence $b_i = 0$ and $f_i = \ddot{u}_i$. Equations 3.6 and 3.7 can be expressed in the vector form as [78] [22]

$$(\bar{\lambda} + \bar{\mu})\nabla(\nabla \cdot \vec{u}) + \mu\nabla^2\vec{u} = \rho_0\ddot{\vec{u}} \qquad (3.8)$$

where ¨ denotes the second time derivative. The displacement $\vec{u}$ can be constructed from two potentials: a scalar ψ associated with dilatational deformation in the direction of ultrasound wave propagation, which is a longitudinal wave, and a vector $\vec{W}$ associated with isochoric deformation, that is a shear wave,

$$\vec{u} = \nabla\psi + \nabla \times \vec{W} \tag{3.9}$$

Substituting Equation 3.9 into Equation 3.8 yields

$$\nabla\left[(\bar{\lambda} + 2\bar{\mu})\nabla^2\psi - \rho_0 \frac{\partial^2\psi}{\partial t^2}\right] + \nabla \times \left[\bar{\mu}\nabla^2\vec{W} - \rho_0 \frac{\partial^2\vec{W}}{\partial t^2}\right] = 0 \tag{3.10}$$

which for an infinite homogenous medium has two separable terms taking the form of wave equations. Separating these two equations and considering propagation in the y direction for the longitudinal wave

$$\frac{\partial^2\psi}{\partial y^2} - \frac{1}{c_l^2}\frac{\partial^2\psi}{\partial t^2} = 0 \tag{3.11}$$

where

$$c_l = \sqrt{\frac{\bar{\lambda} + 2\bar{\mu}}{\rho_0}} \tag{3.12}$$

and the propagation of the shear wave in the direction r that is perpendicular to y,

$$\frac{\partial^2\vec{W}}{\partial r^2} - \frac{1}{c_s^2}\frac{\partial^2\vec{W}}{\partial t^2} = 0 \tag{3.13}$$

where

$$c_s = \sqrt{\frac{\bar{\mu}}{\rho_0}} \tag{3.14}$$

A solution to Equation 3.11 takes the form of

$$\psi = Ae^{-\alpha_l y + j(\omega t - k_l y)}\hat{y} \tag{3.15}$$

where α_l and k_l are the attenuation coefficient and wave number (ω_{arf}/c_l) for longitudinal wave respectively, and A the original wave amplitude. At ultrasound frequencies (> MHz), the longitudinal attenuation α_l gives rise to the ARF. However the attenuation coefficient of biological tissue is strongly frequency dependent. At frequencies as low as ω_{arf}, the attenuation of longitudinal wave is negligible and the material can be adequately modelled as purely elastic [74]. Similarly, a solution to Equation 3.13 is given by

$$W = Be^{-\alpha_s r + j(\omega t - k_s r)}\hat{r} \tag{3.16}$$

where α_s is the attenuation coefficient and $k_{s=}\ \omega_{arf}/c_s$ the wave number for the shear wave, and B the original wave amplitude. For the analysis of shear wave propagation, a Voigt model is chosen to describe the shear viscoelastic behaviour of tissues. It has been shown that this model describes the viscoelasticity of tissues well for low frequency ARF excitation f_{arf} (0-500 Hz) [25] [79]. In the Voigt model, the second Lame's constant can be expressed as:

$$\overline{\mu(t)} = \mu + \eta_s(\partial/\partial t) \xrightarrow{Fourier} \overline{\mu(\omega)} = \mu + j\omega\eta_s \tag{3.17}$$

where μ is the shear modulus and η_s is the shear viscosity. The resulting expressions for shear attenuation and shear wave speed at ω_{arf} are given by [80]:

$$\alpha_s = -\omega_{arf}\left[imag\left(\sqrt{\frac{\rho_0}{\bar{\mu}(\omega_{arf})}}\right)\right] \tag{3.18}$$

and

$$c_s = \left[Real\left(\sqrt{\frac{\rho_0}{\bar{\mu}(\omega_{arf})}}\right)\right]^{-1} \tag{3.19}$$

FEM model:

In the EMA imaging, solving the dynamic response of the soft tissue to ARF stimulation in a geometrically complicated medium is very challenging, and the problem therefore lends itself to a numerical solution. FEM have been used to evaluate the response of soft tissues in a number of studies and good agreement between simulations and experimental observations were reported [81] [82] [83] [74] . Therefore a FEM based linear viscoelastic model was used to evaluate the oscillatory displacement of the tissue as part of the EMA model.

The FEM was implemented using a commercial software package ('Structured Mechanics' of Comsol Multiphysics^{TM}, Comsol Inc., Burlington, MA, USA) from an axially symmetric geometry as shown in Figure 3.7. An axisymmetric background tissue was created with a radius of 4.5 *cm* and a height of 9 *cm*. The simulation was conducted in the time domain for 30 *ms* with a temporal step size of 0.1 *ms*. The radial extent of the background tissue ensured that the shear waves did not reach the cylindrical boundary within the simulation time. For the grid 1642 triangular mesh elements were generated with 18763 degrees of freedom.

For validation, the FEM solutions were computed for an infinite homogenous soft tissue under the stimulation of an ARF pulse, and the results were compared to analytical solutions based on free-space Green's functions.

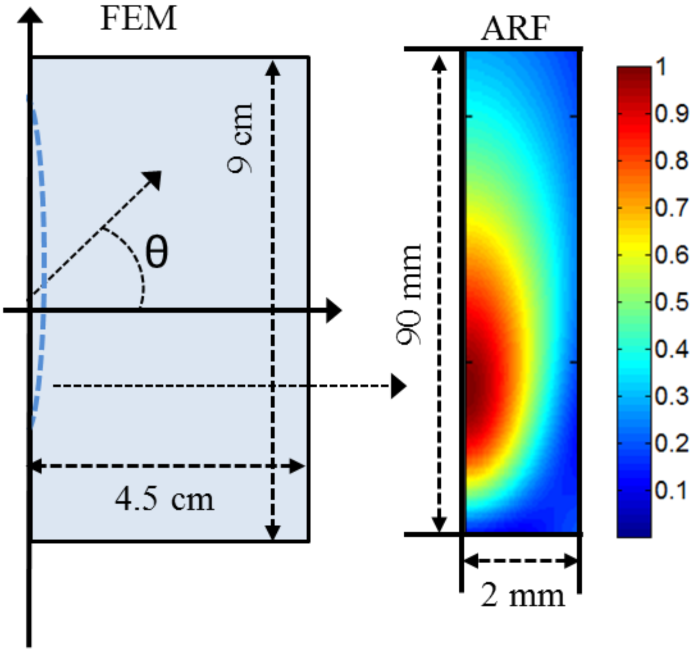

Figure 3.7 Illustration of the geometry of the linear viscoelatic model based on FEM: the axial symmetrical tissue with scatterer omitted from the illustration (left) and the spatial distribution of ARF (right). The colour bar show the normalised amplitude of ARF.

Green's function based solutions:

In the infinitely large homogeneous medium, transient solutions to the displacement induced by externally applied force based on the elastodynamic Green's function for linear elastic [75] and linear viscoelastic [84] materials were developed separately. In the Cartesian coordinates described by (x_1, x_2, x_3), the transient response of linear elastic tissue at location $\boldsymbol{x} = (x_1, x_2, x_3)$ to a spatial and temporal impulse excitation at origin is given by [75] [85] [86],

$$\begin{aligned} g_{ij}(\boldsymbol{x}, t) = &\frac{\left(3\gamma_i\gamma_j - \delta_{ij}\right)}{4\pi\rho}\frac{1}{r^3}\int_{\frac{r}{c_l}}^{\frac{r}{c_s}} \tau\delta(t-\tau)d\tau \\ &+ \frac{\gamma_i\gamma_j}{4\pi\rho}\frac{1}{r}\frac{\delta(t - r/c_l)}{c_l^2} \\ &+ \frac{(\delta_{ij} - \gamma_i\gamma_j)}{4\pi\rho}\frac{1}{r}\frac{\delta(t - r/c_s)}{c_s^2} \end{aligned} \tag{3.20}$$

where $i = 1,2,3$ represents the direction of the applied ARF in Cartesian coordinates, $j = 1,2,3$ the direction of the tissue displacement, $\delta(t)$ the Dirac delta function, and $r = |\boldsymbol{x}| = \sqrt{x_1^2 + x_2^2 + x_3^2}$. $\gamma_i = x_i/r$ is the direction cosine for the vector x_i, c_l and c_s the longitude and shear wave speed respectively. The applied ARF can be treated as a superposition of individual point sources and the induced displacement in the direction j can be computed by the spatio-temporal convolution of the applied force f_i and the spatial-temporal impulse response,

$$u_j(\boldsymbol{x}, t) = f_i(\boldsymbol{x}, t) \otimes g_{ij}(\boldsymbol{x}, t) \tag{3.21}$$

The transient response in a linear viscoelastic medium can be determined with the assumption that the shear wave speed is frequency independent. It is given by the sum of a longitudinal term g_{ij}^{l}, and shear term g_{ij}^{s} and a coupling term g_{ij}^{ls},

$$g_{ij}(\boldsymbol{x}, t) = g_{ij}^{l}(\vec{r}, t) + g_{ij}^{s}(\vec{r}, t) + g_{ij}^{ls}(\vec{r}, t) \tag{3.22}$$

where

$$g_{ij}^{l}(\vec{r},t) = \frac{1}{4\pi\rho c_l}\,\frac{1}{\sqrt{2\pi\nu_l t}}\gamma_i\gamma_j\,\frac{1}{r}\,e^{-\frac{\left(t-\frac{r}{C_l}\right)^2 c_l^2}{2\nu_l t}} \tag{3.23}$$

$$g_{ij}^{s}(\vec{r},t) = \frac{1}{4\pi\rho c_s}\,\frac{1}{\sqrt{2\pi\nu_s t}}\gamma_i\gamma_j\,\frac{1}{r}\,e^{-\frac{\left(t-\frac{r}{C_s}\right)^2 c_s^2}{2\nu_s t}} \tag{3.24}$$

$$\begin{aligned} g_{ij}^{ls}(\vec{r},t) &= \frac{1}{4\pi\rho}\left(3\gamma_i\gamma_j-\delta_{ij}\right)\frac{1}{r^3} \\ &\left[c_l\frac{1}{\sqrt{2\pi\nu_l t}}\int_0^{r/C_l}\tau e^{-\frac{\left(t-\frac{r}{C_l}\right)^2 c_p^2}{2\nu_l t}}\,d\tau \right. \\ &\left. -\,c_s\frac{1}{\sqrt{2\pi\nu_s t}}\int_0^{r/C_s}\tau e^{-\frac{\left(t-\frac{r}{C_s}\right)^2 c_s^2}{2\nu_s t}}\,d\tau\right] \end{aligned} \tag{3.25}$$

where $\nu_l = (\eta_p + 2\eta_s)/\rho_0$ and $\nu_s = \eta_s/\rho_0$ are the kinematic bulk and shear viscosity, η_p and η_s are the bulk viscosity and shear viscosity.

Results and Discussion:

In both the FEM and analytical expression, the transient response of the tissue to a rectangular pulse ARF with a spatial characteristic described in Figure 3.5 were simulated. The duration of the ARF pulse was 3.125 *ms* with an acoustic intensity I_{sptp} = 1000 W/m^2. With the arguments presented in [74] [87], the Poisson's ratio v = 0.499 and the ultrasound attenuation coefficient 0.7 dB*/cm/MHz* were employed. The Young's modulus of the soft tissue was 3 *kPa*, the material density was 1000 kg/m^3, and the shear viscosity was either 0 $Pa \cdot s$ or 0.2 $Pa \cdot s$. The temporal profiles of the displacements were recorded at 1 *cm* (P1) and 2 *cm* (P2) lateral to the focal point of the ARF and are shown in Figure 3.8. Note that both of the observation points were located outside the ARF field to avoid singularities created in Equation 3.20 to Equation 3.24 when $r \rightarrow 0$.

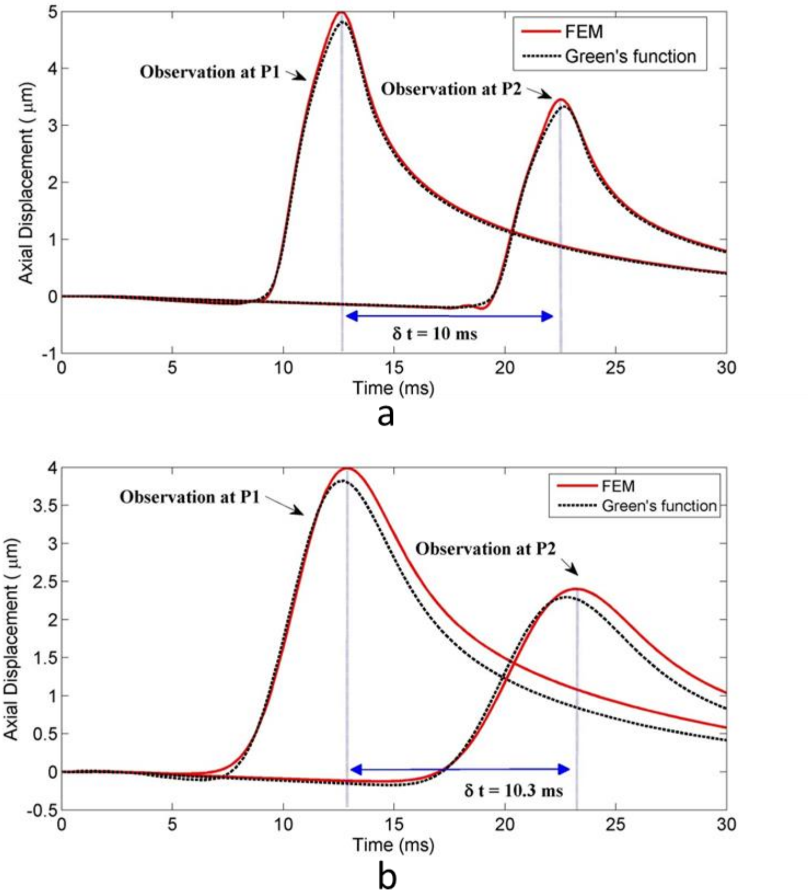

Figure 3.8 The dynamic response of the soft tissue to an ARF pulse: FEM simulated solution at 1cm (P1) and 2 cm(P2) away from the point of stimulation compared to Green's function based solution: (a) $\eta_s = 0\ Pa \cdot s$ *and (b)* $\eta_s = 0.2\ Pa \cdot s$.

It is shown in Figure 3.8 that the FEM solutions are in good agreement with the Green's function based solutions. In both inviscid (Figure 3.8a) and viscous (Figure 3.8b) tissue, the Green's function based solutions underestimated the peak displacements by approximately 4%. This was due to that the spatial grid used in the Green's function based solution was not fine enough to fully resolve the ARF field. Doubling the resolution of the spatial grids in each direction has led to smaller discrepancy between the FEM solution and the analytical solution (3%). However, it has increased the simulation time by 8 times. In addition, slight discrepancies between the arrival time of the peak displacements at P1 and P2 in Figure 3.8b was observed which was larger than seen in Figure 3.8a. This was likely because the Green's function employs a fixed shear wave speed for all frequencies. With a rectangular pulse ARF excitation, the induced shear wave contains components at multiple frequencies which would travel at different speed in the FEM when viscosity was present. In Figure 3.8a, viscosity was not considered, and dispersion would not be an issue, however in Figure 3.8b, there would be dispersion present in the FEM.

From the above investigation it was concluded that the proposed linear viscoelastic model based on FEM is capable of producing accurate prediction of the soft tissue response to time-varying ARF and therefore this model was incorporated into the EMA model in the rest of the work.

3.4 EM scattering from a stationary object

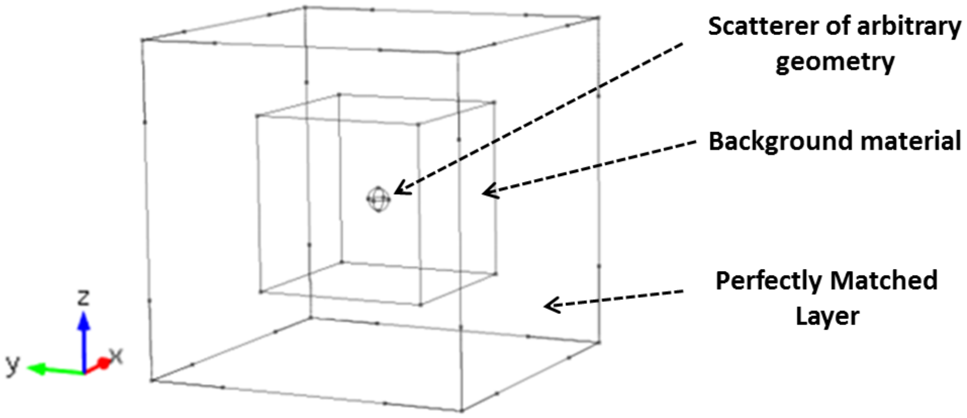

Figure 3.9 The geometry of the EM scattering model by stationary object implemented in Comsol Multiphysics

The simulation framework for the electromagnetic scattering in 3D space followed the two-simulation approach described in Section 2.4. The first step is the simulation of the EM scattering as if the scatterer was stationary.

The FEM model for EM scattering by a stationary object was implemented using 'Comsol Multiphysics^{TM}'. Figure 3.9 illustrates the problem: a scatterer is placed at the origin of the Cartesian coordinates. Note that a spherical scatterer in Figure 3.9 is for the purpose of illustration and the sphere can be replaced by a scatterer of arbitrary geometry. The background medium was modelled by a cube with edge length of 20 *cm*. A perfectly matched layer (PML) of 7 *cm* thickness was added immediately outside the background material with a maximum reflection < -90 dB. This removed the reflection of outgoing EM waves by the background medium boundaries. Free tetrahedral meshes were applied to the inclusion and background tissue and prism meshes were applied to the PML. The total number of elements generated was 92958 with 638244 degrees of freedom solved for. The incident wave was set to be a 434 *MHz* plane wave travelling in +y direction with its E field polarized in z direction. The EM-FEM allowed the field quantities to be recorded at the surface of the scatterer and any other positions at which EM receivers were placed.

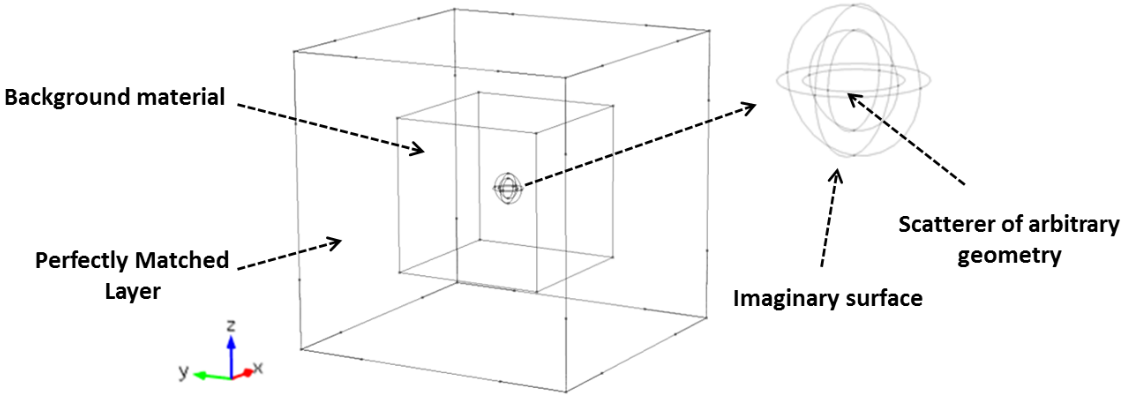

Figure 3.10 The geometry of surface equivalent model. An imaginary closed surface is created just outside the scatterer

However, a particular problem arises when this approach is used in the investigation of HIFU therapy monitoring presented in Chapter 5. The scatterer is a thermal lesion which is olive shaped with maximum length smaller than 10 *mm* in the longitudinal direction, and the electrical contrast between the HIFU lesion and background medium is small (Figure 5.3). The HIFU lesion is therefore a weak scatterer and the amplitude of the scattered EM signal decreases rapidly as the EM receiver moves away from the scatterer. Once the scattered EM signal falls below the numerical noise floor of the FEM it is not detectable in the simulation. This was found to occur at a distance approximately 3 *cm* away from HIFU lesions. The numerical noise is associated the incident EM wave. To solve this problem, one solution is to exploit the surface equivalence theorem [88] to remove the incident EM wave. The surface equivalence theorem states that the incident EM wave and the actual scatterer i.e., the thermal lesion can be replaced by an equivalent source. The steps are summarized as following,

1) A virtual closed surface is created just outside the thermal lesion as shown in Figure 3.10. On the virtual surface, the H field external and tangential to the imaginary surface is recorded.
2) The equivalent current can be calculated by,

$$J_s = \hat{n} \times H_1 \tag{3.26}$$

   where subscript 1 denote the field external to the virtual surface.
3) The incident EM wave is disabled in the FEM. The above calculated equivalent current is distributed at the virtual surface. The volume enclosed by the virtual surface is set to be perfect electric conductor. This model is referred to as a surface equivalence model in the rest of the thesis.
4) The surface equivalence model is implemented and the E field at desired locations is calculated.

Table 3.1 Summary of the electrical properties of the scatterer and background medium at 434 MHz

Parameter	Background medium	Inclusion material
ε	18	57.5
μ	1	1
σ	0 *S/m*	0 *S/m*

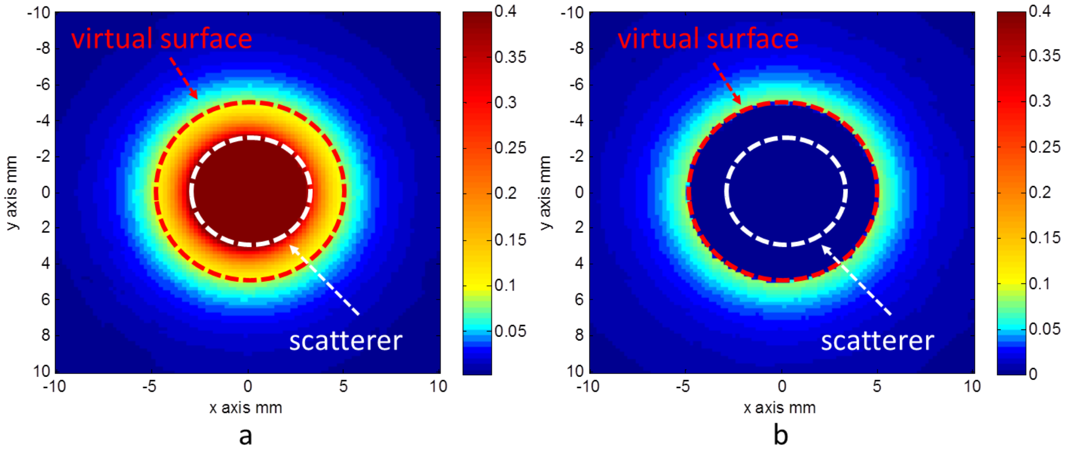

Figure 3.11 Comparison of the EM scattering model and the surface equivalence model. (a) the scattered E field in y-x plane in the EM scattering model for a static object and (b) the radiated E field form equivalent current in the surface equivalence model. The virtual surface is marked out by the red circle and the boundary of the scatterer is marked out by white circle. Colour bar unit V/m

Validation:

For the purpose of validation, a plane EM wave at 434 *MHz* polarized in z direction was assumed to travel in +y direction and the scattered E field by a spherical scatterer of $r = 3\ mm$ was simulated. The virtual surface was chosen to be a sphere with a radius of 5 mm. The relevant parameters are summarized in Table 3.1. The received E field in the y-x plane near the scatterer simulated by the EM scattering model for static object and the surface equivalence model are illustrated in Figure 3.11.

In Figure 3.11a, the E field is of its greatest within the spherical scatterer and decays rapidly when the EM receiver moves away from the scatterer. H field was recorded at the spherical virtual surface, converted to the surface current with Equation 3.26, and distributed onto the virtual surface in the surface equivalence model. The radiated E field by the surface current is shown in Figure 3.11b. The results show that the surface equivalence model produced E field equivalent to the direct scattering model outside the virtual surface. Note that the EM field within the virtual surface is zero in Figure 3.11b as Equation 3.12 implies the field inside the scatterer is 0. The directivity of the E field in y-x plane 89 mm away from the centre of the scatterer are compared in Figure 3.12. At further locations (89 mm in Figure 3.12) from the scatterer, the radiated field in the surface equivalence model was in excellent agreement (RMS error = 1%) with the scattered field in the EM scattering model.

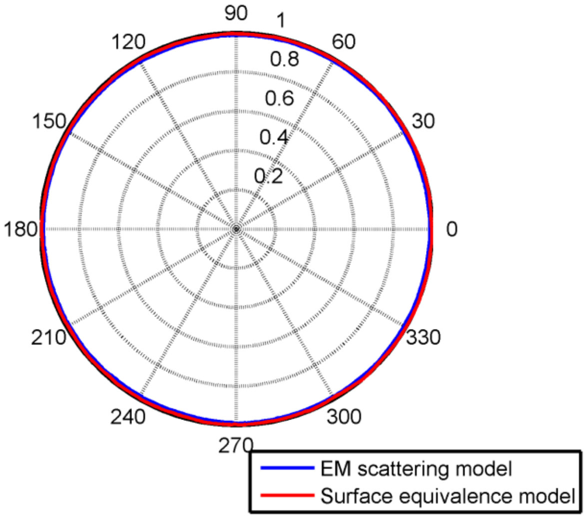

Figure 3.12 The comparison of the directivity of the EM scattering model and surface equivalence model 89 mm away from the centre of the scatterer in the y-x plane.

3.5 A FEM-SBC model in 3D space

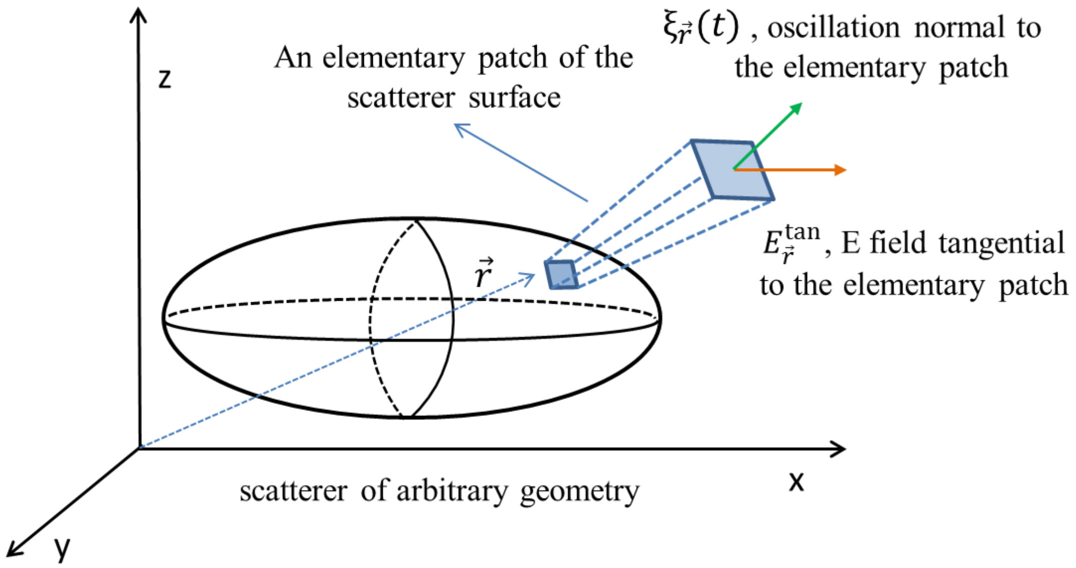

Figure 3.13 Illustration of a 3D scatterer with vibrating boundary. An elementary area at location indicated by vector $\vec{r}$ *is highlighted with its associated normal oscillation (green arrow) and tangential E field (orange arrow)*

The calculation of the FDC using a FEM-SBC model involves the EM field tangential to the surface of the scatterer and the oscillatory motion normal to the surface of the scatterer (Equation 2.26 and Equation 2.35). A scatterer with its boundary in motion is illustrated in 3D in Figure 3.13. An elementary area at the position $\vec{r}$ is highlighted in blue. Note that the change in the area of elementary patch is not considered in the investigation as the soft tissues are assumed to be nearly incompressible (Poisson's ratio is assumed to be 0.499, see Table 4.1). In the EMA imaging, the motion of the scatterer is induced by a localized harmonic ARF and has an angular frequency ω_{arf}. Therefore the oscillatory motion of an elementary area in the normal direction at location $\vec{r}$ can be described by,

$$\xi_{\vec{r}}(t) = \Gamma_{\vec{r}} e^{j\theta_{\vec{r}}} e^{j\omega_{arf} t} \hat{n}_{\vec{r}} \qquad (3.27)$$

or

$$\Xi_{\vec{r}}(\omega) = 2\pi \Gamma_{\vec{r}} e^{j\theta_{\vec{r}}} \delta(\omega - \omega_{arf}) \qquad (3.28)$$

where $\Gamma_{\vec{r}}$ and $\theta_{\vec{r}}$ are the amplitude and phase of the oscillatory motion respectively, ω_{arf} the oscillation frequency, and $\hat{n}_{\vec{r}}$ the unit vector normal to the elementary area at location $\vec{\boldsymbol{r}}$. Using similar principles as introduced in Section 2.4, the equivalent current in the FEM-SBC model distributed on the elementary area can be calculated from the tangential E field at the scatterer surface $E_{\vec{r}}^{tan}$ and the oscillation function,

$$J_{\vec{r}} = \hat{n}_{\vec{r}} \times \hat{n}_{\vec{r}} \times \left\{ -j(\varepsilon_2 - \varepsilon_1)\omega_{em} \Xi_{\vec{r}}(\omega_{arf}) E_{\vec{r}}^{tan} \right\} \qquad (3.29)$$

where ω_{em} is the frequency of the EM signal.

Table 3.2 Summary of the electrical properties of the scatterer and background material at 434 MHz. $\boldsymbol{\varepsilon}$ *is the relative permittivity,* $\boldsymbol{\mu}$ *the relative permeability and* $\boldsymbol{\sigma}$ *the electrical conductivity.*

Parameter	Background material	Inclusion material
ε	18	19
μ	1	1
σ	0 *S/m*	0 *S/m*

For the implementation of the FEM-SBC model, the same geometry of the static EM scattering model can be used with the incident EM wave removed. A 3 mm radius scatterer was assumed to oscillating in y direction harmonically as described in

Section 2.2 and illustrated in Figure 2.1. For the purpose of validation, the scattered field can be compared to the analytical solution derived in Chapter 2.2. The analytical solution had two assumptions 1) the scattered field was detected in the far field and 2) the scatterer had a small electric contrast relative to the background. In order to enable the comparison, the edge of the background medium in the FEM was increased to 32 *cm* which allowed the EM receiver to be placed sufficiently far away from the scatterer, and the electrical parameters listed in Table 3.2 were used to ensure that the electrical contrast was less than 6%. The equivalent current was calculated using Equation 3.29 and distributed at the surface of the scatterer, from which the FDC of the scattered EM field was calculated.

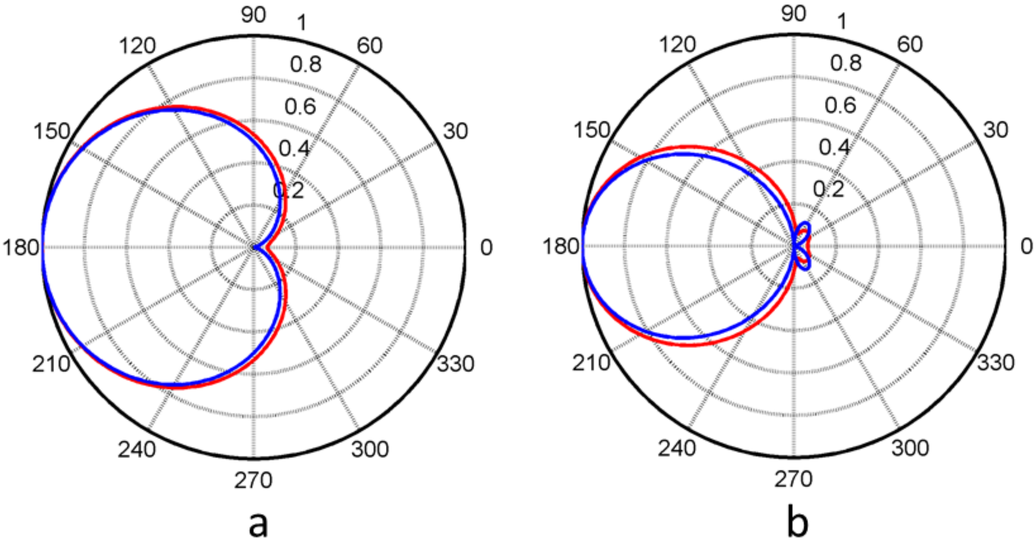

Figure 3.14 The FEM-SBC simulated FDC (red)received 150 mm away from the electrically small and oscillating sphere plotted as a function angle compared to analytical solution (blue)in(a) y-x plane, (b) plane y-z plane.

The FDC was recorded 150 *mm* away from the centre of the scatterer in both y-x plane and y-z plane and is shown in Figure 3.14. There was good agreement between the FEM solutions and analytical solutions. The strongest FDC was observed at the backward scattering position. The radius of the spherical scatterer was then varied from 0.5 *mm* to 10 *mm*. The resultant FDC at the backward scattering position ($\varphi = 0°$) were compared with analytical prediction in Figure 3.15. Again there was excellent agreement as the FEM capture the r^3 dependence of the amplitude which was consistent with Rayleigh scattering. Last, the relative permittivity of the scatterer material ε_{ic} was varied from 18.5 to 20. Figure 3.16 shows that the change in the FDC predicted by the FEM-SBC model as a function of dielectric property was consistent with the prediction by analytical prediction when the electrical contrast was small.

In conclusion, it is demonstrated in this section that the FEM-SBC model developed here is robust in estimating the Doppler shift in the EM signal scattered by a scatterer in oscillatory motion. The model was validated by use of analytical solutions for some simple cases. The FEM-SBC can be applied to scatterers of arbitrary geometry with no restrictions on the electrical contrast and size and can also simulate the EM signal close to the scatterer without the far field assumption in the analytical solution.

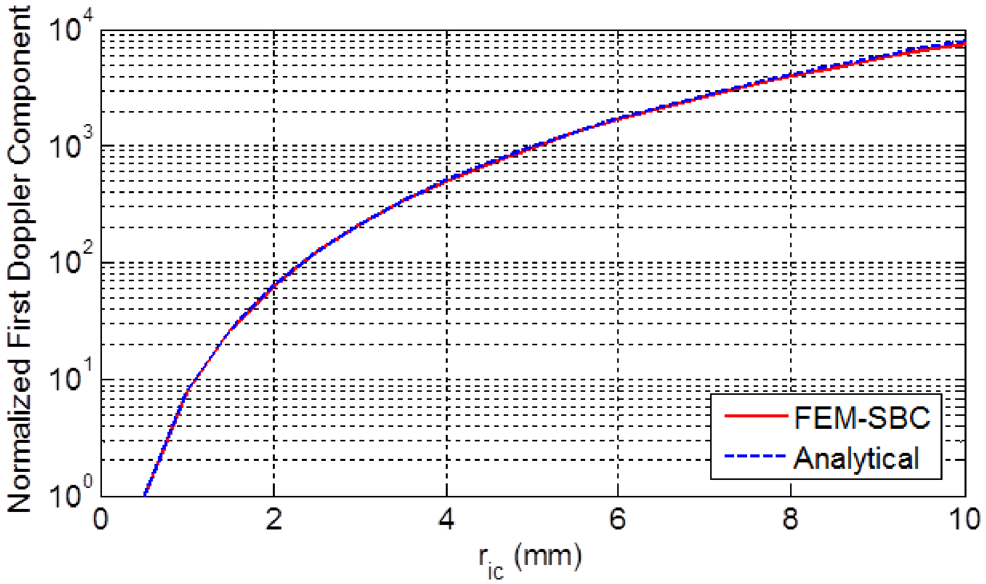

Figure 3.15 The FEM-SBC simulation compared (red) to analytical solution (blue) for oscillating sphere as a function of radius, for ε_{ic} = 19, σ_{ic} = 0 S/m and ε_{bg} = 18, σ_{bg} = 0 S/m

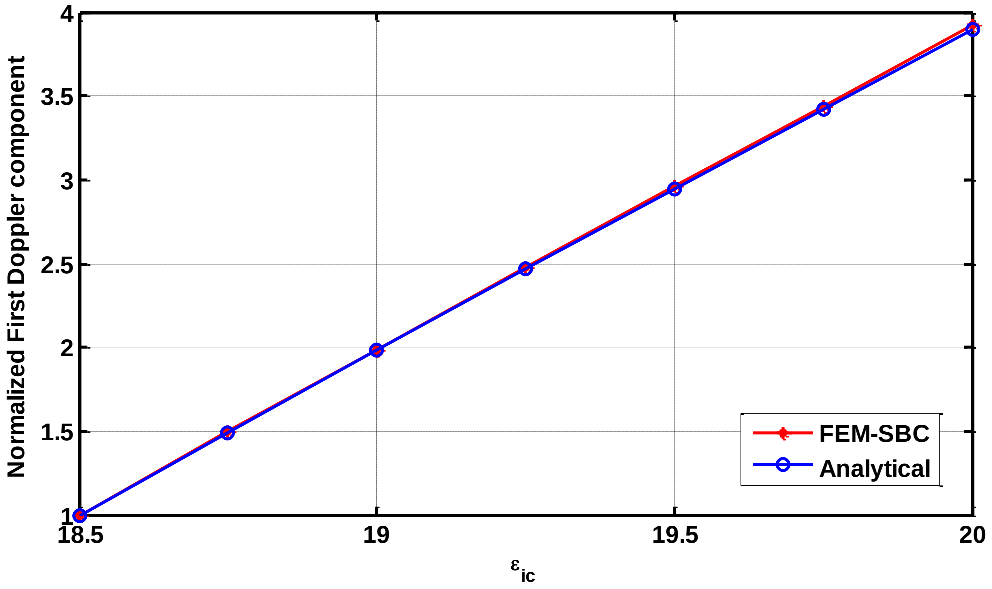

Figure 3.16 The FEM-SBC simulation (red) compared to analytical solution (blue) for oscillating sphere as a function of ε_{ic}, for ε_{ic} = 18.5-20, σ_{ic} = 0 S/m and ε_{bg} = 18, σ_{bg} = 0 S/m

3.6 Summary

In this chapter, a complete numerical model to simulate the key physical processes involved in the EMA imaging in 3D space has been developed. The EMA model is composed of 4 models:

1. A linear acoustic model estimates the ARF generated by an acoustic source ;
2. A linear viscoelastic model computes the oscillatory response of the tissue under the stimulation of the amplitude-modulated ARF;
3. A EM scattering model for stationary object to estimate the UC in the scattered EM signal;
4. A FEM-SBC model to estimate the FDC in the scattered EM signal.

The four models employ a combination of analytical and numerical methods. They were validated using experimental and analytical results during the development. This model will be used to investigate the feasibility of applying the EMA imaging to the diagnosis of various diseases, as well as other applications. In the following chapters, two potential applications of the EMA imaging are investigated: 1) the detection of breast tumours and 2) the real-time monitoring of the High Intensity Focused Ultrasound (HIFU) therapy.

Chapter 4 EMA imaging of breast tumours

4.1 Introduction

In this chapter, the potential of the EMA imaging in breast tumour detection is investigated. The EMA model developed in Chapter 3 is used to evaluate the dependence of the EMA signal on different parameters that are relevant to breast tumours including mechanical properties, electrical properties and tumour size. The chapter is organised as follows: first, the potential clinical safety issues of EMA imaging are discussed. Second, a case study is presented to demonstrate the complete simulation process for a tumour in the breast. A parametric study of the effect of variation of the mechanical and electrical properties on the scattered EM signal is presented. Finally, the influence of the size of the tumour on the scattered EM signal is considered.

4.2 Safety of EMA

In order for the EMA imaging to be clinically viable it is necessary to show that an EMA system does not produce any adverse effects in the patient. Both the ultrasound waves and EM waves have the potential to result in adverse side effects. The safety implications of both forms of radiation will be considered here.

The potential damage that may be induced by ultrasound falls into two categories 1) mechanical damage and 2) thermal damage. Mechanical damage is predominately considered to be due to cavitation at high negative pressures [89]. The Mechanical Index (MI) is used as an indicator to predict the likelihood of mechanical damage [90] [91]. It is defined by,

$$MI = \frac{p_r}{\sqrt{f_{us}}} \tag{4.1}$$

where p_r (MPa) is the peak rarefaction pressure, derated for propagation through tissue, and f_{us} is the centre frequency of the ultrasound transducer. Thermal damage is caused by the absorption of ultrasound energy by the tissue which is converted to thermal energy and results in tissue heating. The thermal index (TI) [92] is defined as,

$$TI = \frac{W_p}{W_{deg}} \tag{4.2}$$

where W_p is the derated acoustic power at the depth of interest and W_{deg} is the energy estimated to raise the tissue equilibrium temperature by 1 $°C$ per unit volume. The temperature rise here can be estimated in the same way for HMI imaging [23]

$$\Delta T = \frac{2\alpha I_{sppa}}{\gamma_v} t \tag{4.3}$$

where α is the absorption coefficient of tissue, γ_v is the specific heat at constant volume for tissue and I_{sppa} is the spatial peak pulse average intensity.

Due to the importance of the United States market, the recommendations by the Food and Drug Administration (FDA) of the United States are the most frequently referenced standards, as regards medical device safety. The FDA has imposed global upper limits on the value of certain parameters as follows [93]:

1) The spatial peak temporal average intensity(I_{spta}) < 720 mW/cm^2 and
2) Mechanical Index (MI) <1.9 or I_{sppa} < 190 W/cm^2

The ultrasound transducer considered in the following investigation operates at f_{us} = 5 MHz. With Equation 4.1 the peak allowable rarefaction pressure is determined to be 4.25 MPa to satisfy the safety regulation. Assuming $\alpha = 0.7\ dB/cm/MHz$ [74] [87] and γ_v= 4.2 $J/cm^3\ /°C$ [23], and I_{sppa} equals half of I_{sptp} = 154 W/cm^2 for the modulation scheme in Section 3.2, the estimated temperature rise in 62.5 ms (10 cycles of ARF) is 1.0 $°C$ by Equation 4.3.

However the employed I_{spta} far exceeds the FDA imposed up limit of 720 mW/cm^2. The same is true for the majority of radiation force based imaging methods such as

HMI and ARFI. The reader is reminded that the FDA imposed limits were largely pragmatically decided in 1970s by referring to the output level used in the equipment up to that time [94]. Research into developing an acoustic output limit based on more accurate models [95] [96] may lead to the reformulation of the current implemented FDA standards to allow most ARF based imaging method including the EMA imaging to be introduced into clinical application.

For EM radiation, tissue heating is associated with the induction of current due to the nonzero conductivity of tissue during EM wave transmission [97]. The specific absorption rate (SAR) measures the power absorption per unit mass by human body from electromagnetic sources such as mobile phones and MRI machines. It is defined as [98]

$$SAR = \frac{\sigma(\vec{r})|E(\vec{r})|^2}{2\rho_0(\vec{r})} \tag{4.4}$$

where σ is the local effective conductivity (0.85 S/m for breast tumour tissue), ρ_0 is the local material density (1000 kg/m^3), and E is the local electric field. The maximum allowable SAR in torso under continuous EM radiation over 5 minutes imposed by FDA is 8 W/kg [99]. To assess the safety of the EMA imaging, the above parameters are substituted into Equation 4.4 resulting an electric field of E = 130 V/m. The European Directive 2004/40/EC recommends a maximum allowable E field of 60 V/m [100] to ensure the safety of workers against EM exposure in an occupational environment. For comparison, the E field strength measured in the near field of mobile phones ranges from 15 *V/m* to 60 *V/m* [101]. In the EMA system, the required electric field is subject to the system noise level, which is determined by the design of the EM transmitting, and receiving system and is not considered in the model of EMA imaging. Therefore the absolute value of electric field does not affect the simulation results, and an incident electrical field of 1 *V/m* is employed in the following investigation for simplification.

4.3 Modelling a breast tumour as a spherical inclusion

In this section, the complete simulation process for breast tumour detection using the EMA imaging is demonstrated. The breast tumour was modelled as a spherical inclusion with $r = 3\ mm$ in background tissue of infinite size. The mechanical properties listed in Table 4.1 were chosen to be consistent with data reported in previous literature [26] [102] [103] [104] and were assigned to the material composing the inclusion and background tissue.

The ultrasound transducer and the modulation scheme of the resulted ARF were introduced in Section 3.2. Briefly, a circular concave single element transducer operating at 5 *MHz* was employed and the resultant ARF was amplitude modulated to produce an oscillating force at 160 *Hz*. The dynamic response of the soft tissue to the excitation of the amplitude modulated ARF was simulated using the linear viscoelastic model developed in Section 3.3. The amplitude-modulated ARF can be decomposed into a step function and a harmonically oscillating component with zero mean. The dynamic response of the soft tissue to the step function force and the oscillating force can be evaluated separately and then superimposed on each other to obtain the dynamic response to the sum of the two forces as demonstrated in Figure 4.1. As only the harmonically oscillating component is responsible for inducing the Doppler effect and because a linear viscoelastic model is employed, only the harmonically oscillating force was considered. The peak harmonic force corresponds to a spatial peak temporal peak intensity of $I_{sptp} = 154\ W/cm^2$, and is used in the rest of the investigation.

Table 4.1 The material properties assigned to the linear-viscoelastic model (E is the Young's modulus, η_s the shear viscosity, ρ the material density, α the ultrasound attenuation coefficient, ε the relative electrical permittivity, σ the electrical conductivity, and μ the relative magnetic permeability [26] [102] [103] [104] [105] [106].

Parameter	Background tissue	Tumour tissue
E	$3\ kPa$	$9\ kPa$
η_s	$1.2\ Pa \cdot s$	$2.0\ Pa \cdot s$
ρ	$1000\ kg/m^3$	$1000\ kg/m^3$
ν	0.499	0.499
α	0.7 dB/*cm/MHz*	0.7 dB/*cm/MHz*
ε	18	57.5
σ	0.13 *S/m*	0.85 *S/m*
μ	1	1

The relative permittivity and electrical conductivity of healthy and cancerous breast tissue were surveyed in previous studies [105] [106]. Representative values summarized in Table 4.1 were assigned to the inclusion and background tissue. The incident EM wave was set to propagate in the + y direction with an E field of amplitude of 1 *V/m* and polarized in z direction. This was the same as in Figure 2.1 except that the small dielectric sphere was replaced by a breast tumour model and the motion of the breast tumour was induced by the oscillating ARF. The UC and the FDC were simulated using the models and methods developed in Section 3.4 and Section 3.5.

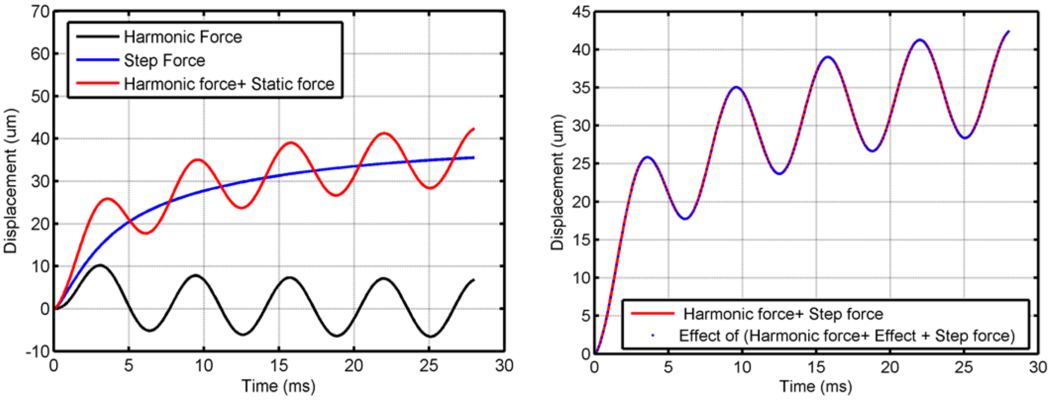

a

b

Figure 4.1 (a) The dynamic response of homogeneous linear viscoelastic tissue ($E = 3$ kPa, $\eta_s = 1.2$ Pa · s and $\rho = 1000$ kg/m^3) to a step force (blue) and a harmonic force (black) and the sum (red) (b) The dynamic response of linear viscoelastic soft tissue to the sum of two forces is equivalent to the sum of the dynamic responses of the same tissue to each of the two forces as would be expected for linear simulation.

Results and Discussion:

The dynamic response of the boundary of the spherical inclusion is illustrated in Figure 4.2. Figure 4.2a presents three snapshots of the spherical inclusion at time corresponds to 0 *ms* (A): before the ARF excitation, 9.4 *ms* (B) at a local maximum and 12.6 *ms* (C) a local minimum of the oscillatory ARF. It can be seen that the spherical inclusion undergoes non-uniform motion: displacement of the whole volume as well as boundary deformation. In Figure 4.2b, the displacements of locations on the spherical boundary corresponding to ϕ = -90°, 0°, and 90° degrees as functions of time are compared. In Figure 4.3, the amplitude and phase of the oscillation experienced by the spherical boundary is illustrated as functions of ϕ. The oscillation observed at positions further away from the axis of the applied ARF was significantly smaller (1.5 μm versus 5 μm) than and lagging behind (100°) that observed on the axis. A detailed discussion of the phenomenon can be found in Section 4.4.

The simulated FDC and UC are shown in Figure 4.4. For the modelled breast tumour, which was an electrically small spherical scatterer, the scattered EM field resembled the radiation pattern of a Hertz dipole as shown in Figure 4.4c and Figure 4.4d. The detectability of the induced Doppler effect can be roughly estimated by the ratio of the FDC and UC, which is collectively determined by a series of parameters such as the ARF excitation, electrical and mechanical properties of both the inclusion and background medium. From Figure 4.4, it is seen that the strongest Doppler effect is observed at the backward scattering position (φ = 180°). Therefore it is recommended that the EM receiver should be located at a position close to the ultrasound transducer.

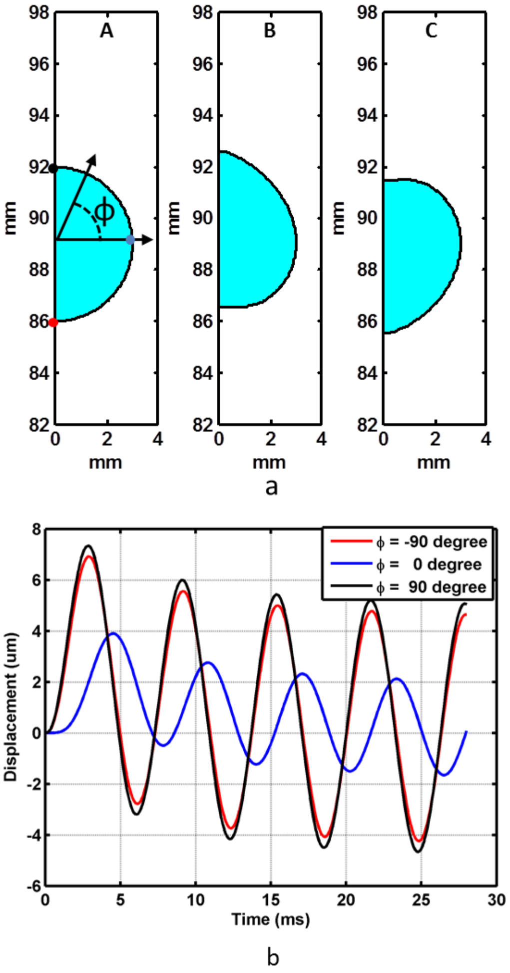

a

b

Figure 4.2 The dynamic response of the spherical inclusion to amplitude modulated ARF. a: The snapshot of the spherical inclusion at t = 0 ms (A: before ARF was applied), t = 9.4ms (B: ARF is at local maximum), and t = 12.6 ms (C: ARF is at local minimum; b: the time-varying displacement at different locations at the spherical boundary shown in A (red spot: ϕ = -90°, blue spot: ϕ = 0°, and black spot: ϕ = 90°). Note that to illustrate the deformation of the spherical boundary, the actual displacement in (a) was magnified by 100 times

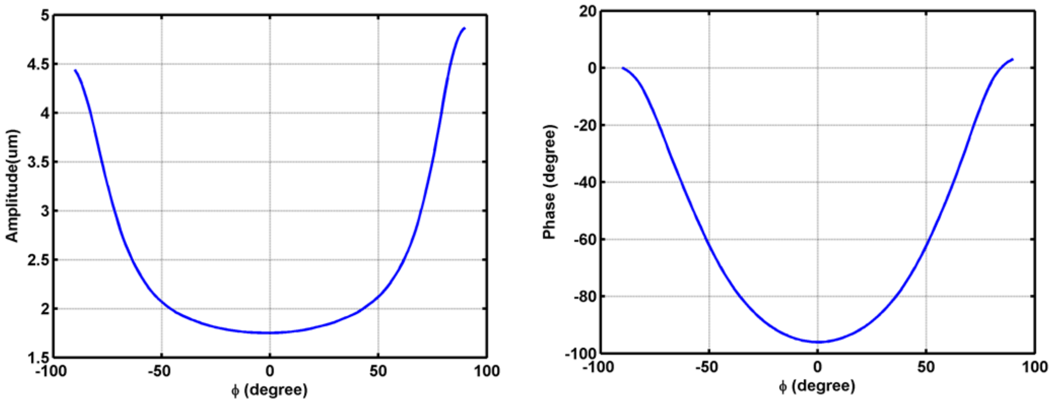

a b

Figure 4.3 The amplitude (a) and phase (b) of the oscillatory displacement of the spherical boundary of the inclusion under the excitation of ARF as a function of ϕ

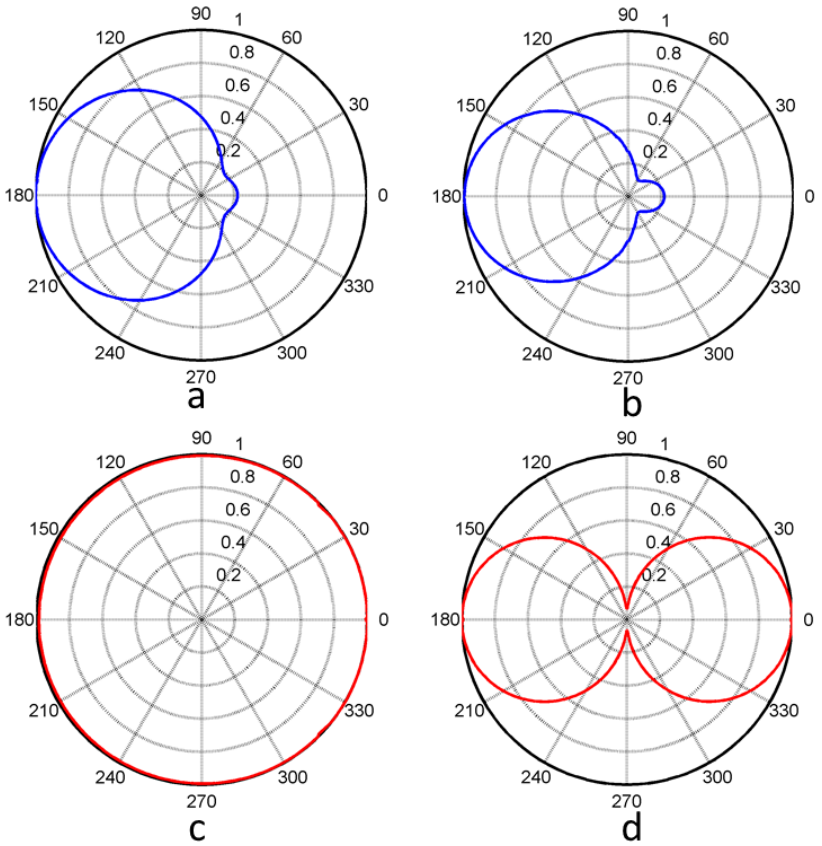

Figure 4.4 The simulated FDC (a: in the y-x plane and b in the y-z plane) received a focal distance (89 mm) away from the centre of spherical inclusion and the simulated UC(c: in the y-x plane and d in the y-z plane) as functions of the bi-static angle φ between the transmitter and receiver.

4.4 Impact of mechanical properties

Method:

Here the effect of varying the mechanical parameters of the tissue on the EMA signal was investigated. The induced Doppler effect in EMA imaging is related to the amplitude of FDC relative to the UC instead of its absolute amplitude. For investigations in which the UC is fixed, the normalized FDC is presented whilst for investigations with varying UC, the ratio of FDC and UC is also presented. The electrical parameters were fixed (ε_{ic}= 57.5 and σ_{ic} = 0.85 *S/m* and ε_{bg}= 18 and σ_{bg} = 0.13 *S/m*) so that, for an inclusion of fixed size, the UC in the scattered EM signal would not vary and therefore only the variations in the FDC are investigated. Simulations were conducted for spherical inclusions of different sizes with varying Young’s modulus, shear viscosity and material density. The mechanical properties are given in Table 4.1 and were varied in ranges clinically relevant for breast tissue [26] [102] [103] [104]. The ARF had a full width half maximum (FWHM) of 2 *mm*, and was induced along the +y direction with its focal point coincident with the centre of the breast tumour. The dynamic responses of the spherical inclusions of different size (r_{ic}= 0.5 *mm*, 1.5 *mm*, 4.5 *mm*, and 6 *mm*) were simulated.

Results and discussion: mechanical response

Figure 4.5 shows the effect upon the FDCs of varying the Young's modulus of the inclusion E_{ic} from 9 kPa to 42 kPa for 0.5 mm and 6 mm radius inclusions. The maximum displacement for both cases was at $\varphi = \pm 90°$ with a minimum at $\varphi = 0°$. When $r_{ic} = 0.5$ mm, the entire volume of the spherical inclusion was within the region of excitation (ROE). The oscillation of the soft tissue at its spherical boundary was induced by the excitation of the oscillating ARF directly. The difference in the amplitude of oscillation at $\phi = \pm 90°$ and $\phi = 0°$ was the result of the lateral gradient of the ARF within the ROE. For $r_{ic} = 6$ mm, the spherical inclusion is greater than the ROE and the direct ARF excitation is confined in the volume near the axis. The induced shear wave then propagated laterally out of the ROE with the energy spreading cylindrically, causing the oscillation of soft tissue outside ROE. Therefore a greater difference in the amplitude of oscillation was observed for a larger inclusion. The effect of propagation can be seen in the phase of the oscillation along the boundaries, where the phase increased by a maximum of 6° for $r_{ic} = 0.5$ mm whereas it had a maximum of 224° for $r_{ic} = 6$ mm. In Figure 4.5, as E_{ic} increases from 9 kPa to 42 kPa, the difference in the amplitude and phase of the oscillation at $\phi = \pm 90°$ and $\phi = 0°$ are reduced for both $r_{ic} = 0.5$ mm and 6 mm. This suggests that, as the spherical inclusion become stiffer with increasing Young's modulus, it behaves more like a rigid body and oscillated more uniformly. Data for the 1.5 *mm* and 4.5 *mm* radius inclusions is not shown, however it shows similar trends to what is seen here.

Figure 4.6 shows the effect of changing the viscosity of the inclusion η_{s_ic}. The angular dependence was similar to that in Figure 4.6. Increasing the shear viscosity decreased the amplitude. This is explained by considering that the shear viscosity is proportional to the imaginary part of shear modulus. Increasing the shear viscosity led to a greater absolute value of the shear modulus, and therefore reduced the tissue peak displacement when the applied force was held fixed. Figure 4.7 shows that increasing ρ_{ic} from 800 kg/m^3 to 1200 kg/m^3 has very little impact on the amplitude and phase of the oscillation along the spherical boundary.

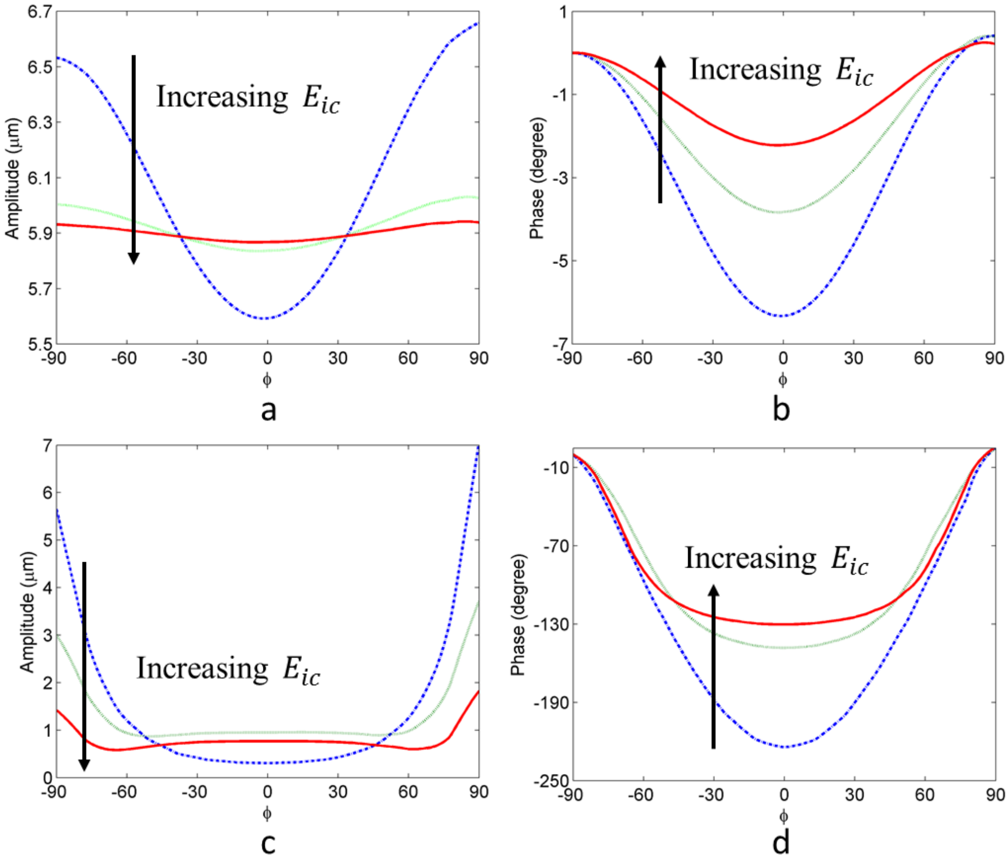

Figure 4.5 The amplitude (a,c) and phase (b,d) of the oscillation at the spherical boundary of inclusions with r_{ic} *= 0.5 mm (a,b), and 6 mm (c,d) as functions of* ϕ*.* E_{ic} *is 9 kPa (blue curve) 24 kPa(green curve) and 42 kPa (red curve). The background medium is* E_{bg} *= 3 kPa. Horizontal axis unit: degree*

The mechanical properties of both the inclusion tissue and background tissue affected the FDC by influencing the dynamic response of soft tissue. The simulated FDC received at a position that was placed next to the ultrasound transducer that was 89 *mm* away from the centre of the spherical inclusion in the backscattering direction are shown in Figure 4.8 to Figure 4.10.

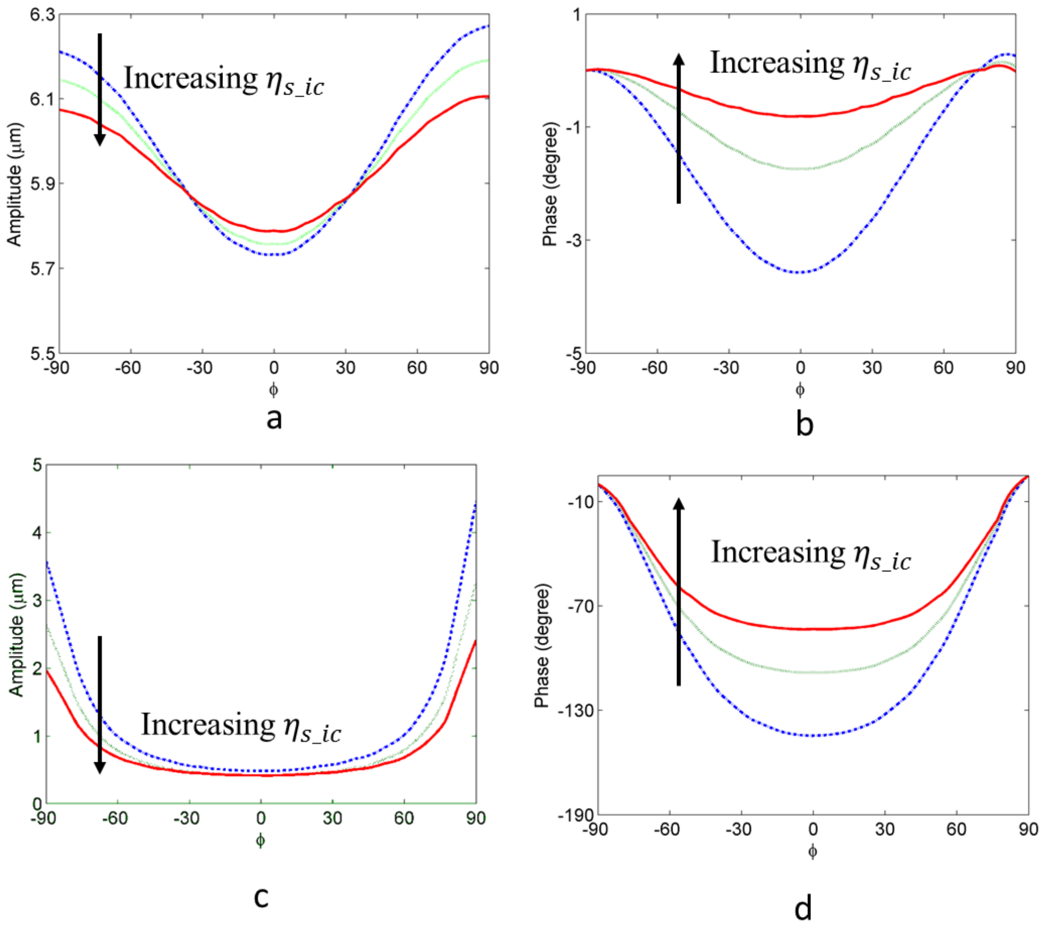

Figure 4.6 The amplitude (a,c) and phase (e,h) of the oscillation at the spherical boundary of inclusions with r_{ic} = 0.5 mm (a,b), and 6 mm (c,d) as functions of ϕ. η_{s_ic} is 3.2 $Pa \cdot s$ (blue curve) 7.2 $Pa \cdot s$ (green curve) and 10.2 $Pa \cdot s$ (red curve). The background medium viscosity is 1.2 $Pa \cdot s$. Horizontal axis unit: degree

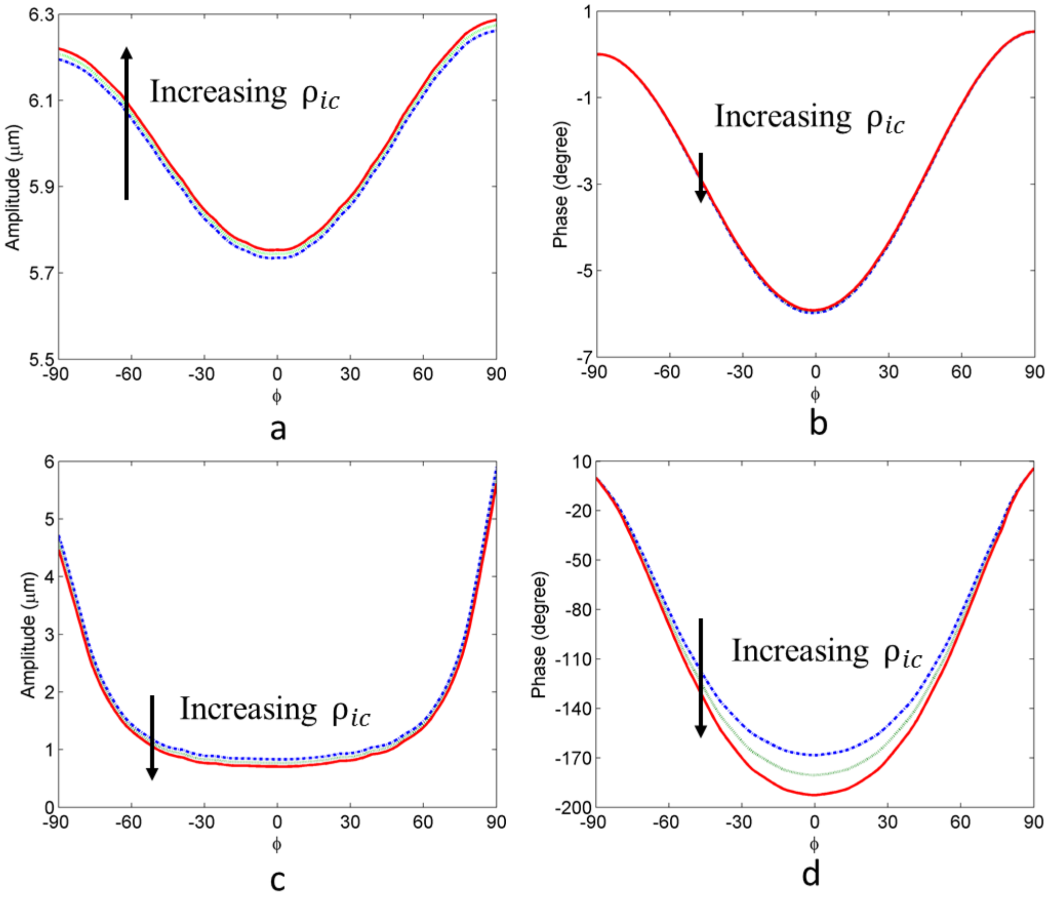

Figure 4.7 The amplitude (a,c) and phase (e,h) of the oscillation at the spherical boundary of inclusions with r_{ic} *= 0.5 mm (a,b), and 6 mm (c,d) as functions of* ϕ. ρ_{ic} *is 800 kg/m*^{3}*(blue curve) 1000 kg/m*^{3} *(green curve) and 1200 kg/m*^{3} *(red curve). The background medium* ρ_{bg} *= 1000 kg/m*^{3}*. Horizontal axis unit: degree*

Figure 4.8 presents the impact of varying the Young's modulus of both the spherical inclusion and background tissue within a clinically feasible range. For the smallest inclusion (r_{ic} = 0.5 *mm*, Figure 4.8a), a 3 fold increase in the Young's modulus of the background tissue E_{bg} led to a 32% decrease in the FDC. On the other hand, as r_{ic} was small, the impact of the material properties of the inclusion was small and increasing E_{ic} from 3 *kPa* to 42 *kPa* led to less than 3% variation in the FDC. For inclusions of greater size (r_{ic} = 1.5 *mm*, *4.5 mm* and *6 mm*), the properties of the inclusion contributed more to determine the dynamic response. Therefore the same changes in the Young's modulus of the inclusion led to greater variations in the FDC compared to when r_{ic} = 0.5 *mm*. Variations in the FDC were up to 15% (r_{ic} = 1.5 *mm*, Figure 4.8b), 40% (r_{ic} = 4.5 *mm*, Figure 4.8c) and 50% (r_{ic} = 6 *mm*, Figure 4.8d).

Increasing E_{ic} from 3 *kPa* to 42 *kPa* in Figure 4.8 (c-d) does not increase the FDC monotonically. Further when r_{ic} = 4.5 *mm* and 6 *mm*, the greatest amplitude of the FDC was observed when the background tissue was stiffest. The phenomena suggest that resonance behaviour in the inclusion may be present. This was corroborated by considering the case of E_{bg} = 9 *kPa* and r_{ic} = 4.5 *mm*, the peak FDC was observed at E_{ic} = 6 *kPa* with a shear wavelength λ_s = 8.9 *mm* in the inclusion tissue, which was twice of r_{ic}. When r_{ic} = 6 *mm* the peak FDC is observed at E_{ic} = 10 *kPa* with λ_s = 11.4 *mm*, again approximately twice of r_{ic}. For E_{ic},> 10 *kPa*, the wavelength of the shear wave exceeded the size of the inclusion and there was no resonance condition, and the amplitude of FDC decreases due to the stiffer tissue. The resonance effect can also be produced by varying the ARF excitation frequency with fixed mechanical properties. In clinical setting, the resonance effect can be exploited to determine the size of the inclusion be sweeping the ARF excitation frequency if the mechanical properties are known. The frequency at which the peak signal is observed

Figure 4.9 shows the impact of varying shear viscosity. Again for smaller inclusions, the FDC was mainly determined by the background tissue properties. A 3 fold increase in the shear viscosity of the background tissue η_{s_bg} led to a 47% decrease in FDC whilst a 3 fold increase in the shear viscosity of the inclusion η_{s_ic} only led to a 3% increase in FDC. In contrast, for larger inclusions, the same change in η_{s_ic} led to a 10% (r_{ic} = 4.5 *mm*, Figure 4.10c) and 18% (r_{ic} = 6 *mm* Figure 4.10d) in the FDC change respectively.

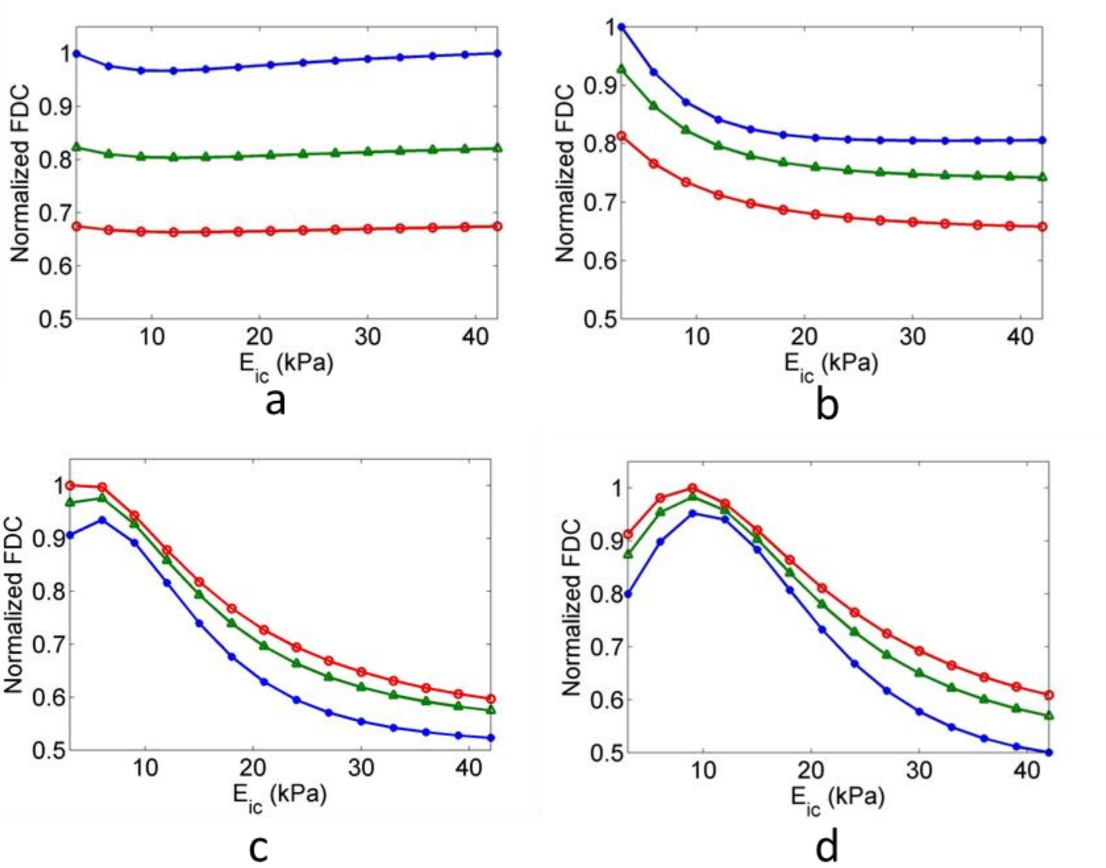

Figure 4.8 The impact of Young's modulus: blue star (Blue star: E_{bg} *= 3 kPa, Green triangle:* E_{bg} *= 6 kPa and red circle:* E_{bg} *= 9 kPa) on the FDC for spherical inclusions with (a)* r_{ic}*= 0.5 mm, (b)* r_{ic}*= 1.5 mm,(c)* r_{ic}*= 4.5 mm and (d)* r_{ic}*= 6 mm*

Figure 4.10 illustrates the effect of varying material density. Increasing ρ_{bg} from 800 *kg/m*^{3} to 1200 *kg/m*^{3} led to a 14 % decrease in the FDC whilst increasing ρ_{ic} from 800 *kg/m*^{3} to 1200 *kg/m*^{3} lead to 2% variation. For inclusions of greater size, the variation in FDC was 10% (r_{ic} = 1.5 *mm*, Figure 4.10c) and 15% (r_{ic} = 6 *mm*, Figure 4.10d). Please note that the range of density investigated here was much larger than what is typically seen in soft tissues (900-1100 kg/m^3 [107] [108] except for bone (1900 kg/m^3 [109]) to demonstrate the material density dependence of the FDC. In a clinical setting, material density is unlikely to be an important factor in determining the FDC because of the small variation of the tissue density.

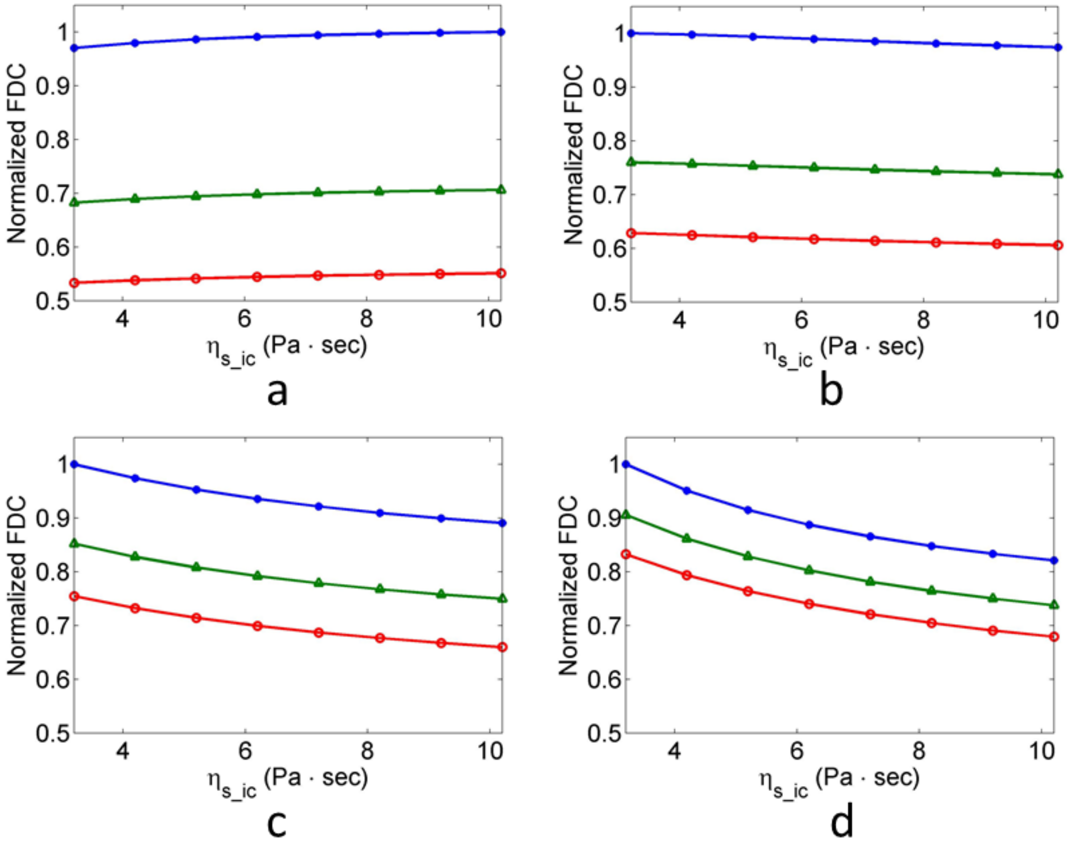

Figure 4.9 The impact of shear viscosity: (Blue star: η_{s_bg} = 1.2 Pa · s, Green triangle: η_{s_bg} = 2.2 Pa · s and red circle: η_{s_bg} = 3.2 Pa · s) on the FDC for spherical inclusions with (a) r_{ic}= 0.5 mm, (b) r_{ic}= 1.5 mm,(c) r_{ic}= 4.5 mm and (d) r_{ic}= 6 mm.

It is noteworthy that in Figure 4.8a the FDC decreases by 3% at first before it increases to unity again. In Figure 4.9a, it increases from 0.97 to 1 with increased η_{s_ic} rather than following the same trend observed in Figure 4.9b-c. These small fluctuations in the FDC were likely to be attributed to the complicated interaction between several factors. First, when $r_{ic} = 0.5\ mm$, the entire inclusion was within the region of excitation and because ARF decreases rapidly in the lateral direction there will be a non-uniform excitation around the surface of the inclusion. Second, varying the mechanical properties of the tissue further complicates the distribution of the amplitude and phase of the oscillation along the spherical boundary. The induced Doppler effect in the scattered EM signal was sensitive to the small perturbations of the amplitude and phase of the oscillation, which led to the observed relationship between FDC and mechanical properties shown in Figure 4.8a and Figure 4.9a.

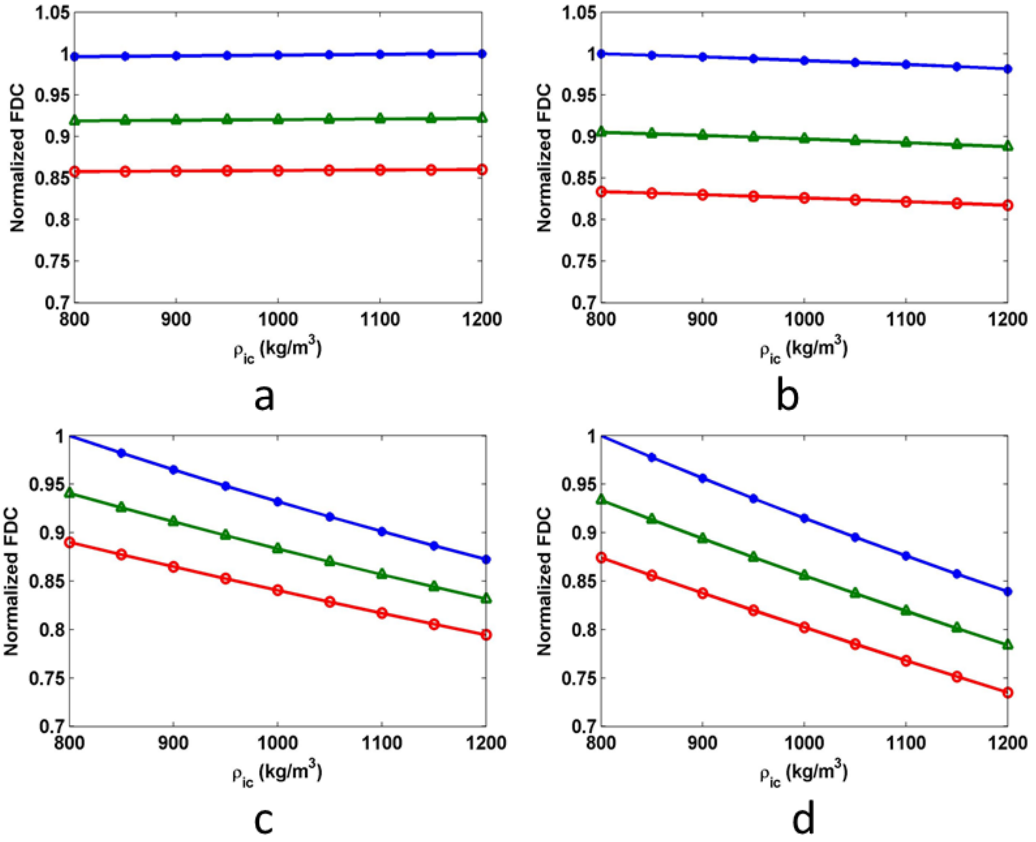

Figure 4.10 the impact of density: (Blue star: ρ_{bg} *=800 kg/m*^{3}*, green triangle:* ρ_{bg} *=1000 kg/m*^{3}*and red circle:* ρ_{bg} *=1200 kg/m*^{3}*) on the FDC for spherical inclusions with (a)* r_{ic}*= 0.5 mm, (b)* r_{ic}*= 1.5 mm,(c)* r_{ic}*= 4.5 mm and (d)* r_{ic}*= 6 mm.*

4.5 Impact of electrical properties

Method:

Contrast in the permittivity ε_{ic} and electrical conductivity σ_{ic} of the inclusion will affect the scattering of both the UC and the FDC. For this investigation, the mechanical parameters listed in Table 4.1 were employed and r_{ic} was held fixed at 3 *mm*. When r_{ic} = 3 *mm*, the size of the spherical inclusion was much smaller than a wavelength of the EM wave at 434 *MHz* in soft tissue (8 *cm*). The EM scattering from such a spherical inclusion falls into the Rayleigh scattering regime. The electrical conductivity and relative permittivity of the inclusion tissue were varied to investigate their effects on both the UC and the FDC.

Results and Discussion:

Figure 4.11 shows the impact of increasing ε_{ic} from 50 to 80 with σ_{ic} = 0.85 *S/m* and σ_{bg} = 0.13 *S/m*. The UC increased by 23% as ε_{ic} increased from 50 to 80. In contrast the FDC increased only by 13%. As a result FDC/UC decreased by 0.7 dB. The noticeable discrepancy in the trends between the FDC and the UC as a function of ε_{ic} was due to the dependence of the FDC on the tissue dynamics. FDC was not only sensitive to the electrical contrast between the inclusion tissue and background tissue, but also the wavenumber of the EM wave in both the inclusion and the background, as suggested by Equations 3.1 to 3.5. The change in ε_{ic} from 50 to 80 increased the EM propagation constant inside the spherical inclusion by 20% which affected the scattering. Similar phenomena are also reported in Section 3.4 in the 2D simulations for a vibrating cylinder.

The FDC is generally many orders of magnitude smaller (~70 dB~80 dB) than the UC. Therefore the UC can be used to represent the strength of the scattered EM signal. The ratio between the FDC and the UC can be used as an estimator of the magnitude of induced Doppler effect. The above results indicate that whilst the presence of electrical contrast is necessary for the generation of the EMA signal, the inter-tumour variation of electrical properties is unlikely to cause detectable change in the induced Doppler effect in an infinite homogeneous background medium. In clinical scenarios the background tissue is finite and heterogeneous. Other scatterers, for example the interfaces between different organs may are not acoustically stimulated, also scatter EM waves without inducing any Doppler effect. The scattered EM energy contributes to the UC and effectively reduces FDC/UC, which is not in favour of EMA imaging. It is speculated that increasing the contrast electrical properties between the inclusion and the background tissue will help reduce the influence of undesired scatterers. The contrast may be increased by injecting contrast agents which is briefly discussed in Chapter 6.

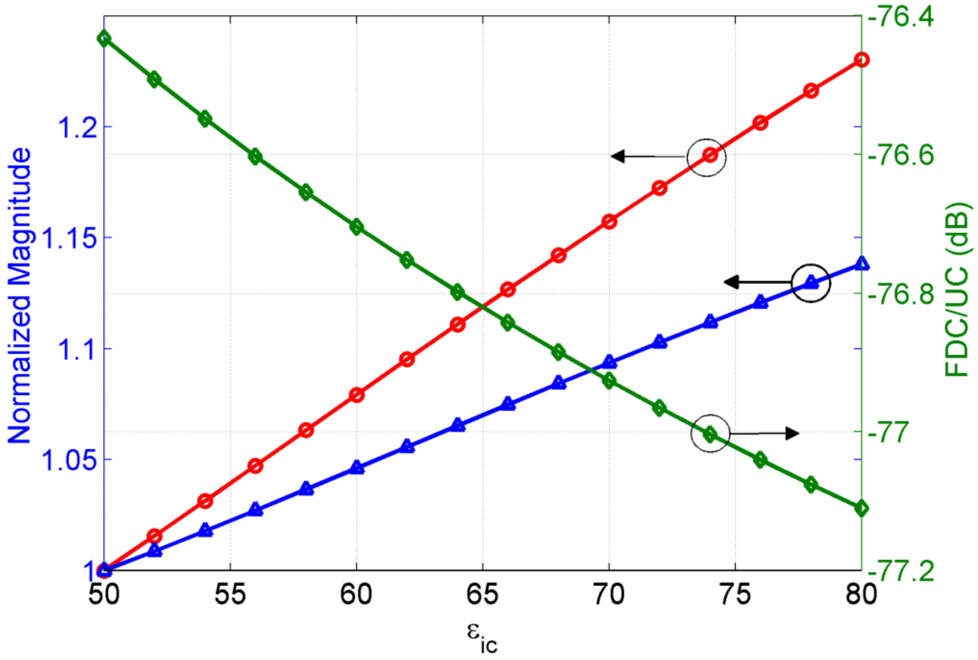

Figure 4.11 The impact of the relative permittivity of the inclusion material on the FDC (Blue triangle) and the UC (red circle) and FDC/UC in dB (green diamond). The arrows indicate the appropriate vertical axes.

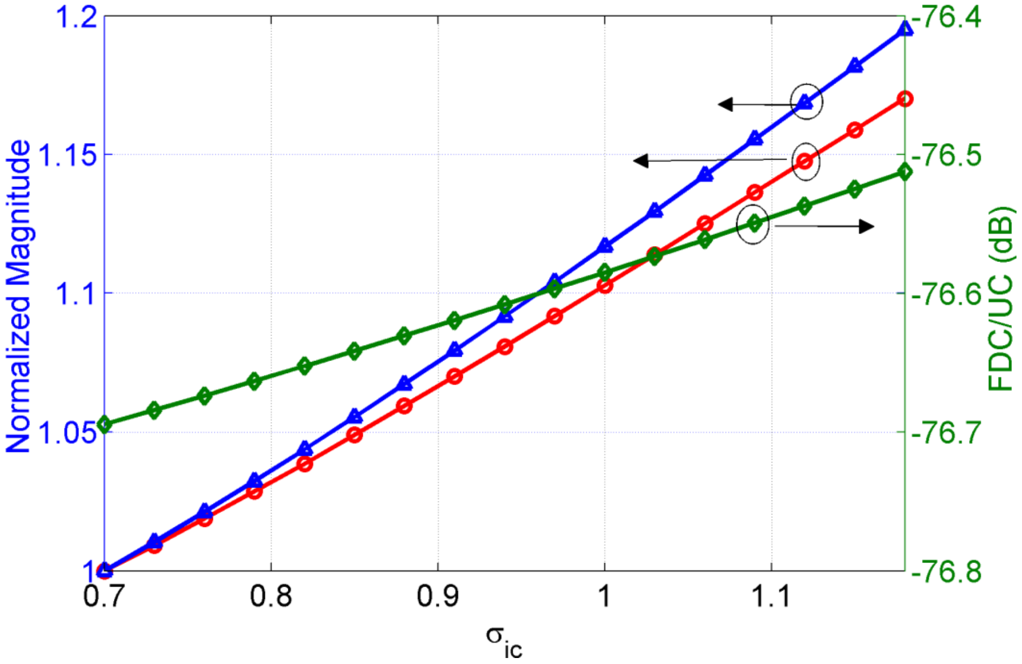

Figure 4.12 The impact of the electrical conductivity of the inclusion material on the FDC (blue triangle) and UC (red circle) and FDC / UC in dB (green diamond). The arrows indicate the appropriate vertical axes.

4.6 Impact of inclusion size

Method:

The investigation of the impact of size of the spherical inclusion was conducted, with the mechanical properties and electrical properties summarized in Table 4.1, and the r_{ic} was varied from 1 mm to 10 mm.

Results and Discussion:

In Figure 4.13 the simulated FDC from a spherical inclusion excited by a harmonic ARF is compared to the analytical solution and the FEM-SBC solution for a rigid sphere of the same size subject to a uniform harmonic oscillation. Because the size of the inclusions studied falls in the Rayleigh regime, the scattering cross section is approximately proportional to r_{ic}^3. That is, for a rigid sphere with uniform motion, the amplitude of both the UC and the FDC are approximately proportional to r_{ic}^3. However in a clinical scenario where tissue is soft, only the volume of the tissue in the focal region of the ultrasound transducer is excited by the ARF directly. Shear wave is created in the region of excitation and spread cylindrically out of the region of excitation. The amplitude of the shear wave is smaller at positions further away from the region of excitation due to the cylindrical spreading of energy and attenuation due to the shear viscosity. Therefore the amplitude of oscillation of the soft inclusion is smaller than if it was rigid. As a result it is seen in Figure 4.13 that the curves for uniform oscillation (green and blue) increase at a rate faster than the ARF excited motion (red curve). As the amplitude of UC is an solely dictated by r_{ic} and is unaffected by tissue dynamics, the FDC increases at a rate smaller than UC for ARF excited inclusion. In Figure 4.14, ratio of the FDC and the UC decreases by 24 dB when r_{ic} is increased from 1 mm to 10 mm. The results suggest that, under the current configuration, a larger inclusion is more difficult to detect as the Doppler effect in the received EM signal reduces with increasing inclusion size.

To be able to detect large breast tumours, the EMA system can be configured in a scan mode where the ultrasound focus is steered across the breast tumour and a 2D EMA image of the scanned cross section is produced. In this configuration, when the ultrasound focus is coincident with the boundaries of the large tumour, an EMA signal can be detected. However, as the larger tumour produces a stronger UC making the FDC appears to be relatively weaker, it is speculated that a small tumour in the EMA image will appear a small area of high signal intensity (corresponds to the stronger Doppler effect observed for a smaller inclusion) whilst a appear tumour will have a large area of low signal level.

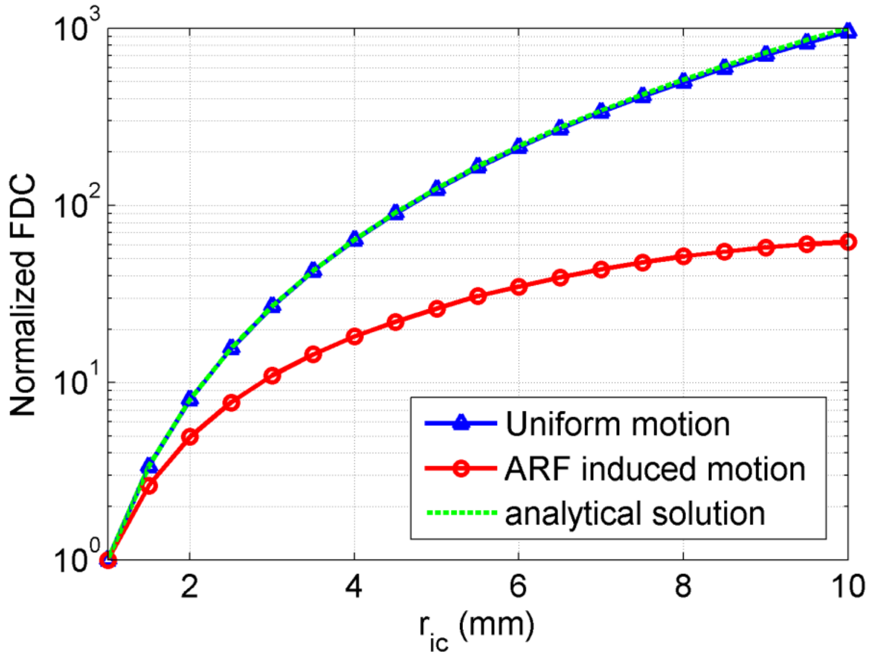

Figure 4.13 The FEM-SBC simulated impact on the FDC of the varying r_{ic} *from 1 mm to 10 mm when the spherical inclusion oscillates uniformly and harmonically (blue triangle) or oscillates under ARF excitation (red circle) together with the analytical solution given in Chapter 2 (green dot).*

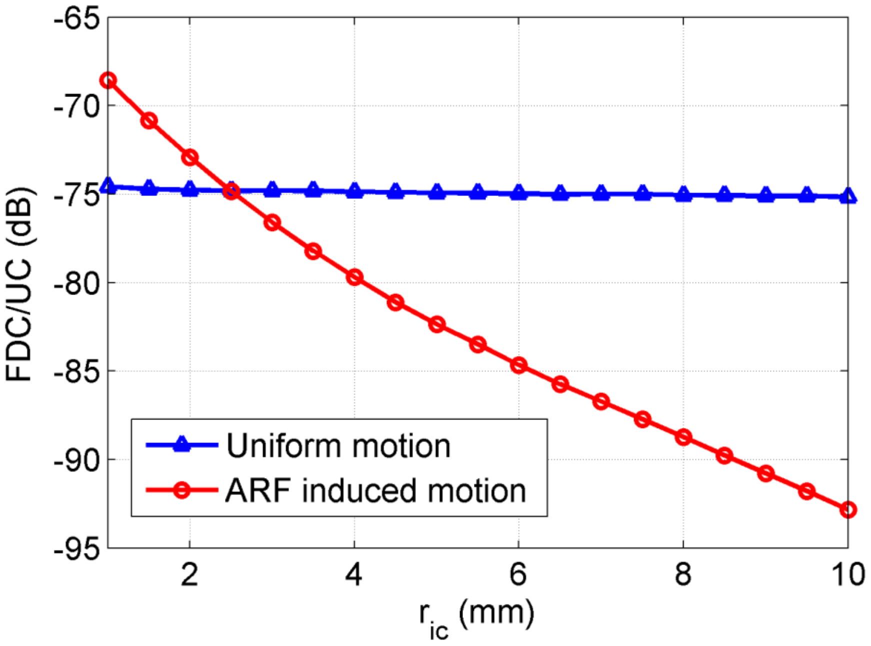

Figure 4.14 FEM-SBC simulated ratio of the FDC and UC in dB for uniformly and harmonically oscillating sphere (blue triangle) and ARF excited spherical inclusion (red circle)

4.7 Summary

The feasibility of using the EMA imaging technique for breast tumour detection has been investigated in this chapter. The tumour was modelled as a spherical inclusion embedded in an infinitely large volume of background tissue. For all scenarios considered there may be issues with safety based on ultrasound levels employed in this work. However, these safety issues are similar to other harmonic radiation force methods and are under evaluation by safety working groups.

The mechanical properties of both the inclusion and the background tissue were found to impact the resultant FDC via the dynamic mechanical response of the tissue boundary. Varying the elastic properties within the clinically relevant range has led to changes in the FDC up to 50%. It was found that resonance behaviour was captured by EMA imaging at specific size and properties of the spherical inclusion. Varying the electrical properties affected both the FDC and UC, by up to 20%. The investigated ranges of relative permittivity and conductivity have led to up to a 0.7 dB decrease and a 0.2 dB increase in the ratio of the two components. It is speculated that the high electrical contrast between the inclusion and background tissue help reduce the undesired signals from other unexcited EM scatterers. The magnitude of the received EM signal is mainly dictated by the size of the spherical inclusion. The FDC did not increase with inclusion size as rapidly as the UC, which led to a decrease of 26 dB in the ratio between the two components as the radius of the inclusion was increased from 1 mm to 10 mm.

In conclusion, there are several issues need to be addressed before EMA imaging can be clinically deployed. First of all, the FDC signal is typically more than 68 dB (see Figure 4.14) below the UC signal level in the simulated scenarios. Detecting such a small Doppler effect in the scattered EM signal is a very challenging task itself. Additional noise sources include the EM reflections from other structures other than the targets one aim to detect, phase noise in the EM signals and thermal noises generated in the EM hardware will make the signal detection more difficult. Overcoming above listed problems require novel signal processing techniques as well as robust hardware such as EM transmitter and detectors. This is discussed in Chapter 6. Another issue is related to the imperfect focusing of the acoustic force field. The current configuration of EMA imaging does not include a mechanism to effectively monitor the exact location of the acoustic focus. When the acoustic force field is imperfectly focused, there will be a mismatch between the locations the operator trying to image and the locations that are actually imaged.

Chapter 5 EMA monitoring of HIFU therapy

5.1 Introduction

In this chapter, the computational model for High Intensity Focused Ultrasound (HIFU) therapy and monitoring is developed to investigate the feasibility of real-time thermal therapy monitoring with EMA imaging. As discussed in Chapter 1 HIFU ablates tissue at depth. The thermal process changes the acoustic, elastic and electrical properties of the tissue. The ablation process may result in a detectable change in the EMA signal. In addition, as the application is therapeutic and the diagnostic safety limit does not apply, the EMA imaging may employ the therapeutic ultrasound transducer in the HIFU system for tissue excitation and higher ultrasound power to induce greater Doppler effect in the scattered EM signal.

The chapter is organised as follows: first, an acoustic model for HIFU propagation and heating is included in the EMA model. Second, a case study is presented to demonstrate the complete simulation process. Third, the sensitivity of the EMA signal to HIFU induced changes in ultrasound attenuation coefficient, shear viscosity and Young’s modulus is investigated. Finally the impact of ultrasound intensity is studied.

5.2 A HIFU-EMA model

The EMA model developed in Chapter 3 is extended to include the HIFU thermal ablation process. The linear acoustic model employed previously is replaced by a nonlinear acoustic propagation and ablation model. The simulation framework is shown in Figure 5.1.

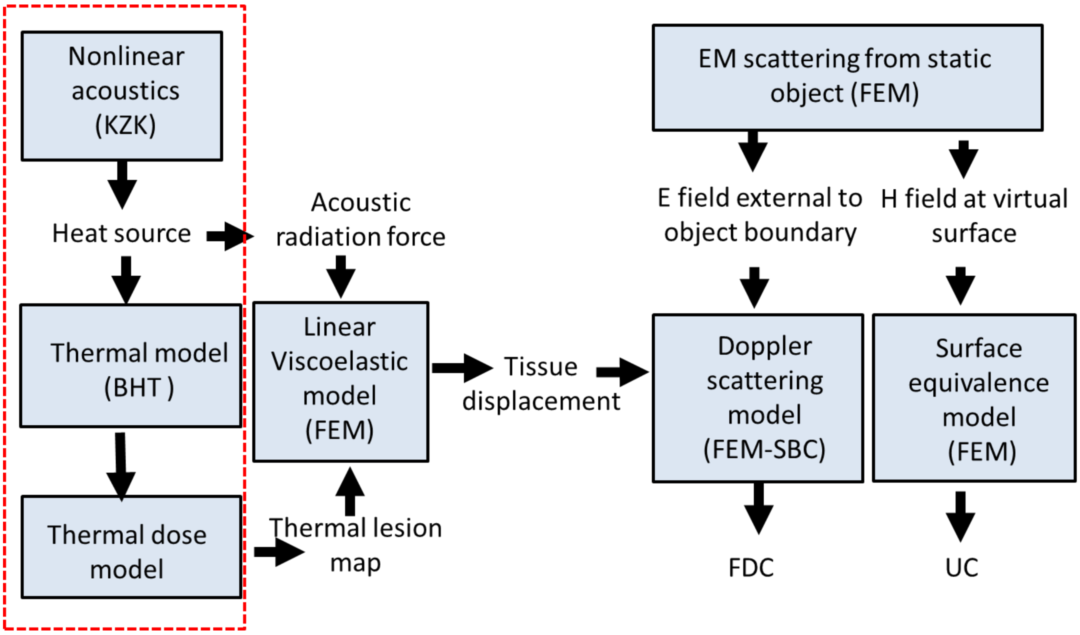

Figure 5.1 Block diagram of the HIFU-EMA model to illustrate the simulation process: inside the red dash line box is the HIFU model consisting of a non-linear acoustic model, a thermal model and a thermal dose model. Outside the red box is the EMA model as introduced in Chapter 3 with an additional surface equivalence model.

The HIFU model employed in this investigation is modified from an existing HIFU simulator [110]. Within the HIFU simulation, a non-linear acoustic model based on Khokhlov-Zabolotskaya-Kuznetsov (KZK) equation is used to solve for the pressure field and heating rate map in the tissue. The key assumption of KZK equation is strictly forward propagating acoustic wave, which is valid as scattering of acoustic waves is not considered here. Defining the direction of the beam propagation as y with the transducer surface lying in the x-z plane perpendicular to y, the KZK equation can be written as [111] [112]:

$$\frac{\partial^2 p}{\partial y \partial \tau} = \frac{c_0}{2} \nabla_{\perp}{}^2\, p + \alpha(f) \frac{\partial^3 p}{\partial \tau^3} + \frac{\beta}{2\rho_0 c_0^3} \frac{\partial^2 p^2}{\partial \tau^2} \tag{5.1}$$

where p is the pressure, c_0 the small signal sound speed, β the nonlinearity coefficient, ρ_0 the density, $\tau = t - y/c_0$ the retarded time and $\nabla_{\perp}{}^2$ the Laplacian operator in the x-z plane. The frequency dependent ultrasound attenuation coefficient in the soft tissue is assumed to follow a power law described by [113],

$$\alpha(f) = \alpha_0 \times \left(\frac{f}{1\ MHz}\right)^{\varsigma} \tag{5.2}$$

where α_0 is the attenuation at 1 *MHz* and ς is the power law exponent. The nonlinear acoustic model output a map of heating rate $Q = \int 2\alpha(f) I(f) df$ [114]. The resultant ARF is given by [52],

$$ARF = \frac{Q}{c_0} \tag{5.3}$$

and used as an input to the viscoelastic model. The heating rate map is used as an input to the thermal model based on bio-heat transfer equation (BHTE) [115],

$$\rho C_t \frac{\partial T}{\partial t} = k\nabla^2 T - w_b C_b (T - T_a) + Q \tag{5.4}$$

where C_t is the heat capacity, T the temperature, k the tissue thermal conductivity, w_b the blood perfusion rate, C_b the heat capacity of blood and T_a the arterial blood temperature. Note that the heat loss due to the blood flow is not considered in this work. Solving Equation 5.4 yields a spatial map of temperature T as a function of the HIFU exposure time.

The thermal damage to the underlying tissue is assessed using a cumulative equivalent minute model [116] with a reference temperature of $43°C$ (CEM$43°C$). This model converts the thermal dose applied in a thermal course of varying temperature to minutes of an equivalent thermal course at a constant temperature of $43°C$. The tissue region with accumulated thermal dose exceeding 240 CEM$43°C$ minutes is regarded as thermally coagulated and hence is defined as a thermal lesion. The thermally coagulated tissue is then assigned appropriate mechanical properties and electrical properties (see Section 5.3).

The EMA model uses the architecture presented in Chapter 3 except that an additional ‘surface equivalence model’ is added into the simulation framework. The role of the ‘surface equivalence model’ has been discussed in Section 3.4. The virtual surface of the surface equivalence model is chosen to be a sphere with a radius of 10 mm. From here on the model introduced in this section is referred to as the HIFU-EMA model.

5.3 Simulating EMA during HIFU exposure

Method:

In this section, the complete simulation process for monitoring thermal lesion formation using the EMA imaging is demonstrated. The acoustic source used in this study was a circular single element focused transducer as illustrated in Figure 6.2. The transducer has an aperture radius $a = 3.2\ cm$, a radius of curvature $d = 6.26\ cm$ and a centre frequency of 1.1 MHz. This matches the property of a commercially available HIFU transducer (H101, Sonic Concepts, Woodinwill, WA). The resultant ARF was amplitude modulated by a 160 Hz sinusoidal signal using the scheme introduced in Section 3.2.

The temperature dependent non-linear acoustic properties of bovine liver tissue have been reported in [113]. An ambient temperature of $37\,°C$ was assumed. The 'non-linear acoustic model' and the thermal model are not capable of updating temperature dependent material properties during the simulation. Therefore the pre-treatment non-linear acoustic properties (Table 5.1) and thermal properties (Table 5.2) of bovine liver tissue at the ambient temperature were used in the non-linear acoustic model and thermal model to simulate the formation of the thermal lesion. The pre-treatment and post-treatment mechanical properties of bovine liver tissue are summarized in Table 5.3 and were used in the linear viscoelastic model for untreated tissue and lesion tissue respectively.

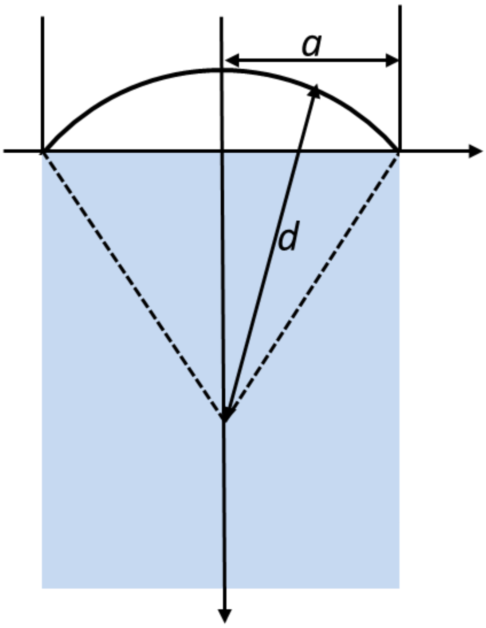

Figure 5.2 Schematic of the employed HIFU transducer. The transducer has a radius of aperture radius a = 3.2 cm, a radius of curvature d = 6.26 cm and a centre frequency of 1.1 MHz.

Table 5.1 The non-linear acoustic parameters of bovine liver tissue used in the non-linear acoustic simulation, data summarized from [113] *at 37°*C.

Non-linear acoustic parameter	Value
c_0	1592 *m/s*
ρ_0	1040 kg/m^3
α_0	0.48 dB/*cm*
ς	1
β	7.19

Table 5.2 The thermal parameters of bovine liver tissue used in the thermal map model, data summarized from [52]. *As the perfusion rate* w_b*was taken to be 0 kg/m*^{3}*/s (no heat loss due to blood flow),* C_b *and* T_a *are not required.*

Thermal parameters	Value
C_t	3510 *J/kg/K*
k	0.51 *W/m/L*
w_b	0 *kg/m*^{3}*/s*

Table 5.3 The mechanical parameters [117] *and electrical properties* [60] *of untreated and coagulated bovine liver tissue used in the linear viscoelastic model. For material densities of both tissues, refer to Table 5.1. E is the Young's modulus,* η_s *the shear viscosity,* ρ_0 *the material density,* ν *the Poisson's ratio,* ε *the relative electrical permittivity,* σ *the electrical conductivity, and* μ *the relative magnetic permeability.*

Parameter	untreated tissue	ablated tissue
E	9 kPa	72 kPa
η_s	2 $Pa \cdot s$	2 $Pa \cdot s$
ρ_0	1040 *kg/m*^{3}	1040 *kg/m*^{3}
ν	0.499	0.499
ε	52.9	46.5
σ	0.785 *S/m*	0.95 *S/m*
μ	1	1

The majority of the previous studies on the temperature and frequency-dependent electrical properties for different tissue types were conducted in the MRI community. The relative permittivity and electrical conductivity of bovine liver tissue at 400 *MHz* and 468 *MHz* has been reported when temperature increased from 35°C to 60°C in a water bath [60]. The frequency of the EM wave employed in the HIFU-EMA system was 434 *MHz* so the average values were used for the EMA simulation within the HIFU-EMA model (see Table 5.3).

Results and Discussion:

The normalized spatial distribution of ARF is the same as the heating rate map as shown in Figure 5.3a. The resulting temperature elevation at the focal point of the transducer is illustrated in Figure 5.3b. Small fluctuations in the temperature (0.1°C, peak-to-peak) were observed when zooming in on the temperature curve. This small fluctuation was associated with the 160 *Hz* amplitude modulation scheme applied on the ARF in order to induce an EMA signal. The region of the thermal lesion was determined by the thermal dose model. Figure 5.4 demonstrates the growth of the lesion region during the thermal ablation as temporal snapshots. From these snapshots, it can be seen that the thermal lesion was olive shaped, resembling the geometry of the ultrasound focus. By the end of the thermal ablation (t = 3*s*), it reached a longitudinal dimension of 8 mm and lateral dimension of 1.5 mm. In Figure 5.5a, the oscillatory displacement at the ultrasound focal point as a function of time is shown just before the onset of the thermal lesion and at the end of the thermal ablation. The oscillatory displacement was reduced as the thermal lesion is formed. This is because the lesion tissue tends to be much stiffer than the background tissue. The reader is reminded that in the simulation, the pre-treatment ultrasound attenuation was used for both untreated tissue and thermal lesion as discussed in Section 5.4. The oscillatory displacement normal to the lesion boundary at the end of the thermal ablation is plotted in vector form in Figure 5.5b.

The simulated FDC and UC received 6.26 *cm* away from the focal point of the ultrasound transducer are shown in Figure 5.6. The dimension of the thermal lesion was smaller than the EM wavelength (8 *cm*) and the radiation pattern of the scattered EM wave (Figure 5.6c-d) resembled the radiation of a Hertz dipole just like the electrically small spherical scatterers discussed in Chapter 4. The strongest FDC was observed in the backward scattering condition.

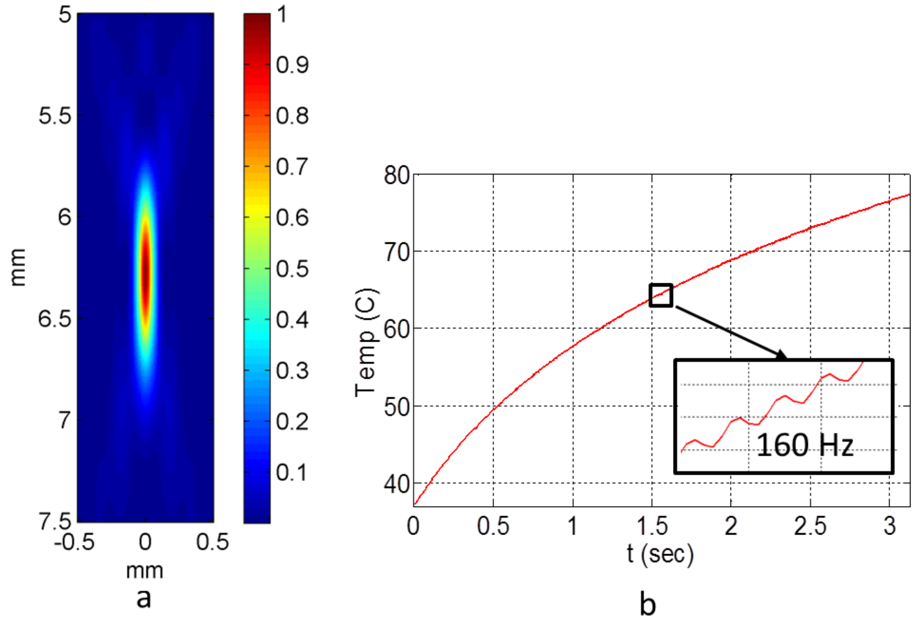

Figure 5.3 (a) The normalized spatial distribution of the ARF (the same as the normalized heating rate map) and (b) the resultant temperature elevation at the ultrasound focal point with I_{spta} *= 750 W/cm*^{2}

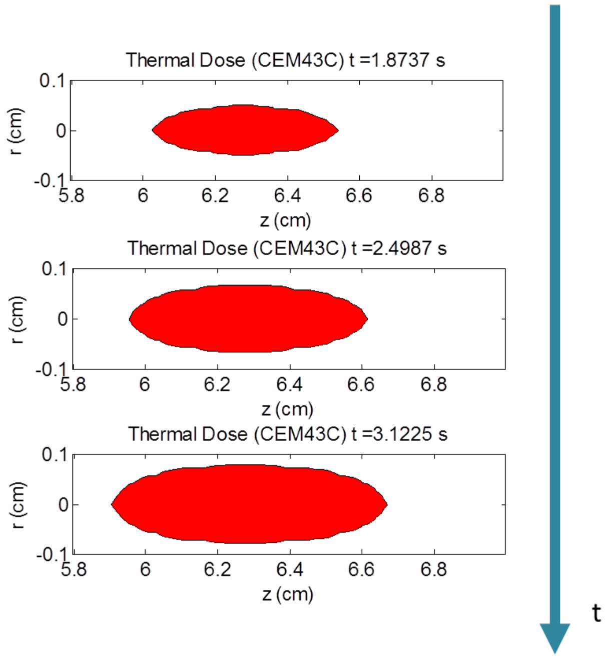

Figure 5.4 The growth of the thermal lesion as a function of HIFU exposure time shown as three snapshots at t = 1.87 s, 2.50 s and 3.12 s. The boundary of the lesion is determined using the thermal dose model

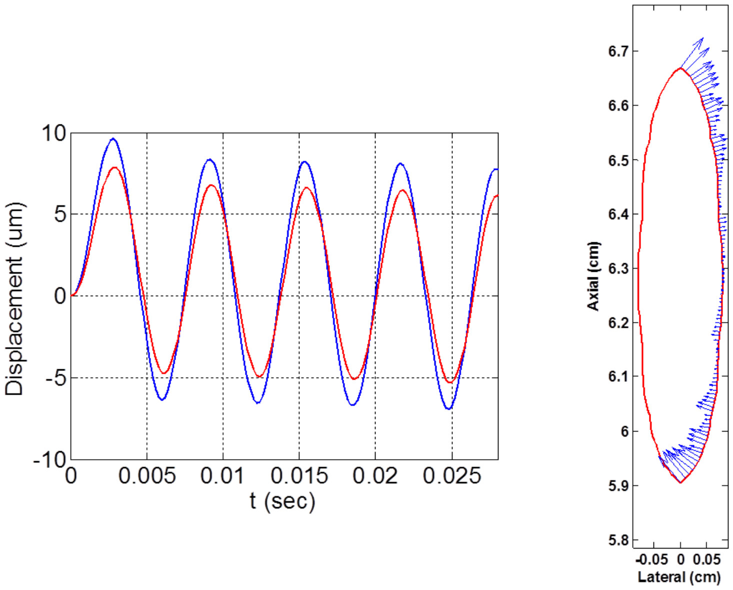

a

b

Figure 5.5 (a) The displacement of tissue at the ultrasound focal point before the lesion is formed (blue curve) and at the end of the thermal ablation (red curve); (b) the displacement field at the end of the ablation plotted as vector field along the lesion boundary

The normalized backscattered FDC and UC in the scattered EM signal, measured at the face of the ultrasound source, are plotted as a function of HIFU exposure time in Figure 5.6a. Both the FDC and the UC increased rapidly during ablation with the UC increases at about a 10% higher rate than FDC for two possible reasons. First, the thermal lesion tissue was stiffer than surrounding tissues. As the region of stiffer tissue (thermal lesion) grew larger, the induced oscillatory displacement was reduced (see Figure 5.5a) which led to slower rate of increase in the FDC. Secondly, when the lesion size grew larger than the size of the ultrasound focal volume, the ARF can only push part of the thermal lesion which further reduced the induced oscillatory motion as well as the induced Doppler effect. Figure 5.6b shows the ratio of FDC and UC

(FDC/UC) as a function of exposure time and it can be seen that it decreases by approximately 2.4 dB.

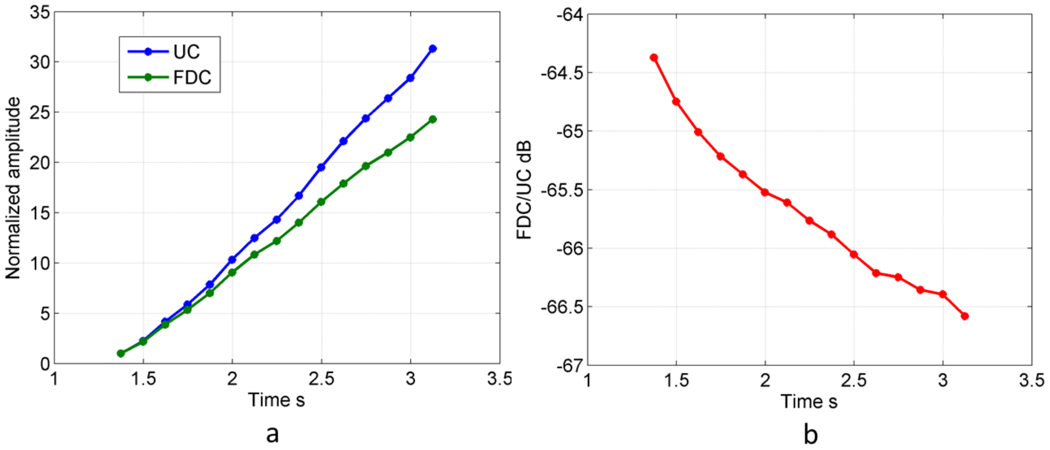

Figure 5.6 (a) The normalized backscattered FDC and UC received at the face of the ultrasound source as a function of HIFU exposure time and (b) FDC/UC as a function of HIFU exposure time

5.4 Sensitivity to mechanical properties

Motivation and method:

Previous characterisation studies of thermally coagulated liver tissue have shown that the mechanical properties of soft tissue under thermal ablation tend to vary from study to study [107, 110-116]. Such variations may be the result of different tissue types, ablation methods and measurement methods. The mechanical properties of soft tissue change as a function of temperature or accumulated thermal dose [117] [118], the exact underlying mechanism of which is still in debate. For simplicity, the employed HIFU-EMA model in this study assigns constant values of mechanical properties to lesion tissue, instead of allowing them to vary with temperature or accumulated thermal dose. Therefore it is necessary to test the sensitivity of the EMA signals to the reported variation in mechanical properties.

The attenuation coefficient at 1 MHz α_0 of bovine liver was reported to increase from 0.48 dB$/cm$ to 0.94 dB$/cm$ when thermally denatured [113]. The acoustic model employed here assumes that the acoustic waves propagate through layers of different materials without reflection. Therefore it can only cope with layered material and does not have the capability to simulate the acoustic scattering from a thermal lesion as the thermal lesion has acoustic properties (e.g. attenuation coefficient) different from the surrounding material. Hence a uniform ultrasound attenuation of 0.48 dB$/cm$

is used for both untreated tissue and lesion tissue throughout the simulation with the acoustic model. The attenuation coefficient is associated with the conversion of acoustic energy to thermal energy and as a result, BHTE which takes the converted energy as an input tends to underestimate the rate of lesion formation. To be consistent with the BHTE, the lesion tissue in the linear viscoelastic model was also assigned $\alpha_0 = 0.48$ dB/m. This led to an underestimation of the forcing function as a lesion grows. In this section the attenuation coefficient in the lesion was assumed to have a higher value of 0.96 dB/cm in the viscoelastic model in order to access the effect of different α_0.

The reported stiffness ratio between the coagulated tissue and untreated tissue is in the range of 15:1 [119] and 8:1 [120] for porcine liver, 3.6~1.4:1 for canine liver [121], and 5:1 [122] and 12:1 [118] for bovine liver. Hou and Konofagou [52] concluded that the coagulated tissue tends to be 2 to 12 times stiffer than untreated tissue and this range will be considered here. No data is available for the shear viscosity at the modulation frequency of ARF (160 *Hz*). Chen and Greenleaf [123] reported a shear viscosity of 2 Pa·s at 100 *Hz*. Shahmirzadi & Konofagou [124] reported a contrast of 8~30:1 for canine liver tissue at 0.1~10 *Hz* whilst Xie & Greenleaf [125] reported a contrast of 20~28:1 in porcine liver tissue at 100 *Hz*. Based on the above data the contrast in shear viscosity was assumed to increase up to a factor of 30.

Results and Discussion: mechanical response

The UC is directly determined by the size of the thermal lesion and the electrical contrast between the lesion tissue and untreated tissue. It does not vary with changes in mechanical properties and therefore in this section the discussion focused on the FDC. Figure 5.7 shows the effect of increasing the attenuation coefficient of lesion tissue to 0.94 dB*/cm* in the linear viscoelastic model. Before the lesion was formed (Figure 5.7a), no difference between the two cases was observed in the oscillatory displacements of tissue as a function of time. After the onset of the thermal lesion (Figure 5.7b), the greater ARF experienced by the thermal lesion due to the higher attenuation coefficient resulted in a greater amplitude of oscillatory displacement. As a result, the FDC in the scattered EM signal grew at about a 10% greater rate (Figure 5.7c). Figure 5.7d shows the ratio of the FDC to the UC for the case where attenuation is altered or uniform. Recall the ratio dropped by approximately 2.1 dB previously, accounting for the extra attenuation the FDC now increases at the same rate as the UC and the change in ratio now is less than 0.5 dB. In a real world scenario, the attenuation coefficient is likely to change gradually with deposited thermal energy. This might lead to a more complicated curve of the FDC/UC. Therefore the simulation suggests that the Doppler effect (estimated by FDC/UC) in the scattered EM signal is unlikely to be a good indicator of the size of the induced thermal lesion.

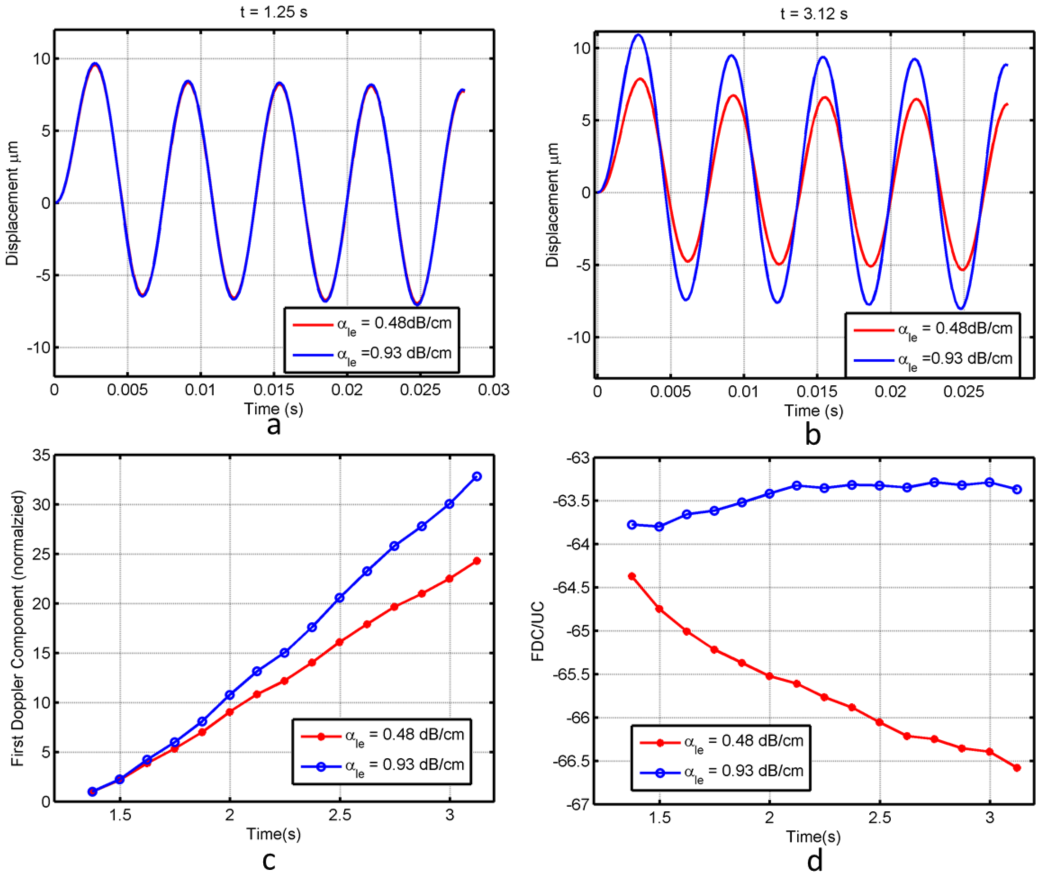

Figure 5.7 The sensitivity of the FDC to the attenuation coefficient (α_{le}*) of thermal lesion tissue. (a) shows the oscillatory displacement at the ultrasound focal point before the lesion is formed (b) compares the displacement at the ultrasound focal point towards the end of the thermal therapy; (c) compares the resultant FDC with different attenuation coefficient assigned to the lesion tissue in the linear-viscoelastic model ;(d) shows the resultant change in the FDC/UC; the subscript le denotes the property for the lesion tissue.*

In Figure 5.8 the stiffness ratio between the lesion and untreated tissue was varied from 4 to 12. The root-mean-square (RMS) differences between the curves of different stiffness ratio were negligible (1.67%). This indicates that the oscillatory displacement and the FDC were not linearly related to the stiffness of the lesion tissue. That is, once the lesion was stiff enough, the effect of further increase in stiffness was minimal.

Figure 5.9 demonstrates the sensitivity of the FDC to the shear viscosity ratio. When it was varied from 1 to 30, the RMS difference between different curves of shear viscosity ratio was again very small (0.65%). As has been mentioned at the start of this section, the values of stiffness ratio and shear viscosity ratio between the lesion tissue and untreated tissue reported in different studies tend to spread in certain ranges. Based on the observations made on Figure 5.8 and Figure 5.9, it is concluded that the FDC is not sensitive to the variations in the stiffness or viscosity of the tissue over the ranges reported in the literature. Therefore the model of EMA imaging will not be significantly affected by the uncertainties in the data of the mechanical properties of the tissue.

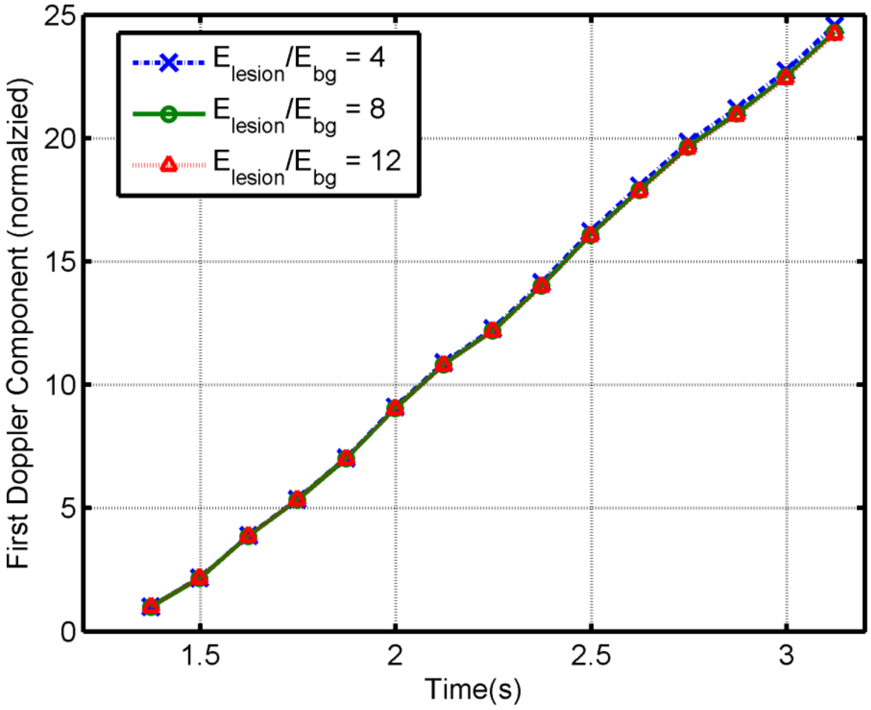

Figure 5.8 The changes in the FDC when the stiffness ratio between the lesion tissue and untreated tissue is varied from 4 to 12.

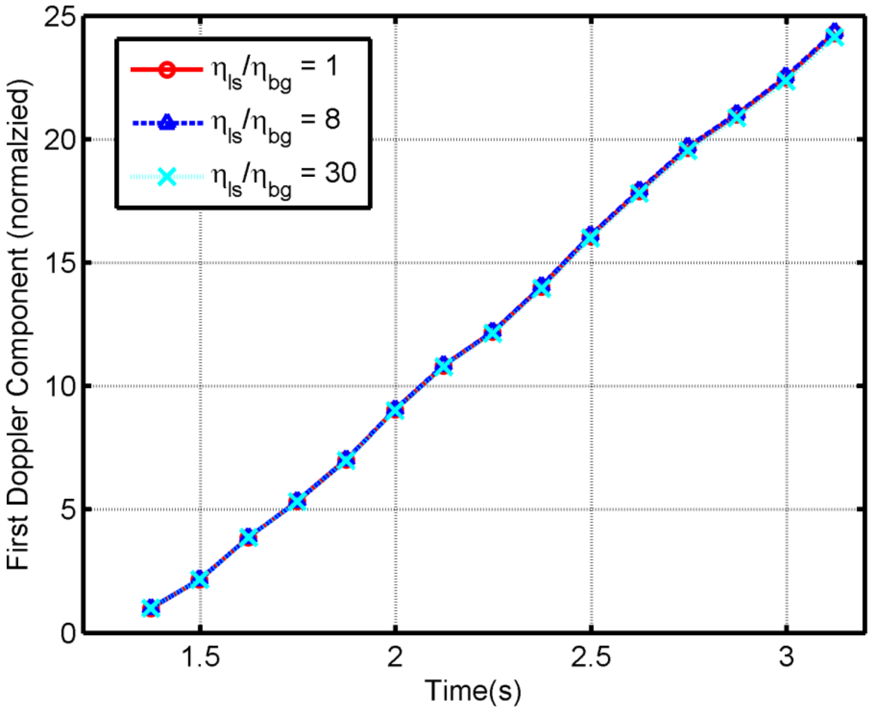

Figure 5.9 The changes in the FDC when the shear viscosity ratio between the lesion tissue and untreated tissue is varied from 1 to 30

5.5 Impact of varying ultrasound intensity

Motivation and Method:

The intensity of ultrasound affects both the heating rate (and hence the rate of thermal lesion formation) and the ARF because for EMA monitoring and HIFU the same transducer is employed. Because high amplitude ultrasound is employed, non-linear effects results in higher absorption than would be expected from linear models. This needs to be considered for both heating and ARF. First the effect of increasing the ultrasound intensity on the FDC and the UC was considered. Then the simulated FDC and UC were compared to the measured lesion volume [58].

The ultrasound transducer was modelled as described earlier: an active diameter of 64 *mm*, focal distance of 62.6 *mm*, and operating at 1.1 *MHz*, however in this case it also had a 20 *mm* hole in the centre to allow for an imaging or monitoring transducer. This geometry matched a commercially available transducer (H102d, Sonic Concepts, Woodinwill, WA) and was done in order to compare with experimental data. The ultrasound propagated directly into the liver tissue. The relevant acoustic properties are given in Table 5.1, thermal parameters in Table 5.2, mechanical and electrical properties in Table 5.3.

In the first part of this section, three ultrasound intensity levels were tested (I_{spta} = 589 W/cm^2, 750 W/cm, and 915 W/cm^2). In the second part, the HIFU-EMA simulation was compared to an experimental investigation in [58] [126] in which the transducer was employed to create thermal lesions in ex vivo bovine liver tissue at a depth of 2 *cm* under the liver tissue surface. The volume of the created lesions was measured by manually slicing through the lesion as functions of ultrasound intensity and HIFU exposure time. The corresponding HIFU-EMA simulation was conducted using the same set-up as in previous investigations and the ultrasound power level was also tuned so that the simulated I_{spta} agreed with the de-rated ultrasound intensity in the experimental investigation.

Results and Discussion:

Figure 5.10 presents the simulated FDC (left axis) and lesion volume (right axis) as functions of the HIFU exposure time. It can be seen that higher ultrasound intensity has led to earlier onset and more rapid growth of the induced thermal lesions: at I_{spta} = 915 W/cm^2 the lesion started to form at approximately t = 1*s* and grows at a rate of 5 mm^3/s whilst at I_{spta} = 589 W/cm^2 the lesion starts to form at t = 1.85*s* and grows at a rate of 3.4 mm^3/s. For each of the ultrasound intensities, the rate of increase of the FDC was slightly smaller than that of the lesion volume.

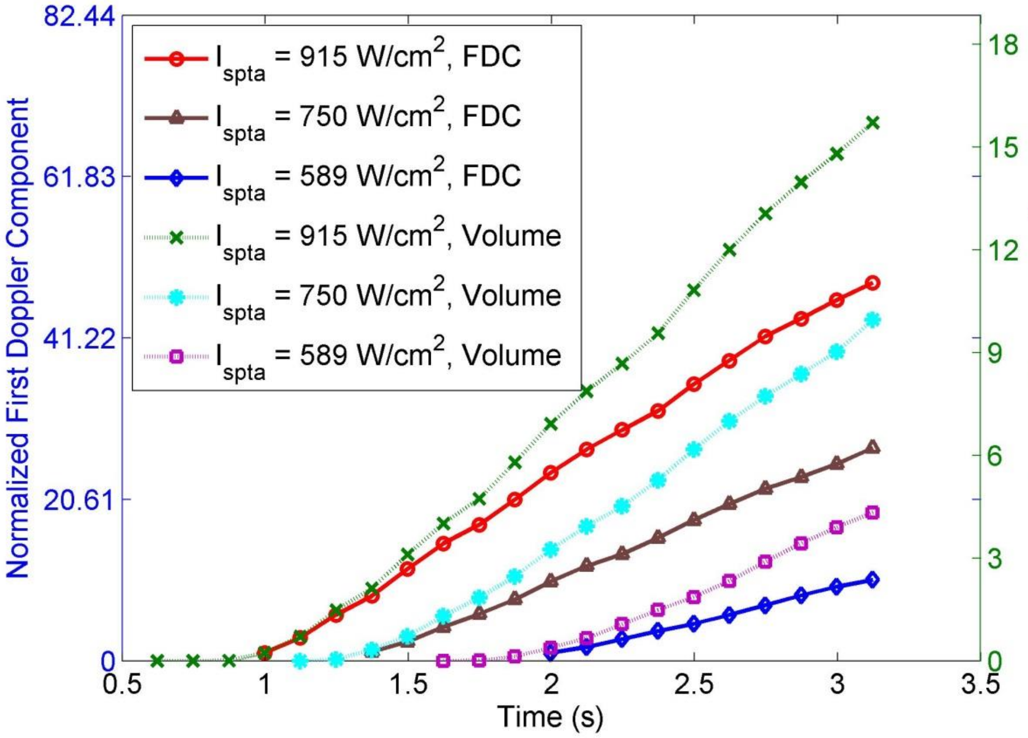

Figure 5.10 The impact of increasing ultrasound intensities on the FDC and simulated lesion volume by the HIFU model. The scattered EM signal is recorded 6.26 cm away from the ultrasound focal point at the backward scattering position

Figure 5.11 compares the simulated volumes of thermal lesions formed at different ultrasound intensities to the experimental investigation in [127]. The large error bars in the measured volume were attributed to the difficulty in obtaining accurate measurements of lesion volume [127]. The simulation estimated the onset of thermal lesions 0.5 seconds earlier than experimentally observed at 1445 W/cm^2 and 0.2 seconds earlier at 1135 W/cm^2 respectively. Note that I_{spta}= 1445 W/cm^2 and 1135 W/cm^2 were de-rated from I_{spta}= 1910 W/cm^2 and 1500 W/cm^2 in Figure 7 of [127] using the recommended de-rating factor of 87% (for ultrasound amplitude). The HIFU-EMA model also significantly underestimated the rate of lesion formation. By the end of the 5 seconds HIFU exposure time, the HIFU-EMA simulated lesion volumes were only approximately 40% of the measured lesion volumes for both ultrasound intensities.

Several sources of error may have contributed to the observed discrepancies between the simulated and measured lesion volumes. First, the experimental study reported more than 40% changes in the thermal conductivity and 20% in specific heat capacity in porcine liver during a heating-cooling cycle($20°C$-$90°C$-$20°C$) facilitated by a water bath [128]. The HIFU-EMA model employed in this study neglects the temperature dependence of thermal parameters of tissue under thermal ablation. Second, as has been discussed in Section 5.4, the thermal model used in this investigation tends to underestimate the thermal energy deposition as it employs the pre-treatment ultrasound attenuation throughout the simulation, which leads to underestimated lesion volume. Lastly, the thermal dose model (CEM43$°C$) used for deciding the volume of the thermal lesion are only intended to be used within a few degrees of $43°\boldsymbol{C}$. Its application in modelling thermal lesion formation during HIFU exposure has not been verified. Despite the shortcomings of the HIFU model, the comparison with experimental results is made to alert the reader that, as the EMA signal is highly correlated with the lesion volume as shown in Figure 5.10, the accuracy of the predicted EMA signal by a HIFU-EMA model is constrained by the robustness of the HIFU model.

More accurate prediction of thermal lesion formation during HIFU therapy is likely to be achieved by using more advanced models and employing more accurate temperature dependent material properties. For example, heterogeneous acoustic model could be used which would allow temperature dependent attenuation to be incorporated. Such model development is non-trivial and is out of the scope of the thesis. Nevertheless, if the spatial profile of the thermal lesion during a HIFU treatment is available from experiments, it can be imported into the HIFU-EMA model to replace the simulated thermal lesion, which will yield more an accurate estimation of the FDC and the UC.

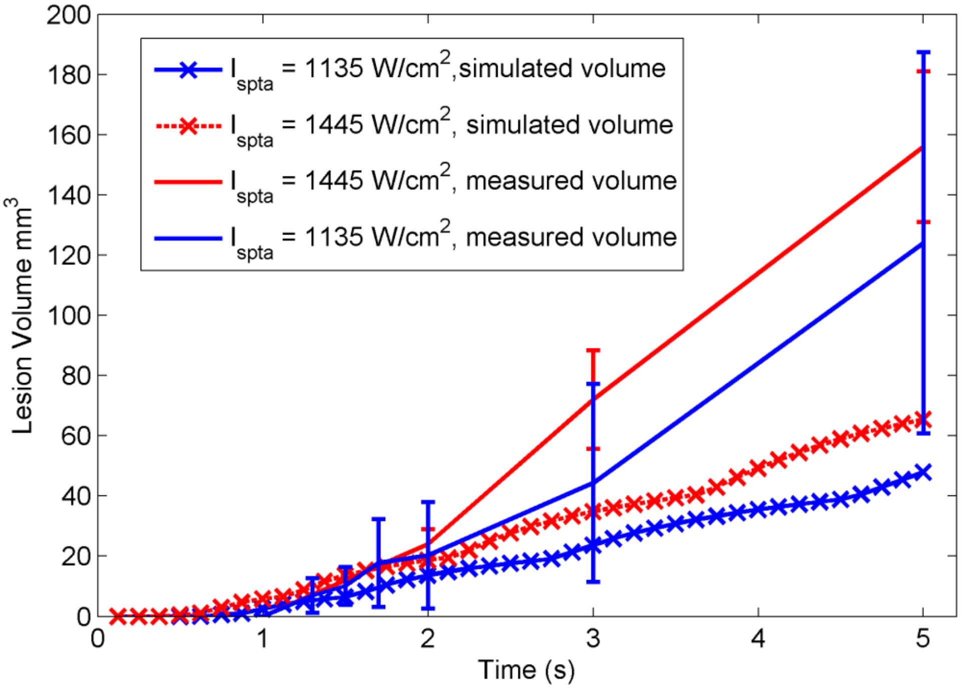

Figure 5.11 Simulated volume of thermal lesions formed at different ultrasound intensities (I_{spta}= 1445 W/cm^2 and 1135 W/cm) compared to experimental measurements described in [127].

5.6 Summary

The feasibility of using the EMA imaging to monitor thermal lesion formation during HIFU therapy was investigated using a HIFU-EMA model. HIFU is well-studied for EMA imaging as HIFU employs a high powered transducer and can deliver high amplitude signals as it is not limited by safety considerations to the same degree of diagnostic applications. The amplitude of the FDC and the UC both increased with the size of the thermal lesion. Increasing the stiffness ratio between the lesion and untreated tissue from 4 to 12 or the shear viscosity ratio from 1 to 30 had no observable effect on the FDC. Therefore the FDC is unlikely to be sensitive to variation in the stiffness and shear viscosity reported in different studies due to different methods and experimental conditions. Investigation of the sensitivity of the FDC to the ultrasound attenuation suggests that the induced Doppler effect (FDC/UC) is unlikely to be a good indicator of lesion size. Higher ultrasound intensity led to more rapid formation and growth of thermal lesion as functions of HIFU exposure time therefore greater FDC was observed as a result of increased scattered EM signal level. It is noteworthy that increasing the ultrasound intensities above a certain threshold may induce cavitation effects, which was not modelled with the current HIFU-EMA model.

In a real world scenario, the EM scattering from ambient scatterers will also contribute to the UC, making the frequency shift in the EMA signal difficult to detect, as has been discussed in Section 4.5. This suggests that the radiation pattern of the EM antenna will play an important role in the EMA system. An advantage in HIFU is that changes in properties are expected at the ultrasound focus, and an antenna system could be designed with high directivity located at the ultrasound focal point, the EM illumination will then be focused on the induced HIFU lesion and the effect of undesired EM scatterers in the ambient environment will be reduced. However, to obtain an EM focus comparable to the acoustic focus in size, the antenna will in inappropriately large (3-5 meters).

Chapter 6 Conclusions and Future Work

6.1 Conclusions

The thesis's major conclusion is that the applications of EMA imaging to medical field will be very challenging due to the small signal to noise ratio predicted by the computational model of EMA imaging developed in this thesis. The model for EMA imaging incorporates three physical phenomena: acoustic propagation in tissue, viscoelastic deformation with ARF stimulation and the Doppler scattering of EM waves from vibrating scatterers. The model was then applied to two medical applications: first the breast tumour detection and the second the monitoring of the thermal ablation of soft tissue using HIFU. In the latter case, a HIFU model to simulate the thermal lesion formation process was also added into the model.

Chapter 2 derived an approximate analytical solution for the EM scattering from an oscillating electrically small dielectric sphere using a quasi-stationary approach. This was used as a benchmark solution to validate the computational model developed in Chapter 3. The EM wave scattered by a harmonically vibrating object has a discrete spectrum with an UC, at the frequency of the incident EM wave, and a FDC separated by the frequency of the vibration of the object from the UC. In a clinical scenario, the amplitude of the ARF induced vibration will be small relative to the wavelength of the EM wave (10s μm versus 10s cm) which makes the numerical evaluation of the Doppler shift computationally unaffordable. To overcome this problem, the SBC was applied to the boundary of the vibrating object and allowed the FDC and the UC to be evaluated in two separate simulations of EM propagation and scattering. The expression of the SBC in the frequency domain was developed and incorporated into frequency domain FEM simulations. The comparison of the SBC-FEM simulated results and analytical results [29] for the EM scattering by vibrating cylinders has demonstrated that the simulation approach developed in this thesis was robust and showed potential for more complex problems in 3D where analytical solutions do not exist. The complete EMA model for medical imaging was presented in Chapter 3. To the best of the author's knowledge, this is the first complete EMA model capable of accounting for the key physical processes in 3D space which can be applied to more realistic clinical problems. Prior models were limited to tissue stimulation with unfocused ultrasound [40] or external compression [44] and simulations were conducted in 2D space [40] [42] [44].

Chapter 4 investigated the feasibility of EMA imaging to diagnose breast cancer by detecting brest tumours. A breast tumour was modelled as a spherical inclusion in an infinite homogeneous background medium which was consistent with prior simulation study of ARFI for breast tumour detection [74] [87]. The amplitude of the UC was found to be many orders greater than that of the FDC therefore can be used as a measure of the strength of the scattered EM signal whilst the FDC relative to the UC can be used to represent the magnitude of induced Doppler effect. Variations of the mechanical properties of the healthy breast tissue and tumour tissue in the clinically feasible range had led to up to 50% change in the amplitude of the FDC whilst the UC was unaffected. Variations in electrical properties produced less than a 1 dB change in the ratio of the FDC and the UC. The FDC was found to be much smaller than the UC (-68 dB to -90 dB, Figure 4.14). Detecting such a small signal frequency shift will be very challenging in practice given the small FDC/UC, and requires a sensitive frequency demodulation circuit. The previously proposed demodulation circuit for EMA [39] was based on a phased locked loop circuit which uses a voltage controlled crystal oscillator (CVSS-940, Crystek Corporation, Fort Myers, Florida, United States) which has a phase noise of -80 dB*c* at a 100 *Hz* offset. The phase noise of CVSS-940 suggests that detecting the FDC that is 68 dB smaller than UC seems to be possible. However the 68 dB is an optimistic estimation and it does not consider the effect of other non-vibrating EM scatterers in the view of the EM antennas (see Section 4.5). In realistic situations, strong and large EM scatterers such as the interface between air and soft tissue may increase the amplitude of UC significantly and make the frequency demodulation even more challenging. Alternatively, digital filters, e.g., matched filters, may be used to demodulate the frequency shift. However implementing digital matched filters for EMA requires the EM signal to be sampled at a high sampling frequency (10s *GHz*) to avoid the EM waveform distortion and a high resolution (>16 Bits) analogue to digital converter to provide sufficient dynamic range. The conclusion of this chapter was that the tumour detection with EMA imaging requires the development of an EM signal system that is able to discriminate the FDC from the UC that is 90 dB greater. The author believes that designing an EM system that meets the SNR requirements of the EMA imaging is possible, although it is likely to be challenging, as it requires the state of art electronic components and signal processing techniques.

For the HIFU application the ablation of tissue results in an increase in tissue stiffness, which may be detected by EM. Previous groups have used acoustic radiation force in order to detect changes in stiffness [81] [52]. The EMA imaging is not only sensitive to tissue dynamics, moreover, it also can exploit the electrical contrast between HIFU lesion and unabated tissue. A widely accepted non-linear acoustic propagation model and a thermal model [110] were added into the EMA model for HIFU scenarios. Simulations were conducted with realistic properties of liver tissue. The results showed that the FDC was most sensitive to the initial stage of the stiffening of the lesion tissue after which further increases in the stiffness ratio between lesion and untreated tissue had minimal effect. The same was found for shear viscosity. Using the ultrasound attenuation of untreated tissue throughout the simulation led to a descending trend in frequency shift (FDC/UC) as a function of ablation time. However this descending trend was replaced by a flat curve if a more realistic attenuation coefficient was assumed for lesion tissue in the linear viscoelastic model.

This showed that the frequency shift in the scattered EM signal was unlikely to be a good indicator of lesion size. The higher ultrasound intensity of the acoustic beam caused the thermal lesion to form earlier and grew more rapidly. Due to the lack of correlation between the frequency shift and lesion volume, the EMA is unlikely to be ideal candidate for HIFU monitoring as an independent method. However, the ARF stimulation of tissue in EMA is very similar to other imaging methods such as HMI, ARFI, and SWET (Section 1.2.5). Therefore EMA imaging may be a valuable piece of technology to be integrated into other systems because of its ability to detect electrical contrasts.

The overarching conclusion from this work is that the signal-to-noise ratio for EMA imaging is so low as to make applications to the medical field challenging. Recalling that the inclusions are from 0.5 mm to 10 mm in size and are moving in a μm scale whilst the EM waves have wavelengths of 10s cm, it is not surprising that the medical application of EMA is challenging. However, with the advent of EM coil design with better directivity and improved signal processing the SNR barrier is not so large that it cannot be overcome.

6.2 Future work

The EMA model developed in this thesis made a number of simplifying assumptions. The analysis in Chapter 4 for breast tumour detection and Chapter 5 assumed that the inclusion (either tumour or thermal lesion) was embedded in an infinite homogeneous background medium. In reality tissue is heterogeneous and finite in extend. The heterogeneity will affect the acoustic propagation, elastic deformation and the EM scattering. The effects of other EM reflectors such as blood vessels, lungs and bones in the body were also not considered. The developed EMA model has the capability to include these EM scatterers. It is speculated that the presence of non-vibrating EM scatterers will contribute additional energy to the UC and hence increase the difficulty to detect the frequency shift beyond what was reported here. This problem may be overcome by replacing the plane EM wave source assumed in the thesis with EM transmitting and receiving antennas with high directivity. High directivity reduces EM illumination on tissues that is not stimulated by ARF hence reduce the effect of EM scatterers. The EM antenna that can achieve a small (mm) focus at a close distance (cm) is likely to have a large size (meters) which makes it inappropriate to be deployed with an EMA imaging system. Some researchers are attempting to achieve sub-wavelength antenna with enhanced directivity using meta-material [129]. However this is unlikely to be achieved in a near future. Alternatively, targeted contrast agents that can bind on specific tissue type (e.g., cancer) [130] and modify the local dielectric properties [131] could be used to increase the electrical contrast so that the EM scattering by the targeted tissue (e.g., a tumour) is increased relative to other undesired EM scatterers.

Another important aspect of the work is the optimisation of EMA parameters using the developed EMA model. For example, EMA parameters such as the frequency of the EM signal, frequency of the ultrasound and frequency of the ARF amplitude-modulation in this thesis were selected to be consistent with the experimental system under development. Increasing the frequency of the amplitude-modulation of the ARF f_{arf} is likely to alter the amplitude of tissue oscillation (due to the frequency dependence of shear wave attenuation, see Equation 3.18), which will affect the amplitude of the FDC relative to the UC. On the other hand, increasing f_{arf} separates the FDC further from UC in the spectrum, which relaxes the phase noise requirement of the voltage controlled oscillator in the frequency shift detection system. Increasing the frequency of the EM wave f_{em} increases its propagation constant which leads to increased FDC. But higher f_{em} reduces its penetration depth to soft tissue which limits the application of EMA imaging in deeper body positions. There will also be issues with regulation of the EM spectrum for various applications. With a wide search domain it may be possible to find an optimal choice of f_{arf} and f_{em} by simulations with the developed EMA model.

There are several different possible configurations for EMA imaging. EMA can be deployed with a clinical ultrasound scanner. Modern scanners employ a phased array ultrasound transducer which allows the focus of ARF to be scanned in the plane of a B-mode image. This produces an EMA image that is automatically registered to the B-mode ultrasound image with additional information about the tissue's mechanical and electrical properties. The challenge will be developing a sufficiently sensitive frequency shift detection system to demodulate the scattered EM signal. Another possible option is to integrate EMA imaging into a microwave imaging system, for example the radar based microwave imaging system [11] [14]. The system uses ultra-wide band microwave up to 10 *GHz* and has the capability to steer its microwave focal point with the ultrasound focus. The high microwave frequency helps improves the detectability of the FDC whilst the electronically steerable microwave focus reduces the energy contribution to the UC by the ambient undesired EM scatterers. The induced Doppler effect is small and is unlikely to affect the formation of microwave image. Therefore automatically registered microwave and EMA images may be produced with the latter reflecting the mechanical properties of the underlying tissue.

Bibliography

[1] Momna Hejmadi, *Introduction to Cancer Biology*, 1st ed. Cambridge, UK: Cambridge University Press, 2010.

[2] (2015, February) National Cancer Insititute. [Online]. http://www.cancer.gov/cancertopics/what-is-cancer#related-diseases

[3] International Agency for Research on Cancer, WHO, Cancer Research UK, "World Cancer Factsheet," 2014.

[4] (2015, April) CancerresearchUK. [Online]. http://www.cancerresearchuk.org/about-cancer/cancer-symptoms/why-is-early-diagnosis-important

[5] Carl R. Jensen et al., "Spatiotemporal Monitoirng of High-Intensity Focused Therapy with Passive Acoustic Mapping," *Radiology*, vol. 262, no. 1, pp. 252-261, January 2012.

[6] Nadine Barrie Smith and Andrew Webb, *Introduction to Medical Imaging: Physics, Engineering and Clinical Applications*. New York: Cambridge University Press, 2011.

[7] F. Bloch, "Nuclear Induction," *Physical Review*, vol. 70, pp. 460-474, 1946.

[8] E.M Purcell, "Resonance Absorption by Nuclear Magnetic Moments in a Solid," *Physical Review*, vol. 69, pp. 37-38, 1946.

[9] Mark Cohe. brainmapping. [Online]. http://www.brainmapping.org/MarkCohen/Papers/SpeedLimit.html

[10] William R. Hendee and Russell Ritenour, *Medical imaging physics*, 4th ed.: John Wiley & Sons, Inc, 2003.

[11] Elise C. Fear, "Microwave Imaging of the Breast," *Technology in Cancer Research and Treatment*, vol. 4, no. 1, pp. 69-82, 2005.

[12] Serguei Semenov, "Microwave tomography: review of the progress towards clinical applications," *Philoscophical transactions*, vol. 367, no. 1900, pp.

3021-3042, 2009.

[13] Kenneth I. Carr, "Microwave Radiometry: Its importance to the detection of cancer," *IEEE Transactions on microwave theory and technoques*, vol. 37, no. 12, pp. 1862-1868, 1989.

[14] Susan C.Hagness, "Two-Dimensional FDTD Analysis of a Pulsed Microwave Confocal System for Breast Cancer Detection: Fixed-Focus and Antenna-Array Sensors," *IEEE transactions on Biomedical Engineering*, vol. 45, no. 12, pp. 1470-1479, 1998.

[15] W. C. Chew and Y M Wang, "Reconstruction of Two-Dimensional Permittivity Distribution Using the Distorted Born Iterative Method," *IEEE transactions on medical imaging* , vol. 9, no. 2, pp. 218-225, 1990.

[16] David W. Winters, Barry D Van Veen, and Hagness C Susan, "A Sqarisity Regularization Approach to the Electromagnetic Inverse Scattering Problem," *IEEE transactions on antennas and propagation*, vol. 58, no. 1, pp. 145-154, 2010.

[17] Zhong Qing and Qing Huo Liu, "Three-Dimensional Nonlinear Image Reconstruction for Microwave Biomedical Imaging," *IEEE transactions on biomedical engineering*, vol. 51, no. 3, pp. 544-548, 2004.

[18] Cloin Gilmore, Amer Zakaria, Stephen Pistorius, and Joe LoVetri, "Microwave Imaging of Human Forearms: Pilot Study and Image Enhancement," *Internaltional Journal of Biomedical Imaging*, vol. 2013, no. 1-17, 2013.

[19] K.L.Carr, P Cevasco, P Dunlea, and J Shaeffer, "Radiometric Sensing: An Adjuvant to Mammography to Determine Breast Biopsy," in *IEEE international microwave symposium Digest*, 2000.

[20] Paul M Meaney et al., "Micrwowve imaging for neoadjuvant chemotherapy monitoring: initial clinical experience," *Breast Cancer Research*, vol. 15, pp. 1-16, 2013.

[21] Armen Savazyan et al., "An overview of elastography-an emerging branch of medical imaging," *Curr Med Imaging Rev*, vol. 7, no. 4, pp. 255-282, Nov 2011.

[22] Kathryn Nightingale, Rex Bentley, and Gregg Trahey, "Observations of Tissue Response to Acoutic Radiation Force: Opportunities of Imaging," *Ultrasound Imaging*, vol. 24, pp. 129-138, 2002.

[23] Caroline Maleke, "In Vivo Detection and Thermal Treatment Monitoring of Breast Tumors Using Harmonic Motion Imaiging(HMI)," 2010.

[24] Armen Sarvazyan, Oleg V Rudenko, Scott D Swanson, J Brian Fowlkes, and Stanislav Y Emelianov, "Shear wave elsticity imaging: a new ultrasonic technology of medical diagnostics," *Ultrasound in Medicine and Biology*, vol. 24, no. 9, pp. 1419-1435, 1998.

[25] Jeremy Bercoff, Mickael Tanter, and Mathias Fink, "Supersonic Shear Imaging: A New Technique for Soft Tissue Elasticity Mappling," *IEEE Transactions on Ultrasounics, Ferroelectrics and Frequency Control*, vol. 51, no. 4, pp. 396-409, 2004.

[26] Ralph Sinkus et al., "Viscoelastic shear properties of in vivo breast lesions measured by MR elastography," *Magnetic Resonance Imaging*, vol. 23, pp. 159-165, 2005.

[27] Emil.Wolf Max.Born and Emil Wolf, *Principle of Optics*, 7th ed. Cambridge, UK: Cabridege University Press, 1975.

[28] G Benedek and T Greytak, "Brillouin Scattering in Liquids," *Proceedings of the IEEE*, pp. 1633-1629, 1965.

[29] Kamal Sarabandi and Daniel E Lawrence, "Acoustic and Electromagnetic Wave Interaction: Analytical Formulation for Acousto-Electromagnetic Scattering Behavior of a Dielectric Cylinder," *IEEE Transactions on Antenna and Propagation*, vol. 49, no. 10, pp. 1382-1392, 2001.

[30] Gerhard Peters, "History of RASS and Its Use for Turbulence Measurement," *IEEE*, pp. 1183-1185, 2000.

[31] Max E North and Allen M Peterson, "RASS, A Remote Sensing System for Measuring Low-Level Temperature Profiles," *Bulletin of the American Meteorological Society*, vol. 54, no. 9, pp. 912-918, 1973.

[32] Wayne M. Angevine, "Radio Acoustic Sounding System (RASS) Applications and Limitations," *Proceedings of IEEE*, pp. 1180-1182, 2000.

[33] Pete D Theobald, Stephen P Robinson, Roy C Preston, Paul A Lepper, and Yuebing Wang, "Technique for the Calibration of Hydrophones in the Frequency Range 10-600 kHz using a Heterodyne Interferometer and an Acoustically Compliant Membrane," *Journal of Acoustical Society of America*, pp. 3110-3116, 2005.

[34] David R. Bacon, "Primary Calibration of Ultrasounic Hydrophones Using Optical Interferometry," *IEEE Transactions on Ultrasonic Hydrophones Using Optical Interferometry*, vol. 35, no. 2, pp. 152-161, 1988.

[35] Waymond R Scott and James S Martin, "Experimental Investigation of the Acousto-Electromagnetic Sensor for Locating Land Mines," *Proceedings of SPIE*, vol. 3710, 1999.

[36] James S Martin and Scott R Waymond, "A Hybrid Acoustic/Electromagnetic Technique for Locating Land Mines," in *Geoscience and Remote Sensing Symposium Proceedings*, Seattle, WA, 1998, pp. 216-218.

[37] Waymond R Scott and James S Martin, "An Experimental Model of a Acousto-Electromagnetic Sensor for Detecting Land Mine," in *Proceedings of the 1998 IEEE Antennas and Propagation Symposium*, Atlanta, 1998.

[38] Robin O. Cleveland, Ning Zhang, and David Edwards, "Electromagnetic-Acoustic(EMA) imaging of stiffness and dielectric properties in gels," in *Proceedings of Meetings on Acoustics*, Montreal, Canada, 2013.

[39] Zein A.Khan, "Medical Imaging Using the Acousto-Electromagnetic Technique," Oxford University, Oxford UK, Thesis 2011.

[40] Amelia M. Buerkle and Kamal Sarabandi, "Analysis of Acousto-Electromagnetic Wave Interaction Using Sheet Boundary Conditions and the Finite Difference Time Domain Method," *IEEE Transactions on Antenna and Propagation*, vol. 77, no. 7, pp. 1991-1998, 2007.

[41] Daniel E.Lawrence and Kamal Sarabandi, "Electromagnetic Scattering from Vibrating Metallic Object Using Time-Varying Generaized Impedance Boundary Condtion," in *Antennas and Propagation Society International*

Symposium, Ann Arbor, 2002, pp. 782-785.

[42] Daniel E.Lawrence and Kamal Sarabandi, "Electromagnetic Scattering from Vibrating Penetrable Object Using a General Class of Time-Varying Sheet Boundary Condition," *IEEE Transactions on Antenna and Propagation*, vol. 54, no. 7, pp. 2054-2061, 2006.

[43] Daniel E Lawrence and Kamal Sarabandi, "Acoustic and Electromagnetic Wave Interaction: Estimation of Doppler Spectrum From an Acoustically Vibrated Metallic Circular Cylinder," *IEEE Transactions on Antennas and Propagation*, pp. 1499-1507, 2003.

[44] Min Zhao et al., "Numercial Study of Microwave Scattering in Breast Tissue via Coupled Dielectric and Elastic Contrast," *IEEE Antennas and Wireless Propagation Letters*, vol. 2008, pp. 247-250, Aug 2008.

[45] Robert A. Smith, Durado Brooks, Vilma Cokkinides, Debbie Saslow, and Otis W Brawley, "Cancer Screening in the United States, 2013 A review of Current American Cancer Society Guidelines, Current Issues in Cancer Screening, and New Guideance on Cervical Cancer Screening and Lung Cancer Screening," *Cancer J Clin*, vol. 63, no. 2, pp. 87-105, 2013.

[46] Carol DeSantis, Rebecca Siegel, and Ahmedin Jemal, "Breast Cancer Facts & Figures 2013-2014," American Cancer Society, Atlanta, research document 2014.

[47] Janet E. Joy, Edward E Pengiet, and Diana B Petitti, *Saving Women's Lives: Strategies for improving breast cancer detection and diagnosis*. Washington, DC: National Academies Press, 2005.

[48] Karla Kerlikowske et al., "Comparative effectiveness of digital versus film-screen mammography in community practice in the United States," *Annals of Internal Medicine*, vol. 155, no. 8, pp. 493-510, 2011.

[49] James F. Freenleaf, Mostafa Fatemi, and Michael Insana, "Selected Methods for Imaging Elastic Properties of Biological Tissues," *Annu. Rev. Biomed. Eng*, vol. 5, pp. 57-78, 2003.

[50] Z.Zhao and F Wu, "Minimally-invasive thermal ablation of early-stage breast cancer: a systemic review," *European Journal of Surgical Oncology*, vol. 36,

pp. 1149-1155, 2010.

[51] Theodore J. Dubinsky, Carlos Cuevas, Manjiri K Dighe, Orpheus Kolokythas, and Joo Ha Hwang, "High-intensity Focused Ultrasound: Current Potential and Oncologic Applications," *Ultrasound Imaging*, vol. 190, pp. 119-199, 2008.

[52] Gary Y. Hou, "Performance Assessment of HIFU Lesion Detection By Harmonic Motion Imaging For Focused Ultrasound(JMIFU): A 3-D Finite-Element-Based Framework with Experimental Validation," *Ultrasound in Medicine and Biology*, vol. 37, pp. 2013-2027, 2011.

[53] Ernesto R. Cordeiro et al., "High-intensity focused ultrasound (HIFU) for definitive treatment of prostate cancer," *BJU international*, vol. 110, pp. 1228-1242, 2012.

[54] David Schlesinger et al., "MR-guided focused ultrasound surgery, present and future," *Medical Physics*, vol. 40, no. 8, pp. 1-30, 2013.

[55] Kullervo Hynynen et al., "MR Imaing-guided focused ultrasound surfery of fibroadenomas in the breast: a feasibility Study," *Radiology*, vol. 219, pp. 176-185, 2001.

[56] Mathieu Pernot, Mickael Tanter, Jeremy Bercoff, Kendall R Waters, and Mathias Fink, "Mathieu Pernot," *Temperature Estimation Using Ultrasonic Spatial Compound Imaging*, vol. 51, no. 5, pp. 606-615, 2004.

[57] Brian A. Rabkin, Vesna Zderic, and Shahram Vaezy, "Hyperecho in ultrasound images of HIFU therapy ," *Ultrasound in Medicine and Biology*, vol. 31, no. 7, pp. 947-956, 2005.

[58] Sacha Nandlall, Edward Jackson, and Constantin-C Coussios, "Real-Time Passive Acoustic Monitoring of HIFU-Induced Tissue Damage," *Ultrasound in Medicien and Biology*, vol. 37, no. 6, pp. 922-934, 2011.

[59] Huizhong Cui and Xinmai Yang, "Real-time monitoring of high-intensity focused ultrasound ablations with photoacoustic technique: an in vitro study," *Medical physics*, vol. 38, pp. 5345-5350, 2011.

[60] Fanrui FU, Sherman Xuegang Xin, and Wufan Chen, "Temperature and frequency dependant dielectric properties of biological tissues within the

temperature and frequency ranges typically used for magnetic resonance imaging -guided focused ultrasound surgery," *International Journal of Hyperthermia*, vol. 30, pp. 56-65, 2014.

[61] H.C. van de Hulst, *Light Scattering by Small Particles*. New York: John Wiley & Sons, Inc, 1957.

[62] T.Shiozawa, "Electromagnetic Scattering by a Moving Small Particle," *J.Appl.Phys*, vol. 39, pp. 2993-2997, 1968.

[63] J.Van Bladel, *Relativity and Engineering*. Berlin: Springer-Verlag, 1984.

[64] Jean G.Van Bladel, *Electromagnetic Fields*. Hoboken: John wiley & Sons, Inc., 2007.

[65] Andrew M.Steane, *Relativity made relatively easy*. Oxford: OXford University Press, 2012.

[66] Jeffery Cooper, "Scattering of Electromagnetic Fields by a Moving Boundary: The One-Dimensional Case," *IEEE Transactions on Antennas and Propagation*, vol. 28, no. 5, pp. 791-795, 1980.

[67] Dan Censor, "Theory of Doppler Effect: fact, fiction and approximation," *Radio Science*, vol. 4, pp. 1027-1040, 1984.

[68] Farhan Rana. Cornell University. [Online]. https://courses.cit.cornell.edu/ece303/

[69] Dan Censor, "Generalized Doppler effect: Coherent and incoherent spectra," *J.Acoust. Soc. Am*, vol. 83, no. 6, pp. 2012-2019, 1988.

[70] Kamal Sarabandi and Daniel E Lawrence, "Acoustic and Electromagnetic Wave Interaction: Estimation of Doppler Spectrum From an Acoustically Vibrated Metallic circular Cylinder," *IEEE transactions on antennas and propagation*, vol. 51, no. 7, pp. 1499-1507, 2003.

[71] Daniel E.Lawrence and Kamal Sarabandi, "Acoustic and Electromagnetic Wave Interaction: Analytical Formulation for Acousto-electromagnetic Scattering behavior of a Dielectric Cylinder," *IEEE transactions on Antenna and Propagation*.

[72] Xucai Chen, Karl Q Schwarz, and Kevin J Parker, "Radiation pattern of a focused transducer: A numerically convergent solution," *Journal of the Acoustical Society of America*, vol. 94, no. 5, pp. 2979-2991, 1993.

[73] Armen Sarvazyan, Oleg V Rudenko, and Wesley L Nyborg, "Biomedical applications of radiation force of ultrasound: historical roots and physical basis," *Ultrasound in Medicine and Biology*, vol. 36, no. 9, pp. 1379-1394, May 2010.

[74] Mark L. Palmeri, Amy C Sharma, Richard R Bouchard, Roger W Nightingale, and Kathryn R Nightingale, "A Finite-Element Method Model of Soft Tissue Response to Impulsive Acoustic Radiation Force," *IEEE Trans Ultrason Ferroelectr Freq Control*, vol. 52, no. 10, 2005.

[75] Samuel Calle, Jean-Pierre Remenieras, Oliver Bou Matar, Melouka Elkateb Hachemi, and Frederic Patat, "Temporal analysis of tissue displacement induced by a transient ultrasound radiation force," *Journal of Acoustic Society of America*, vol. 118, no. 5, pp. 2829-2840, 2005.

[76] Kevin J. Parker, "Ultrasounic attenuation and absorption in liver tissue," *Ultrasound in Medicine and Biology*, vol. 9, no. 4, pp. 363-369, 1983.

[77] JG. Abbott, "Rationale and derivation of MI and TI- a review ," *Ultrasound in Medicine and Biology*, vol. 25, no. 3, pp. 431-441, 1999.

[78] J.D. Achenbach, *Wave Propagation in Elastic Solids*. New York: Elsevier Science Publishers, 1999.

[79] S. Catheline et al., "Measurement of viscoelastic properties of homogeneous soft solid using transient elastography: an inverse probelm approach," *Journal of the Acoustical Society of America*, vol. 116, pp. 3734-3741, 2004.

[80] Kristen H.Lee, "Modelling shear waves through a viscoelastic medium induced by acoustic radiation force," *International journal for numerical methods in biomedical engineering*, vol. 28, pp. 678-696, 2012.

[81] Caroline Maleke, Jianwen Luo, Viktor Gamarnik, Xin L Lu, and Elisa E Konofagou, "Simulation Study of Amplitude-Modulated(AM) Harmonic Motion Imaging(HMI) for Stiffness Contrast Quantification with Experimental

Validation," *Ultrasound Imaging*, vol. 32, pp. 154-176, 2010.

[82] F.Moravec and N Letzelter, "On the Modeling of the linear viscoelastic behaviour of biological material using Comsol Multiphysics," *Applied and Computational Mechanics*, pp. 175-184, 2007.

[83] Kathryn R. Nightingale, Roger W Nightingale, Mark L Palmeri, and Gregg E Trahey, "A Finite Element Model of Remote Palpation of Breast Lesions Using Radiation Force: Factors Affecting Tissue Displacement," *Ultrasound Imaging*, vol. 22, pp. 35-54, 2000.

[84] Jeremy Bercoff, "The Role of Viscosity in the Impulse Diffraction Field of Elastic Waves Induced by the Acoustic Radiation Force," *IEEE Transactions on Ultrasonics, Ferroelectrics, and Frequency Control*, vol. 51, no. 11, pp. 1523-1536, 2004.

[85] Laurent Sandrin, Didier Cassereau, and Mathisas Fink, "The role of he coupling term in transient elastography," *J. Acoust. Soc.Am*, vol. 115, no. 1, pp. 73-83, 2004.

[86] P.G.R.Aki, *Quantitative Seismology, Theory and Methods*. SanFrancisco: Freeman, 1980.

[87] Mark L. Palmeri, Steogeb A McAleavet, Kelly L Fong, Gregg E Trahey, and Kathryn Nightingale, "Dynamic Mechanical Response of Elastic Spherical Inclusions to Impulsive Acoustic Radiation Force Excitation," *IEEE transactions on ultrasonics, Ferroelectrics and frequency control*, vol. 53, no. 11, pp. 2065-2079, 2006.

[88] Constantine A.Balanis, *Advanced Engineering Electromagnetics*, 1st ed. New York, USA: John Wiley and Sons, 1989.

[89] C.C.Coussios, C H Farny, G TER Haar, and R A Roy, "Role of acoustic cavitation in the delivery and monitoring of cancer treatment by high-intensity focused ultrasound (HIFU)," *International Journal of Hyperthermia*, vol. 23, no. 2, pp. 105-120, March 2007.

[90] Wesley L. Nyborg, "Biological effects of ultrasound : developement of safty guildlines part1 ," *Ultrasound in med & bio*, vol. 26, no. 6, pp. 911-964, April

2000.

[91] Nyborg Wesley. L, "Biological effects of ultrasound: development of safety guildlines part 2," *Ultrasound in med&bio*, vol. 27, no. 3, pp. 301-333, September 2001.

[92] "The thermal index: its strengths, weaknesses, and proposed improvements," *Jornal of ultrasound in medicine*, vol. 30, pp. 714-734, November 2011.

[93] Robert Gill, *The Physics and Technology of Diagnostic Ultrasound: A Practitioner's Guide*. Sydney, USA: High Frequency Publishing, 2012.

[94] Mark A. Anastasio and Patrick La Riviere, *Emerging Imaging Technologies in Medicine*. Boca Ration: Taylor and Francis Group, 2013.

[95] Naotoka Nitta, Nobuki Kudo, and Iwaki Akiyama, "Temperature Elevation of Biological Tissue Model Exposed by Focused Ultrasound with Acoustic Radiation Force," in *American Institute of Physics*, 2012, pp. 263-266.

[96] Yunbo Liu, Bruce Herman, Joshua Soneson, and Gerald Harris, "Thermal Safety Simulations of Transient Temperature Rise During Acoustic Radation Force-Based Ultrasound Elastography," *Ultrasound in Medicine and Biology*, vol. 40, pp. 1001-1014, 2014.

[97] Christopher M Collins and Zhangwei Wang, "Calculation of Radiofrequency Electromagnetic Fields and Their Effects in MRI of Human Subjects," *Mag Reson Med*, vol. 65, no. 5, pp. 1-27, 2011.

[98] R.Otom and H Gromat, "Specific Absorption Rate Computations With A Nodal-Based Finite Element Formulation," *Progress in electromagnetic research*, vol. 128, pp. 399-418, 2012.

[99] Loren A Zaremba, "Guidance for Industry and FDA staff: Criteria for Significant Risk Investigations of Magnetic Resonance Diagnostic Devices," Food and Drug Administration, USA, FDA guidance 2003.

[100] Jolanta Karpowicz, Maila Hietanen, and Krzysztof Gryz, "EU Directive, ICNIRP Guildlines and Polish Legislation on Electromangetic Fields," *International Journal of Occupational Safety and Ergonomics* , vol. 12, no. 2,

pp. 125-136, 2006.

[101] S. Selim Seker, "Electric Field Measurements of Different Mobile Handsets in Near Zone," *IEEE international symposium on Electromagnetic Compatibility*, vol. 1, pp. 411-414, 2003.

[102] S.Sinkus et al., "Imaging Anisotropic and Viscous Properties of Breast Tissue by Magnetic Resonance-Elastography," *Magnetic Resonance in Medicine*, vol. 53, pp. 372-387, 2005.

[103] Abbas Samani, Judit Zubovits, and Donald Plewes, "Elastic Moduli of normal and pathological human breast tissues: an inversion-technique-based investigation of 169 samples," *Physics in Medicine and Biology*, vol. 52, pp. 1565-1576, 2007.

[104] A. Srivastava, Y Verma, and P K Gupta, "Determination of Elastic Properties of Resected Human Breast Tissue Samples Using Optical Coherence Tomographic Elastography," *Strain*, vol. 47, no. 1, pp. 75-87, 2011.

[105] William T. Joines, Yang Zhang, Chenxing Li, and Randy L Jirtle, "The measured electrical properties of normal and malignant human tissues from 50 to 900 MHz," *Medical Physics*, vol. 21, pp. 547-550, 1994.

[106] Mariya Lazebnik et al., "A large-scale study of the ultrawideband microwave dielectric properties of normal breast tissue obtained from reduction surgeries," *Physics in Medicine and Biology*, vol. 52, pp. 2637-2656, 2007.

[107] T. H. Allen, H J Kyziwicki, and J E Roberts, "Density, fat, water and solids in freshly isolated tissues," *Journal of applied physiology*, vol. 14, no. 6, pp. 1005-1012, November 1959.

[108] Samuel. R. Ward and Richard L Lieber, "Density and hydration of fresh and fixed human skeletal muscle," *Journal of biomechanics*, vol. 38, pp. 2317-2320, 2005.

[109] John R Cameron, James G Skofronick, and Roderick M Grant, *Physics of the body*. Madison: Medical Physics Publishing, 1999.

[110] Soneson JE, "A User-Friendly Software Package for HIFU Simulation," in *8th*

International symposium on therapeutic ultrasound, 2009.

[111] Victor F. Humphrey, "Nonlinear propagation in the ultrasonic fields: measurements, modelling and harmonic imaging," *Ultrasonics*, vol. 38, pp. 267-272, 2000.

[112] Xiaofeng Zhao and Robert J McGough, "The Khokhov-Zabolotskaya-Kuznetsov (KZK) equation with power law attenuation," in *IEEE International Ultrasonics Symposium Proceedings*, 2014, pp. 2225-2228.

[113] Edward Jackson, C C Coussios, and R O Cleveland, "Nonlinear acoustic properties of ex vivo bovine liver and the effects of temperature and denaturation," *Physics in Medicine and Biology*, vol. 59, pp. 3223-3238, 2014.

[114] Johua E. Soneson and Matthew R Myers, "Thresholds for Nonlinear Effects in High-Intensity Focused Ultrasound Propagation and Tissue Heating," *IEEE Transactions on ultrasonics, Ferroelectrics, and Frequency Control*, vol. 57, no. 11, pp. 2450-2459, 2010.

[115] Janne Heikkila, Laura Curiel, and Kullervo Hynynen, "Local Harmonic Motion Monitoring of Focused Ultrasound Surgery-A Simulation Model," *IEEE transactions on biomedical engineering* , vol. 57, no. 1, pp. 185-193, January 2010.

[116] Sapareto SA and W C Dewey, "Thermal dose determination in cancer therapy," *International Journal of Radiation Oncology, Biology ,Physics*, vol. 10, pp. 787-800, 1984.

[117] E Sapin-de Brosses, J L Geenisson, M Pernot, M Fink, and M Tanter, "Temperature dependence of the shear modulus of soft tissues assessed by ultrasound," *Physics in Medicine and Biology*, vol. 55, pp. 1701-1718, 2010.

[118] Emilie Sapi-de Brosses, "The link between tissue elasticity and thermal dose in vivo," *Physics in Medicine and Biology*, vol. 56, pp. 7755-7765, 2011.

[119] Man Zhang et al., "Real-time sonoelastography of hepatic thermal lesions in a swine model," *Medical Physics*, vol. 35, no. 9, pp. 4132-4141, 2008.

[120] Xuegong Shi, W Roy Martin, Daniel Rouseff, Shahram Vaezy, and Lawrence A Curm, "Detection of High-Intensity Focused Ultrasound Liver Lesions Using Dynamic Elastometry," *Ultrasound Imaging and Tissue Characterization Symposium*, vol. 21, pp. 107-126, 1999.

[121] Raffaella Righetti et al., "Elastographic Characterzation of HIFU-induced Lesions in Canine Livers," *Ultrasound in Medicine and Biology*, vol. 25, no. 7, pp. 1099-1113, 1999.

[122] Tao Wu, Joel P Felmlee, James F Greenleaf, Stephen J Riederer, and Richard L Ehman, "Assessment of Thermal Tissue Ablation With MR Elastography," *Magnetic Resonance in Medicine*, vol. 45, pp. 80-87, 2001.

[123] Shigao Chen et al., "Shearwave Dispersion Ultrasound Vibrometry (SDUV) for Measuring Tissue Elasticity and Viscosity," *IEEE Transactions on Ultrasonics, Ferroelectrics, and Frequency control*, vol. 56, no. 1, pp. 55-62, 2009.

[124] Danial Shahmirzadi, Elisa Konofagou, Gary Hou, and Jiangang Chen, "Ex vivo characterisation of canine liver tissue viscoelasticity after high intensity focused ultrasound ablation," *Ultrasound in medicine and biology*, vol. 40, no. 2, pp. 341-350, August 2013.

[125] Hua Xie et al., "Quantitative Assessment of Thermal Lesion Stiffness in the Liver: Initial ex vivo Results," in *UEEE Ultrasonics Symposium(IUS)*, Orlando, FL, 2011, pp. 2098-2101.

[126] Sacha D Nandlall, "Monitoring Cell and Tissue Damage During Ablation by High-Intensity Focussed Ultrasound," 2011.

[127] Sacha D.Nandlall, Edward Jackson, and Constantin-C Coussios, "Real-Time Passive Acoustic Monitoring of HIFU-Induced Tissue Damage," *Ultrasound in Medicien and Biology*, vol. 37, no. 6, pp. 922-934, 2011.

[128] Sitaramanjaneya Reddy Gunter, Kang Il Lee, Dong-Guk Paeng, Andrew John Coleman, and Min Joo Choi, "Temperature-Dependent Thermal Properties of Ex Vivo Liver Undergoing Thermal Ablation," *Ultrasound in Medicine and Biology*, vol. 39, no. 10, pp. 1771-1784, 2013.

[129] E. Shamonina and L Solymar, "Superdirectivity by virtue of coupling between

meta-atoms," in *Proc in Metamaterials'*, Bordeaux, France, 2013, pp. 97-99.

[130] Zhuxian Zhou and Zheng-Rong Lu, "Godolinium-Based Contrast Agents for MR Cancer Imaging," *Wiley Interdiscip Rev Nanomed Nanobiotechnol*, vol. 5, no. 1, pp. 1-30, Jan 2013.

[131] Yifan Chen, Panagiotis Kosmas, and Sylvain Martel, "A feasibility study for microwave breast cancer detection using contrast-agent-loaded bacterial microbots," *International Journal of Antennas and Propagation*, vol. 2013, pp. 1-11, June 2013.

[132] Jacob Beutel, *Medical Imaging: Physics and Psychophysics*. Washington: The international society for optical engineering, 2000.

[133] H.T.O'Neil, "Theory of Focusing Radiators," *Journal of the Acoustical Society of America*, vol. 21, no. 5, pp. 516-526, 1949.

[134] Oleksiy S. Kim, Sergey Pivnenko, and Olav Brienbgerg, "Superdirective Magnetic Dipole Array as a First-Order Probe for Spherical Nearfield Antenna Measurements ," *IEEE transactions on antennas and propagation*, vol. 60, no. 10, pp. 4670-4676, October 2012.

[135] Lihong V. Wang, "Ultrasound-mediated biophotonic imaging: a review of acousto-optical tomography and photo-acoustic tomography," *Disease Markers*, vol. 19, pp. 123-138, 2003-2004.